

**Permeability and porosity as constraints on
the explosive eruption of magma:
Laboratory experiments and field
investigations**

Inauguraldissertation
zur Erlangung des Doktorgrades
Fakultät für Geowissenschaften
der Ludwig-Maximilians-Universität München

vorgelegt von
Sebastian Müller

München
26. Oktober 2006

1. Berichterstatter: Prof. Donald Bruce Dingwell

2. Berichterstatter: Prof. Ludwig Masch

Tag der mündlichen Prüfung: 27. April 2007

For we must suppose that the wind in the earth has effects similar to those of the wind in our bodies whose force, when it is pent up inside us, can cause tremors and throbbings (...)

Aristoteles, *Meteorologica*, Book II

Table of Content

Table of Content	VII
List of Figures	X
List of Tables	XIII
Preamble	XV
Zusammenfassung	1
1 Introduction	7
1.1 Explosive volcanism – threat and challenge.....	7
1.2 The development of porosity – bubble nucleation and growth	9
1.3 Causes and consequences of magma permeability.....	12
2 Sample provenance and preparation	15
2.1 Investigated volcanoes.....	15
2.1.1 St. Augustine, Alaska, USA	16
2.1.2 Bezymianny, Kamchatka, Russia	18
2.1.3 Colima, Mexico	20
2.1.4 Krakatau, Indonesia	23
2.1.5 Kelut, Indonesia.....	24
2.1.6 Merapi, Indonesia	26
2.1.7 Soufrière Hills, Montserrat, UK	27
2.1.8 Campi Flegrei, Agnano-Monte Spina, Italy	29
2.1.9 Stromboli, Italy.....	30
2.1.10 Monte Pilato, Lipari, Italy	31
2.1.11 Santorini, Greece	33
2.1.12 Mt. Unzen, Japan	34
2.1.13 Pinatubo, Philippines	36
2.1.14 Sample overview	37
2.2 Sample preparation	39
2.3 Laboratory porosity determination	40
3 Field porosity investigations	42
3.1 Introduction	42
3.2 Field based porosity determination.....	43
3.3 Field porosity measurements – results.....	45

3.3.1	St. Augustine	45
3.3.2	Bezmyianny	47
3.3.3	Colima	50
3.3.4	Krakatau.....	51
3.3.5	Kelut	52
3.3.6	Merapi.....	54
3.3.7	Unzen.....	56
3.4	Interpretations	57
3.4.1	Correlations between porosity distributions and eruptive behaviour	57
3.4.2	Correlations between porosity and the size of volcanic eruptions	60
4	Permeability measurements on volcanic rocks – influences of texture and temperature	65
4.1	Factors controlling permeability.....	65
4.1.1	Basic parameters.....	65
4.1.2	Textural parameters	65
4.2	Permeability measurements - method.....	70
4.2.1	Experimental setup	70
4.2.2	Data analysis.....	72
4.2.3	Error estimation	77
4.3	Permeability measurements - results	78
4.4	Permeability-porosity relationships - interpretations.....	79
4.5	High-temperature permeability measurements – experimental difficulties, possible solutions and preliminary results	82
4.5.1	Experimental approaches.....	83
4.5.2	High-temperature measurements with a NaCl sealing	86
5	Permeability control on volcanic fragmentation processes	91
5.1	Introduction	91
5.2	Bubble overpressure and its reduction.....	91
5.3	Experimental procedure.....	93
5.4	The effect of permeability on the fragmentation threshold	95
5.4.1	Fragmentation energy density.....	100
5.4.2	Implications	102
6	Summary and conclusions	104
7	Bibliography.....	107

Acknowledgements	117
Appendices	119
A. Permeability measurements and the use of the filtration codes – an operating manual	119
B. Tables of experimental results	124
Curriculum vitae.....	129

List of Figures

Figure 1.1: Schematic view of processes in a volcanic conduit	10
Figure 1.2: Bubble growth history	11
Figure 2.1: World map with investigated volcanoes.	15
Figure 2.2: TAS diagram	16
Figure 2.3: St. Augustine volcano	16
Figure 2.4: Thin section and sample picture of St. Augustine andesite.	17
Figure 2.5: Bezymianny volcano	18
Figure 2.6: Thin section and sample picture of Bezymianny andesite.	19
Figure 2.7: Colima volcano	20
Figure 2.8: Schematic depiction of the stages of Colima eruption cycles.....	21
Figure 2.9: Thin section and sample picture of Colima andesite	22
Figure 2.10: Krakatau islands	23
Figure 2.11: Thin section and sample picture of Krakatau pumice.....	24
Figure 2.12: Kelut volcano	24
Figure 2.13: Thin section and sample picture of Kelut basaltic andesite.	25
Figure 2.14: Merapi volcano.	26
Figure 2.15: Thin section and sample picture of Merapi andesite.....	27
Figure 2.16: Soufrière Hills volcano	27
Figure 2.17: Thin section and sample picture of Soufrière Hills andesite.....	28
Figure 2.18: Campi Flegrei caldera.	29
Figure 2.19: Thin section and sample picture of Campi Flegrei pumice.....	30
Figure 2.20: Stromboli volcano.	30
Figure 2.21: Thin section and sample picture of Stromboli scoria.....	31
Figure 2.22: Monte Pilato, Lipari.	31
Figure 2.23: Thin section and sample picture of Lipari pumice.....	32
Figure 2.24: Santorini island	33
Figure 2.25: Thin section and sample picture of Santorini pumice.....	34
Figure 2.26: Unzen volcano.....	34
Figure 2.27: Thin section and sample picture of Unzen dacite	35
Figure 2.28: Pinatubo volcano.....	36
Figure 2.29: Thin section and sample picture of Pinatubo grey pumice.. ..	37

Figure 2.30: Pumice clast with a drilled sample cylinder.....	39
Figure 2.31: Helium pycnometer.....	40
Figure 3.1: The setup used for field density/porosity measurements	44
Figure 3.2: Locations of density measurements on Augustine island	46
Figure 3.4 Porosity distributions of Augustine volcano	47
Figure 3.5: Locations of density measurements on Bezymianny volcano	48
Figure 3.6: Porosity distributions of Bezymianny volcano	49
Figure 3.7: Locations of density measurements on Volcán de Colima.	50
Figure 3.8: Porosity distributions of Colima	51
Figure 3.9: Locations of density measurements on Krakatau.....	51
Figure 3.10: Porosity distributions of Krakatau.	52
Figure 3.11: Locations of density measurements on Kelut volcano.....	53
Figure 3.12: Porosity distributions of Kelut	53
Figure 3.13: Locations of density measurements on Merapi volcano.....	54
Figure 3.14: Porosity distributions of Merapi	55
Figure 3.15: Locations of density measurements on Unzen volcano.....	56
Figure 3.16: Porosity distributions of Unzen volcano.....	57
Figure 3.17: Compilation of the total porosity distribution datasets	58
Figure 3.18: Porosity-based classification of eruptive styles	60
Figure 3.19: Mean porosity vs. VEI	62
Figure 3.20: Mean porosity vs. eruption magnitude.....	64
Figure 4.1 Textural parameters that may influence the permeability	66
Figure 4.2: Permeability-porosity relations according to Kozeny-Carman equations	67
Figure 4.3: Permeability-porosity relation according to percolation theory.....	68
Figure 4.4: Permeability data of previous workers.....	69
Figure 4.5: The experimental setup for permeability measurements	71
Figure 4.6: Detailed view of the permeability autoclave setup	72
Figure 4.7: Pressure an temperature evolution curves of a permeability experiments....	73
Figure 4.8: Experimentally measured and calculated pressure evolution	75
Figure 4.9: Results of permeability measurements.	78
Figure 4.10: Comparison of k obtained by transient and quasi-static approaches	78
Figure 4.11: Permeability results - interpretations	80
Figure 4.12: Different types of pore textures responsible for permeability variations....	82
Figure 4.13: Sample mounting for high-temperature permeability measurements	85

Figure 4.14: Pressure profiles for high temperature experiments.....	87
Figure 4.15: Permeability development during high-temperature experiments	88
Figure 4.16: Pressure profiles of a degassing experiment on a steel cylinder.....	89
Figure 4.17: High temperature permeability measurement on a trachytic sample	90
Figure 5.1: Schematic depiction of permeability control on fragmentation processes....	92
Figure 5.2: Set-up of the autoclave section used for fragmentation experiments..	94
Figure 5.3: High- and room-temperature fragmentation threshold values	95
Figure 5.4: k - Φ relations of permeability-fragmentation experiment samples.	96
Figure 5.5: Permeability vs fragmentation threshold.	98
Figure 5.6: Permeability vs fragmentation threshold at samples with 80% porosity	99
Figure 5.7: Fragmentation threshold energy density vs permeability.	101
Figure 5.8: Comparison of the fit accuracy of two threshold-models.	103

List of Tables

Table 2.1: Overview of the samples used for permeability and/or fragmentation experiments.....	37
Table 3.1: Compilation of Tephra volume, measured mean density, calculated erupted mass and the explosivity scales M and VEI.	63
Table 5.1: Results of combined porosity, permeability, and fragmentation threshold determinations for 22 pumice/ breadcrust bomb samples and 10 dome rock samples....	97
Table B.1: Room-temperature permeability, porosity, threshold and energy density results of 112 samples.....	124
Table B.2: Parameters and results of high-temperature permeability experiments.....	127

Preamble

Parts of the contents presented in this thesis have been published in scientific journals or are in the process of reviewing:

Mueller, S., Melnik, O., Spieler, O., Scheu, B., Dingwell, D.B. (2005): Permeability and degassing of dome lavas undergoing rapid decompression: An experimental determination. *Bull Vulcanol* **67**, 526-538

Scheu, B., Kueppers, U., Mueller, S., Spieler, O., Dingwell, D.B.: Experimental volcanology on eruptive products of Unzen volcano. Submitted to *J Volcanol Geotherm Res.*

Mueller, S., Scheu, B., Dingwell, D.B.: Permeability control on magma fragmentation. Submitted to *Geology*, in review.

Parts of the permeability measurement setup development follow a previous study performed in the context of the diploma thesis “Die Entwicklung einer Permeabilitäts-Messmethode zur Analyse von Vulkaniten unter Hochdruck- und Hochtemperaturbedingungen”, by S. Mueller, LMU München, 2002.

Zusammenfassung

Vulkanausbrüche stellen eine der am schwierigsten vorhersagbaren Naturkatastrophen dar. Die Unwägbarkeiten beziehen sich dabei sowohl auf den Zeitpunkt eines Ausbruchs als auch auf dessen Ausprägung und Heftigkeit. Die Prozesse, die vor oder während eines Vulkanausbruchs ablaufen, werden durch eine Vielzahl physikalischer und chemischer Parameter beeinflusst. Die Tatsache, dass die meisten dieser Parameter in irgendeiner Form voneinander abhängen und sich somit gegenseitig beeinflussen, führt zu einem komplexen Netzwerk an Einflussgrößen, das nicht mehr rein theoretisch erfasst werden kann. Die Ergebnisse experimenteller Arbeiten an natürlichen Materialien gewinnen deshalb, insbesondere als Datengrundlage für numerische Eruptionsmodelle, zunehmend an Bedeutung. Solche Modelle stellen gerade zu Zeiten, in denen sozio-ökonomische Faktoren zu einer zunehmenden Bevölkerungsdichte und Agglomeration von Industrie in direkter Umgebung von Vulkanen führen, ein effektives Instrument zur Vorhersage und Risikoabschätzung dar.

Die Porosität eines Magmas und dessen Gaspermeabilität sind Parameter, die einen beachtlichen Einfluss auf den Charakter einer Eruption haben können. Detaillierte Untersuchungen der Permeabilität vulkanischer Gesteine und ihrer Abhängigkeit von Porosität und textuellen Gegebenheiten einerseits, und ihres Einflusses auf die Magmenfragmentation andererseits, sind deshalb für das Verständnis eruptiver Prozesse grundlegend. Gerade die Kombination von Feldbeobachtungen und Laborarbeit ermöglicht sowohl die Aufstellung einer statistisch relevanten Datenmenge, als auch die experimentelle Quantifizierung von Zusammenhängen verschiedener Gesteinsparameter.

Das Hauptaugenmerk dieser Arbeit lag auf der experimentellen Bestimmung der Gaspermeabilität vulkanischer Gesteine. Um dabei hoch-turbulente vulkanische Entgasungsprozesse zu simulieren, wurden die Versuche mit einer instationären Meßmethode nach dem Stoßrohr-Prinzip (*shock tube*) durchgeführt: Eine durch das kontrollierte Öffnen von Berstscheiben hervorgerufene, quasi-instantane Dekompression in einer Autoklavenkammer oberhalb des Probenzylinders verursacht einen Druckgradient über die Probe. Dieser Gradient führt entweder zur Filtration des

noch unter Druck stehenden Gases unterhalb des Probenzylinders durch den Porenraum des Gesteins, bis auch in der unteren Autoklavenkammer Atmosphärendruck herrscht, oder, wenn der initiale Gasdruck über einem probenspezifischen Schwellenwert liegt, zur Fragmentation der Probe. Die aufgezeichnete Druckverlaufskurve der unteren Autoklavenkammer dient als Grundlage für die Berechnung zweier Permeabilitätskoeffizienten: Ein linearer Koeffizient k , der in etwa der Darcy-Permeabilität eines laminar strömenden Fluids entspricht, und ein nicht-linearer Koeffizient C als Korrekturfaktor für das nicht-laminare Fließverhalten des Gases.

Die Permeabilität eines porösen Gesteins hängt von einer Vielzahl textueller Gegebenheiten ab. Das effektiv für die Gasfiltration verfügbare Porenvolumen, d.h. die Gesteinsporosität Φ , spielt dabei eine wichtige Rolle. Da Filtration in vulkanischen Gesteinen jedoch ausschließlich durch miteinander verbundene Poren und Brüche stattfinden kann, kommt dem Grad der „Poren-Verbundenheit“ die ausschlaggebende Bedeutung zu. Dieser Grad wird wiederum von Faktoren wie Klüftigkeit des Gesteins, mittlere Porengröße, Porengrößenverteilung, Porenform, etc. beeinflusst. Aufgrund der Komplexität dieser Einflüsse ist es nahezu unmöglich, die Permeabilität von natürlichen Materialien theoretisch zu berechnen oder vorherzusagen. Empirisch-experimentelle Arbeit ist in diesem Gebiet deswegen unabdingbar. Durch mehr als 360 Versuche an 112 Gesteinsproben verschiedener Herkunft, Zusammensetzung und Porentextur wurde mit dieser Arbeit eine umfassende Datenbasis an Permeabilitäts- und Porositätswerten für die Untersuchung verschiedenster Fragestellungen auf diesem Gebiet geschaffen.

Der Zusammenhang zwischen Porosität und Permeabilität vulkanischer Gesteine ist in erster Linie durch eine enorme Streuung gekennzeichnet. Für denselben Porositätswert können Permeabilitätswerte in einem Bereich von vier Größenordnungen auftreten. Dennoch konnten die in dieser Arbeit untersuchten Gesteine nach ihrer zugrundeliegenden Porengeometrie in zwei Gruppen mit unterschiedlichen Permeabilitäts-Porositäts-Trends klassifiziert werden. Der grundsätzliche Verlauf der beiden Trends konnte durch zwei verschiedene theoretische Modelle begründet werden: Bei niedrig-porösen Domgesteinen, bei denen Klüfte und stark deformierte und elongierte Poren einen übergeordneten Einfluss auf Entgasungsvorgänge haben, konnte der k - Φ -Trend mit Modellen zum Gasfluss durch kluftähnliche (zwei parallele Begrenzungsebenen) und kapillare Geometrien (Röhren) angenähert werden (Kozeny-Carman-Gleichungen; $k \sim \Phi^n$; $3 \leq n \leq 3,8$). Bei hoch-porösen Gesteinen explosiven Ursprungs (Bimse, Schlacken, Brotkrustenbomben), bei denen der Gastransport

bevorzugt durch ein Netzwerk miteinander verbundener, mehr oder wenig kugelförmiger Blasen stattfindet, konnte die Filtrations-Theorie von vollständig „überlappbaren“ Hohlkugeln (*fully penetrable spheres* – FPS; $k \sim (\Phi-30)^2$) als Näherung verwendet werden.

Die Permeabilität von Vulkaniten kann durch das Entstehen von Abkühlungs-(Mikro-)Rissen post-eruptiv verändert werden und entspricht damit nicht mehr der ursprünglichen Magmenpermeabilität. Experimente bei hohen, magmatisch relevanten Temperaturen können daher Aufschlüsse über die „reale“ Gesteinspermeabilität liefern.

Gasflusseexperimente bei hohen Temperaturen stellen jedoch eine hohe technische Herausforderung dar. Die Abdichtung der Probe gegen die Autoklavenwand bzw. den Probenhalter entpuppte sich dabei als das am schwierigsten zu lösende Problem. Letztendlich konnten jedoch durch die Verwendung von gepresstem NaCl als Dichtung erste zufrieden stellende Ergebnisse erzielt werden. Der relativ niedrige Schmelzpunkt von Kochsalz (801 °C) erlaubte jedoch -unter Berücksichtigung gewisser Verunreinigungen (z.B. Wasser) und einer Sicherheitsmarge- nur Versuchstemperaturen bis ~750 °C. Das feinkörnige Salz wird in den Zwischenraum von Autoklav und Probenzylinder eingefüllt und regelmäßig mittels eines Stahlrohrs und einer Presse komprimiert. Während des Versuchs kann das Salz jederzeit nach Bedarf weiterkomprimiert werden, um eventuell auftretende Undichtigkeiten wieder auszufüllen. Die leichte mechanische Deformierbarkeit der Salzkristalle sorgt hierbei für eine stets kompakte, gasdichte Ummantelung der Probe. Die Messergebnisse von drei Domgesteinen zeigen eine zum Teil deutlich reduzierte Filtrationsrate bei hohen Temperaturen, ein Effekt, der größtenteils auf die höhere Gasviskosität zurückzuführen sein dürfte. Eine diesbezügliche Korrektur ergab für die Proben einen höheren Permeabilitätswert als bei einer bei Raumtemperatur durchgeführten Messung. Dies könnte ein Hinweis auf eine durch thermische Expansion bedingte Weitung der für den Gasfluss relevanten Porenverbindungen sein. Da jedoch die kompressive Kraft, die das Salz (durch die manuelle Nachkomprimierung einerseits und die thermische Expansion des Salzes andererseits) auf den Probenzylinder ausübt, bei diesen Versuchen eine unbekannte Größe darstellt, müssen die erzielten Ergebnisse unter Vorbehalt betrachtet werden. Die Kompression könnte, insbesondere bei Gesteinen mit ausgeprägten Kluftsystemen, Risse in einem unbekanntem Maße verengen und somit einen - der thermischen Ausdehnung entgegenwirkenden - Einfluss auf die effektiv gemessene

Permeabilität haben. Der Vergleich von Permeabilitätswerten vor und nach dem Aufheizprozess und eine Langzeitmessung an einer peralkalinen (trachytischen) Probe legen nahe, dass bei den hier angewendeten Versuchsbedingungen keine permanenten Veränderungen der Porenstruktur (z.B. Kluftheilung) auftreten.

Für die Modellierung eruptiver Prozesse ist der Einfluss der Permeabilität auf die Magmenfragmentation von besonderem Interesse. Insbesondere der Fragmentationsschwellenwert (*fragmentation threshold*), d.h. die physikalischen Rahmenbedingungen, bei denen ein poröses Magma Gasüberdruck nicht mehr allein durch Filtration abbauen kann, sondern in Partikel verschiedener Größe zerbricht, stellt diesbezüglich einen wichtigen Parameter dar. Dieser Schwellenwert wurde lange Zeit allein als abhängig vom Erreichen einer bestimmten Porositätsstufe angesehen (z.B. *Sparks 1978, Thomas et al. 1994, Gardner et al. 1996*); neuere experimentelle Arbeiten proklamieren dagegen eine Kombination von Gasüberdruck und Porosität als bestimmende Faktoren (*Spieler et al. 2004b*). Mit einer Serie kombinierter Permeabilitäts- und Fragmentationsversuche konnte in der vorliegenden Arbeit zusätzlich ein beträchtlicher Einfluss der Permeabilität auf den Fragmentationsschwellenwert, insbesondere bei hoch-permeablen Gesteinen, experimentell nachgewiesen werden. Dieser Einfluss konnte in einer analytischen Beziehung zwischen Gasüberdruck, Gesteinsporosität und Permeabilität quantifiziert werden. Mit dieser Gleichung können nun numerischen Modellen von Conduit-Prozessen, wie der Übergang von effusivem zu explosivem Verhalten, realistischere Input-Parameter zur Verfügung gestellt werden. Diese können damit einen verbesserten Beitrag zur Risiko-Evaluierung explosiver Vulkane leisten.

Ein weiterer Aspekt der vorliegenden Arbeit bestand in der Analyse von Dichte- und Porositätsdaten von insgesamt acht zirkum-pazifischen Vulkanen, die teils im Rahmen von Feldkampagnen selber gemessen, teils aus der Literatur entnommen wurden (*Hoblitt & Harmon 1993, Kueppers 2005*). Bei den untersuchten Vulkanen handelt es sich um St. Augustine (Alaska, USA), Bezymianny (Kamtschatka, Russland), Colima (Mexiko), Merapi, Kelut, Krakatau (alle Indonesien), Unzen (Japan) und Mt. St. Helens (Washington, USA). Um eine statistisch aussagekräftige Dichteverteilung zu erhalten, wurde im Gelände die Dichte von durchschnittlich 60 - zufällig ausgewählten - Gesteinsproben pro Messpunkt mittels Archimedischem Prinzip (Messung des Gewichts

der Probe in Luft und ihres Auftriebs in Wasser) bestimmt (*Kueppers et al.* 2005). Pro Vulkan wurden zwischen drei und 37 Messpunkte bearbeitet. Aus der Rohdichte eines Gesteins kann bei bekannter Dichte der reinen Festphase des Materials (Matrixdichte oder Reindichte) dessen Porosität bestimmt werden. Die Matrixdichten wurden an Pulvern repräsentativer Proben im Labor mittels He-Pycnometrie bestimmt.

Die Resultate der einzelnen Messpunkte und der Gesamt-Porositätsdaten eines Vulkans wurden in Histogrammen mit einer Häufigkeitsverteilung der unterschiedlichen Porositätsklassen in 5 %-Schritten dargestellt. Die vergleichende Interpretation dieser Porositätsverteilungen erlaubt (a) Aussagen über regionalspezifische Eruptions- und Ablagerungsmechanismen, wenn die einzelnen Probenpunkte eines Vulkans untereinander verglichen und analysiert werden, und (b) Aussagen über generelle, überregionale Zusammenhänge bezüglich Eruptionscharakteristika und Explosivität, wenn die Gesamtdatensätze mehrerer Vulkane betrachtet werden. In diesem Zusammenhang interpretierbare Parameter sind die generelle Form (z.B. unimodal-bimodal) und die Varianz (d.h. die „Breite“) einer Verteilungskurve, sowie die Werte der Häufigkeits-Maxima und der Porositäts-Durchschnitte.

Anhand dieser Parameter konnten die acht untersuchten Vulkane in drei übergeordnete Eruptions-Klassen eingeordnet werden: (1) Dom-bildende Vulkane, deren Haupt-Aktivitätsform aus gravitativ induzierten Block- und Asche-Strömen (*block-and-ash-flow* oder *nuée ardente*) und seltenen explosiven Events besteht (Merapi, Unzen, Colima), (2) Kryptodom-bildende Vulkane, bei denen ein plötzliches dekompressives Ereignis (z.B. Hangrutsch) einen explosiven Ausbruch (*lateral* oder *directed blast*) hervorgerufen hat (Mt. St. Helens, Bezymianny), und (3) explosive, subplinianische bis plinianische Eruptionen mit pyroklastischen Strömen (Kelut, Krakatau, St. Augustine).

Des Weiteren wurden mögliche Zusammenhänge zwischen den mittleren Porositätswerten einer Eruptionsablagerung und der Explosivität eines Ausbruchs untersucht. Als Messgrößen für die Explosivität wurden dabei zwei verschiedene in der Literatur beschriebene Indizes verwendet:

- Der *Volcanic Explosivity Index* (VEI) nach *Newhall & Self* (1982), eine größtenteils auf dem Gesamtvolumen des bei einem Ausbruch (oder während einer längeren Eruptionsphase) geförderten Materials basierende Kennzahl zwischen 0 (= rein effusiv) und 8 (= katastrophal explosiv), und

- die *Eruption Magnitude* (M) nach *Pyle* (1995, 2000), der die Masse des geförderten Materials als Grundlage dient.

Während der Abgleich der Porositätsdaten mit dem VEI einen eher qualitativen, positiven Zusammenhang mit allerdings ungenauer Korrelation bei niedrig-porösen und -explosiven Förderprodukten aufweist, konnte durch Berechnung der *Eruption Magnitude* (unter Verwendung der in dieser Studie ermittelten Porositätswerte) eine insgesamt bessere Korrelation erreicht werden. Abweichungen von einem linear ansteigenden Trend können dabei durch die jeweiligen Eruptionscharakteristiken (z.B. Kryptodom, phreatomagmatische Aktivität) erklärt werden.

1 Introduction

1.1 Explosive volcanism – threat and challenge

The relationship between mankind and volcanoes is of ambivalent nature. On the one hand, people have always benefited from the fertility of the rich volcanic soils and the amenities of hot springs, and therefore often settled in proximity of volcanoes. But every now and then, the apparently peaceful landscapes tend to turn into vigorously exploding volcanoes, responsible for lethal catastrophic events that may destroy human lives, buildings, and infrastructure. Several of the most serious natural disasters in history are correlated to explosive volcanic eruptions – either directly by pyroclastic flows and ash fall, or indirectly through the effect of tsunamis (e.g. Krakatau 1883, with more than 36,000 casualties) or the impact of volcanic aerosols on climate and agriculture (e.g. Tambora 1815, with at least 117,000 casualties, *Sigurdsson* 2000). Just as the powerful consequences of these phenomena have always fascinated and frightened people, their causes have been subject to speculation and interpretation since early times of human civilization.

At the beginning of the 21st century, approximately 10 % of human population live within a 100 km radius of historically active volcanic centres, concurrently a considerable amount of capital is concentrated in those areas. Explosive volcanic eruptions generate natural hazards that can have devastating effects on human life, and the environmental status quo. The damage to infrastructure can lead to massive international capital flow with a social and economic hangover. For risk minimization and the prevention of casualties caused by the various effects of such an event it is therefore essential to understand mechanistically how a volcano works and why (and, even more important, when) it “chooses” to explode.

As of today, the most applicable methods for volcanic hazard assessment are provided by seismic or chemical monitoring of eruptive precursors. But considering the enormous speed of progress in computational technologies, numerical modelling is becoming an increasingly important tool to predict the course and consequences of an eruption. If provided with a framework of profound and realistic physico-chemical

parameters, such models can now deliver helpful insights even into extremely complex physical processes.

An explosive volcanic eruption as one of such processes derives its complexity from the interaction of a vast number of more or less interdependent physico-chemical parameters. Chemical composition, pressure, and temperature govern magma crystallinity, volatile exsolution, and viscosity. The latter in turn influence magma ascent and bubble growth dynamics. Overpressure development in volatile phase depends on the structure of a pore framework and its gas permeability. An efficient discharge of the gaseous phase again has an impact on magma viscosity and all the related processes and properties (e.g. *Gilbert & Sparks 1998, Dingwell 1998b, Cashman et al. 2000*).

It can be regarded as a primary task of experimental volcanology to contribute a basis of realistic data that may serve as input parameter for numerical models. This especially accounts for those natural processes, which are eluded from direct observation, or are too complex for a purely theoretical treatment. Magmatic fragmentation is a good example for such a complex process (*Mader et al. 2004*).

The subject of this work is to investigate the interrelations of porosity and permeability of natural volcanic rocks and examine the effects of both parameters on fragmentation processes and explosivity. For this purpose, a new setup for the investigation of permeability under conditions close to volcanic environments – high decompression rates, strongly transient conditions and high temperatures – has been developed. The influence of pore texture and volume on the permeability has been experimentally investigated (Chapter 4). The determination and quantification of a dependency between the degassing efficiency of a volcanic rock and its fragmentation behaviour was a further vital component of this work (Chapter 5). Porosity data from samples of various volcanic settings have been achieved in the laboratory and, in a statistical relevant amount, directly from volcanic deposits in order to analyse their significance for volcanic explosivity evaluations (Chapter 3).

1.2 The development of porosity – bubble nucleation and growth

A magma is basically a mixture of three phases: a viscous silicate melt, crystals, and a volatile phase. The composition of the latter varies with the magma's origin and degree of fractionation; the biggest portion is usually represented by H₂O and CO₂. Under deep-crustal conditions, volatiles are dissolved in the melt. The total amount of volatiles that can be kept in dissolution depends on the magma's composition, its temperature, and the confining pressure.

Bubble nucleation

The formation of a new gas phase requires a certain amount of volatile supersaturation in the silicate melt, in order to provide the energy input necessary to create new surfaces (Figure 1.1). Since a huge volume increase accompanies volatile exsolution and formation of a vapour phase, pressure reduction is the most effective mechanism to achieve this supersaturation. This depressurization might be caused e.g. by magma ascent to shallower levels or sudden confining wall rock failure. This type of bubble nucleation is also referred to as *first boiling* (Navon & Lyakhovskiy 1998). Another process to reach supersaturation is to increase the water content of the melt. The crystallization of OH-poor or -free minerals, would, for instance, increase the relative H₂O-content of the residual melt. This process is termed *second boiling* and may be of special importance for the pressurization of crystallizing magma chambers or lava domes (Navon & Lyakhovskiy 1998, Cashman et al. 2000, Francis & Oppenheimer 2003).

Once a melt is saturated, the thermodynamic equilibrium demands the formation of a separate vapour phase. According to classical nucleation theory for a homogenous material (e.g. Landau & Lifshitz 1980, Navon & Lyakhovskiy 1998), bubble formation is governed by the counterbalance between energy gained by balancing the saturation disequilibrium (volume energy) and energy lost by increasing the bubble-melt interface against surface tension (surface energy). A critical nucleus size, above which the bubble is stable and can grow, is defined at exactly the point, where volume energy and surface energy are balanced. If a bubble with a radius smaller than the critical radius is formed, capillary force closes the bubble. Classical nucleation theory predicts that - assuming

realistic surface tension values of silicate melts - extremely high supersaturation pressures of up to 150 MPa are required to cause nucleation in a *homogenous* medium (Navon & Lyakhovskiy 1998). However in a natural system with all kinds of impurities, nucleation may also occur *heterogeneously*. Crystals may provide particularly favourable sites for bubble nucleation, since the crystal-gas interface energy is lower than that of the melt to gas. Taking these heterogeneities into account, bubble nucleation may thus occur at much lower degrees of supersaturation (Navon & Lyakhovskiy 1998, Cashman *et al.* 2000). These two end-member models - purely homogenous versus heterogeneous - define two possible exsolution levels within a magma column. This relative position, with respect to the fragmentation level during an explosive eruption, is an important control on the resulting bubble sizes, bubble-size distribution and bubble number density of the pyroclasts, since it defines the time scale of bubble growth and coalescence. This may have considerable effects on the general dynamics of an eruption (Cashman *et al.* 2000).

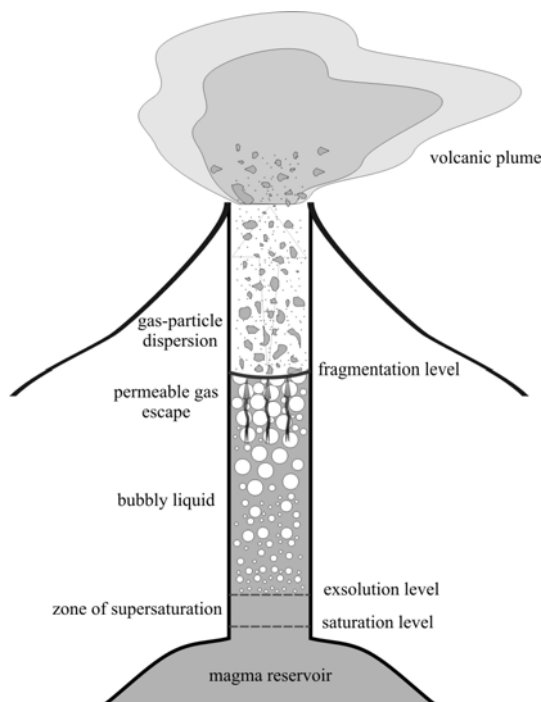


Figure 1.1: Schematic view of processes in a volcanic conduit. Bubble nucleation initiates when the magma has reached a certain amount of volatile supersaturation, which mainly depends on the available concentration of heterogeneities acting as nucleation sites. After nucleation, bubbles grow due to volatile diffusion and decompression, and eventually coalesce. If a system of interconnected pore space is established, gas will escape following the pressure gradient. Lastly, magma fragmentation transforms the bubbly flow into a gas-particle dispersion flow. Modified from Melnik *et al.* 2005.

Bubble growth

Once nucleated, bubble growth is - under constant ambient pressure - controlled by an interplay between water diffusion from the melt phase towards the melt-vesicle interface and bubble expansion against the viscous melt. In early stages of vesicle

expansion, when diffusion is rapid and a sufficient amount of water molecules is available, viscosity-controlled exponential growth (i.e. limited mainly by viscous resistance of the melt) dominates (Figure 1.2, A; *Cashman et al. 2000*). Above a certain vesicle size, diffusion is not rapid enough to maintain the equilibrium saturation pressure in the bubble, so the growth slows down and follows the square-root of time, i.e. the time-bubble radius path becomes parabolic (Figure 1.2, B; *Lyakhovskiy et al. 1996*). The velocity of bubble expansion is then primarily limited by the efficiency of diffusive flux. In natural systems with many vesicles, the growth of a single bubble will at some point be influenced and further slowed by the proximity of neighbouring bubbles, expressed by mean separation distances between bubbles (Figure 1.2, C). Once the system approaches mechanical and chemical equilibrium, that is the gas pressure in the bubble reaches ambient pressure, and volatile concentration in proximity to the bubble is uniform, the bubbles have reached their final size, and growth stops (*Lensky et al. 2004*).

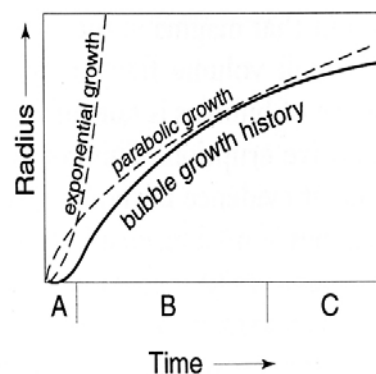


Figure 1.2: Bubble growth history is divided into three segments: A – growth is exponential and viscosity-limited, B – growth is parabolic and diffusion-limited, C – growth is hindered and slowed by neighbouring bubbles. From *Cashman et al. 2000*

The duration of each of these stages depends on the melt composition, which controls viscous deformation, the volatile content (and thus diffusivity), the ambient pressure, and the rate of decompression (e.g. *Toramaru 1995, Navon & Lyakhovskiy 1998, Lensky et al. 2004*). The relative time scales of the related processes have a direct impact on the eruptive style. Deep in the conduit, viscosity is relatively low, and bubble growth is limited by the rate of volatile diffusion. As magma ascends, its viscosity increases because of cooling and crystallization; yet decompression favours bubble expansion, in turn limited by the viscous resistance of the surrounding melt. At

shallower depth, this enhanced viscous resistance may result in considerable amounts of excess pressure in the bubbles, which may eventually lead to magma fragmentation by internal overpressure (Figure 1.1; *Cashman et al.* 2000). These effects will be addressed further in Chapter 5.

Porosity

The entirety of the bubbles nucleated, grown, and coalesced during ascent, together with syn- and post-eruptive shear- cooling- or expansion fractures, define the total porosity of a volcanic rock. It is commonly expressed as a fraction of the bulk volume (vol% or fraction between 0 and 1). The total porosity (Φ_{tot}) of a material is composed by the connected (or open, accessible, effective) pore space (Φ_{op}) plus isolated (or closed) pores.

In contrast to sedimentary rocks with an intergranular porosity, where the void space is primarily defined by the interstices between single grains or particles and is commonly highly interconnected, the porosity of volcanic rocks derives from originally isolated, 'spherical' vesicles. The accessibility of gas to flow between these vesicles is provided mainly by bubble-bubble interconnections, formed during bubble coalescence. If a sample has experienced considerable brittle deformation, the influence of (micro- and macro-) cracks on the formation of a connected porosity may be substantial. The resulting texture of a volcanic rock's pore space depends on its history of coalescence, shear deformation (elongation) and compaction during ascent or emplacement. Important parameters in this context are the bubble size, the bubble size distribution, the bubble number density (number of bubbles per volume unit), the bubble's aspect ratios, the degree of coalescence, and, indirectly, also the crystal content. Textural features of porosity and their relation to permeability will be further addressed in Chapter 4.

1.3 Causes and consequences of magma permeability

According to theoretical solubility relationship (e.g. *Shaw* 1974), initial H₂O contents of many dacitic to rhyolitic magmas (4-6 wt%) should lead to porosities of about 75 vol% at 450-750 m depth and >99 vol% at the volcanic vent (*Klug & Cashman* 1996). The fact that such high vesicularities are rarely found in natural pumices indicates the presence of more or less effective degassing of the magma during ascent.

Degassing is a crucial process for the eruptive behaviour of a volcanic system. Beside its superficially visible manifestations, like volcanic gas emission and the precipitation of magmatic-hydrothermal deposits, it may have substantial impacts on the fragmentation behaviour (*Klug & Cashman 1996, Dingwell 1998a, Papale 2001*), the transition in eruptive styles (explosive-effusive; *Eichelberger et al. 1986, Dingwell 1996, Gonnermann & Manga 2003, Melnik et al. 2005*), the pressurization of lava domes and plugs (*Sparks 1997, Navon et al. 1998*), and post-fragmentation processes (*Kaminsky & Jaupart 1997*).

Gas filtration through magma occurs if an interconnected framework of pores and fractures has been developed during bubble growth and brittle deformation, and a pressure gradient exists that drives the motion of the gas phase. The permeability of such a system is limited by the aperture size of the bubble-bubble interconnections or the width of a fracture (*Blower 2001a*). To create a network of bubbles connected via apertures, the vesicles have to mechanically interact and coalesce at some point during ascent. This is considered to happen mainly through the process of thinning and subsequent failure of bubble walls. The time scale of melt film rupture thereby depends on the balance between two counteracting forces: the pressure difference that causes radial expansion of bubbles together with capillary and gravitational forces (both acting to retract the melt films between touching vesicles), against viscous resistance of the liquid (*Klug & Cashman 1996, Navon & Lyakhovskiy 1998*). According to *Klug & Cashman (1996)* the frequent occurrence of coalesced bubbles in pumices indicates that the aforementioned time scale of wall thinning is less than the time scale of fragmentation.

Assumptions about the mechanisms and directions of gas escape diverge: some models assume that magma degassing through the conduit wall into the country rock is significant (e.g. *Jaupart 1998*), while others claim effectively impermeable conduit walls and a vertical direction of gas filtration through a permeable bubbly magma (*Jaupart & Allegre 1991, Woods & Koyaguchi 1994*).

However, as the dynamics of volcanic eruptions are likely to be sensitive to volatile content, exsolution mechanisms, and gas overpressures, small changes of the permeability within a volcanic system may change the eruptive style considerably. Accordingly, sudden transitions from effusive to explosive behaviour and back may, for example, be attributed to the opening of new fracture systems within a volcanic edifice, giving rise to a sudden increase in degassing efficiency. Similarly, a gradual increase of

the permeability of a porous magma and the transition from closed- to open-system degassing may at some point lead to the transgression of the critical degree of volatile and overpressure extraction from the magma, and cause termination of explosive activity. Examples and explanations of these kinds of eruptive style transitions are given in *Eichelberger et al.* 1986, *Woods & Koyaguchi* 1994, *Gonnermann & Manga* 2003, *Melnik* 2000 and *Melnik et al.* 2005.

A contribution to the ongoing debate, whether a high permeability can influence, and eventually also prevent magma fragmentation, is given by the experimental investigations described in Chapter 5 of this thesis.

2 Sample provenance and preparation

2.1 Investigated volcanoes

For this work, pyroclastic rocks of 13 volcanoes have been analysed (Figure 2.1). The samples were taken and provided by Bettina Scheu and Ulrich Küppers (Unzen), Oliver Spieler, (Merapi, Souffrière Hills, Santorini, Kelut, Krakatau), Andrea di Muro (Pinatubo), Jacopo Taddeucchi (Stromboli), Margarita Polacci (Stromboli, Pinatubo, Campi Flegrei), Dominique Richard and Simon Kremers (Kelut, Krakatau), and Daniele Giordano (Campi Flegrei). Samples from Augustine, Colima, Bezymianny, Campi Flegrei and Lipari were taken by myself in cooperation with Oliver Spieler.



Figure 2.1: Samples from 13 volcanoes that have been investigated in this study. World map base © www.kartenwelt.de.

To allow for profound empirical analyses, one of the fundamental concepts of this work was the coverage of a broadest possible range of volcanic products. This applies for textural parameters as well as for chemical compositions. Therefore, samples in a continuous range from basalt over andesite to rhyolite, as well as high-alkali trachytes have been used (Figure 2.2).

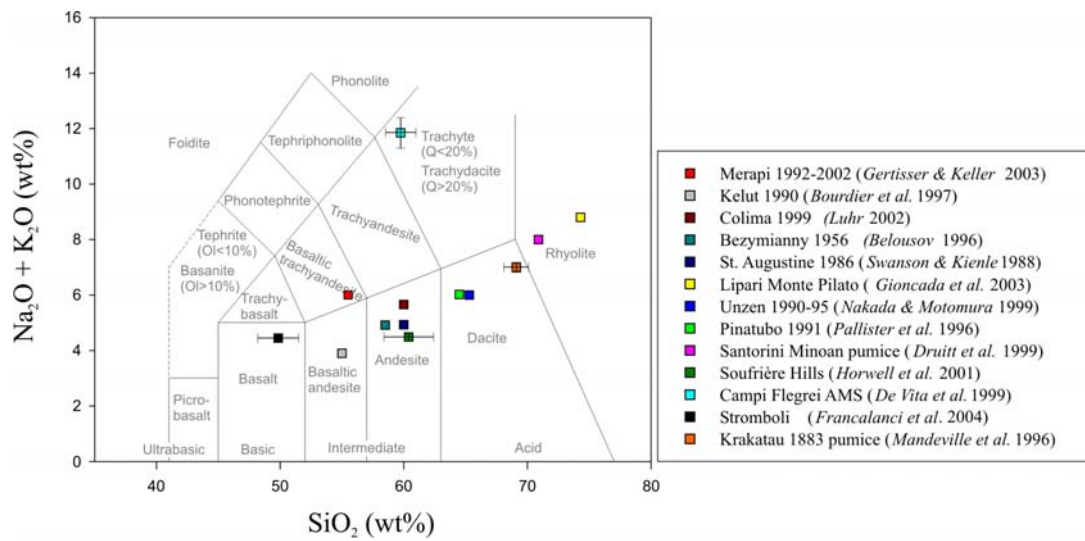


Figure 2.2: TAS diagram showing the chemical compositions of the volcanic rocks used in this work (after *LeBas et al. (1986)*).

In the following sections a short description of each of the investigated volcanoes, with their main characteristics in terms of erupted material and eruptive style, will be given.

2.1.1 St. Augustine, Alaska, USA

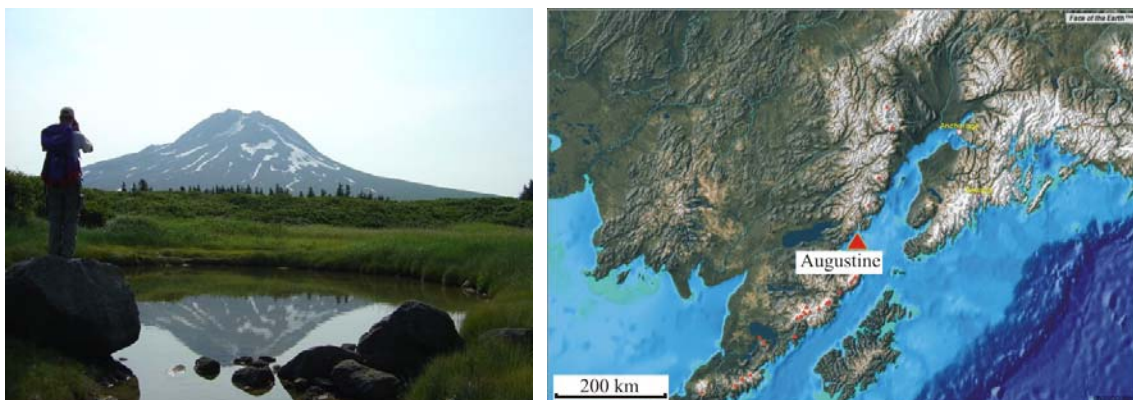


Figure 2.3: St. Augustine volcano seen from the north-western side. Augustine island is located in the Lower Cook Inlet, on the Alaskan south coast. Map: Face of the Earth™

St. Augustine volcano is 1260 m high, and located on Augustine Island, Lower Cook Inlet, southern Alaska, USA (59°23' N, 153°26' W; Figure 2.3). The volcano consists of a central dome and lava complex which is surrounded by pyroclastic debris.

Its eruptive style can be described as dome-building with occasional subplinian explosive activity. The Volcanic Explosivity Index (VEI) according to *Newhall & Self* (1982; see also Chapter 3.4) of the 1986 eruptive phase was classified as “4” (*Siebert & Simkin* 2002-).

St. Augustine is the youngest and most frequently active of the Cook Inlet volcanoes. Its activity began during the late Pleistocene Moosham glacial advance (19,000 – 15,500 years BP; *Johnson* 1979). In historical times, eight eruptive phases have been recorded: 1812, 1883, 1908, 1963/64, 1976, 1986 and 2005. The eruption of 1883 is considered to have had the most violent activity. Eruptions of Augustine volcano typically endure several months and consist of multiple phases. The first phase is typically the most violently explosive one; successive stages include minor explosive ash eruptions, pyroclastic and mud flows, and the extrusion of a lava dome (*Swanson & Kienle* 1988, *Waite & Beget* 1996).

The eruptive products of St. Augustine are commonly reddish dark grey to light grey porphyritic andesites with mainly plagioclase, pyroxene and magnetite phenocrysts (*Getahun et al.* 1996, *Waite & Beget* 1996). Pumices with mingled white and black parts are common. Magma composition was found to be relatively constant throughout eruptive history, with an average SiO₂ content of approximately 60 % (*Swanson & Kienle* 1988). The glass matrix of pumices ranges from dacitic to rhyolitic composition, with the most silicic glass sample showing > 72 % SiO₂ (*Waite & Beget* 1996).

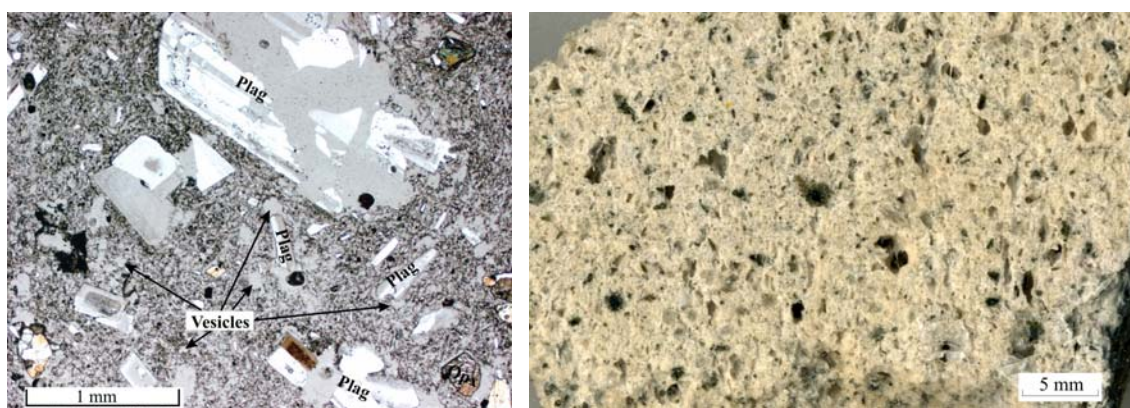


Figure 2.4: Left: Thin section of Aug P5 pumice (~70 vol% porosity), under partially polarized light. Plagioclase phenocrysts are up to 3 mm large, An-rich and often zoned and fractured. Further phenocryst phases are Opx and oxides. The largest portion of vesicles is small (10-30 μm) and forms an extensive network within the groundmass; some reach 100-200 μm and few large bubbles are up to 3 mm large. Right: White pumice of a 1986 pyroclastic flow deposit. The pumices are generally rich in crystals (mainly plagioclase and pyroxenes).

The samples investigated in this work derive from the 1986 eruption. The porosity/density distribution of volcanic products of eight different locations has been measured in a field campaign in summer 2004. The porosity of the investigated material ranges from ~3 to ~80 vol%.

2.1.2 Bezymianny, Kamchatka, Russia

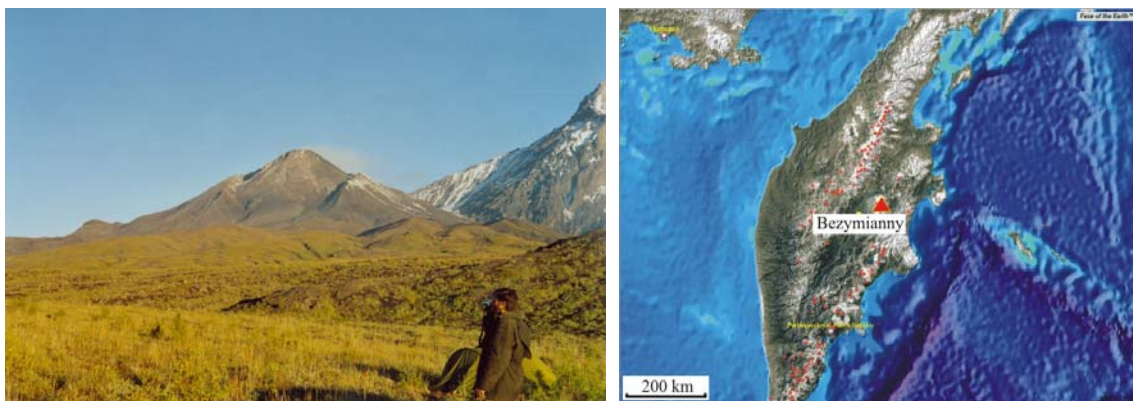


Figure 2.5: Bezymianny volcano on central Kamchatka peninsula seen from south-east. Visible is the horseshoe-shaped crater of the 1956 directed blast event with a newly grown dome structure. Map: Face of the Earth™.

The volcano (2882 m asl) is situated in the central part of the Klyuchevskaya volcanic complex, Kamchatka peninsula, Russia (56°04' N, 160°43' E; Figure 2.5). Its activity is dome-building with highly explosive eruptions, interrupted by up to several hundred years of quiescence. The explosivity of the last major explosive event in 1956 is rated as VEI 5 (*Siebert & Simkin 2002-*).

The eruptive history of Bezymianny volcano began 10,000–11,000 yBP with the extrusion of basaltic-andesitic to andesitic lava to form a “pre-Bezymianny” stratovolcanic structure. The present Bezymianny stratovolcano started growing 5000–5500 yBP. Three periods of activity were recorded within the last 2500 years: 2400–1700 yBP (B I), 1350–1000 yBP (B II) and 1955–present (B III; *Bogoyavlenskaya et al. 1991*).

The eruptive phase of 1955/56 culminated in a sector collapse triggering a directed blast event similar to the 1980 Mt. St. Helens eruption, and destroyed the formerly 3100 m high summit and the eastern slope, forming a horseshoe-shaped crater with a new dome structure in its centre. For this work, samples of proximal block-and-ash-flows from a 2000 eruption and deposits of the pyroclastic flows that followed the

1956 sector collapse, as well as deposits of the blast event itself have been investigated. Density measurements have been performed on five sites in September 2004.

The products of this eruption are dense, dark grey to bluish hornblende andesites, vesicular light-grey hornblende andesites, and rock fragments of the old pre-Bezymianny edifice. The bulk SiO₂-content ranges between 52.5 % and 65.5 % (*Bogoyavlenskaya et al.* 1991) and averages at around 58.5 % (*Belousov* 1996). Thin sections show that the main phenocrysts phases are plagioclase and hornblende (Figure 2.6).

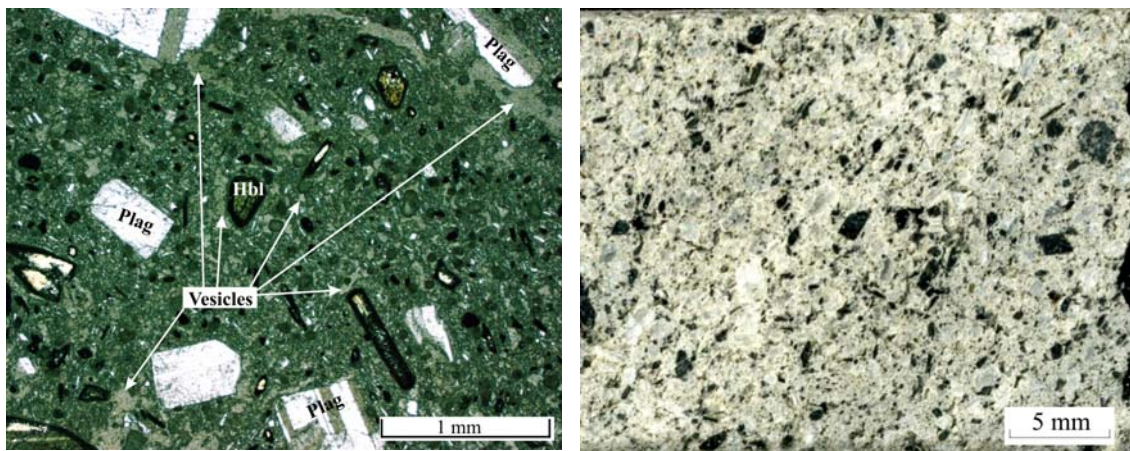


Figure 2.6: Left: Thin section of an andesite from 1956 Bezymianny blast-deposit. Vesicles are rather small with sizes mainly between 25 and 100 μm . They show for the most part deformation/ collapse structures (e.g. concavely shaped edges). The dominating phenocryst phase is plagioclase; hornblende and ore minerals are minor components. Mafic minerals are often rimmed by oxide minerals. Right: High-crystalline blast-deposit sample (porosity ~ 25 vol%) with deformed vesicles, and predominantly plagioclase and hornblende phenocrysts.

2.1.3 Colima, Mexico

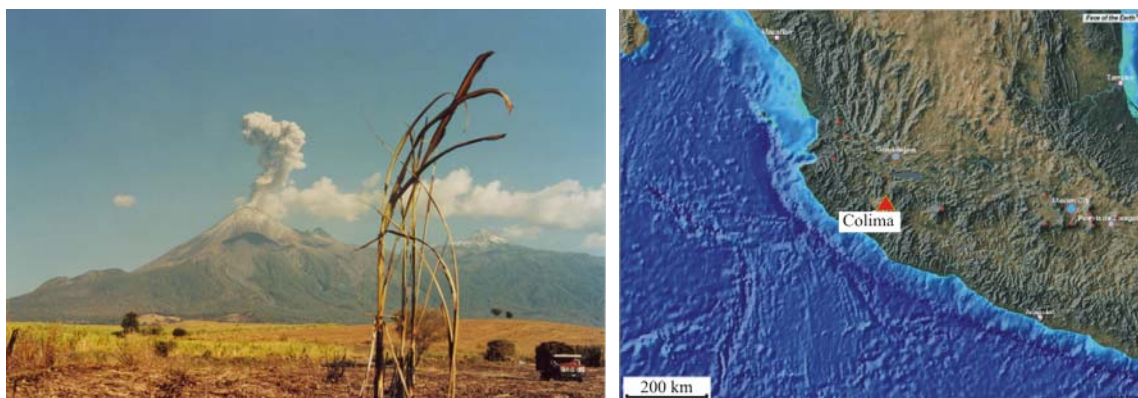


Figure 2.7: Small explosion of Colima volcano, photographed in April 2004 from the eastern side. The volcano is located in western central Mexico. Map: Face of the Earth™.

Volcán de Colima (also “Volcán de Fuego”) with an elevation of 3860 m asl is situated in western central Mexico ($19^{\circ}30' \text{ N}$, $103^{\circ}37' \text{ W}$; Figure 2.7), and is part of the Trans-Mexican Volcanic Belt. The stratovolcano marks the intersection of the N-S trending Colima Rift Zone and the NE-SW trending Tamazula Fault (*Zobin et al.* 2002). Together with the northerly adjacent inactive Nevado de Colima (4320 m) it forms the Colima volcanic complex. The volcanic activity of this complex can be traced back to at least 600,000 yBP. The formation of the two modern volcanoes began, on the basis of an older caldera structure, about 200,000 years ago (Nevado), and 50,000 years ago (Colima, “Paleofuego”), respectively. Each of them was affected by a huge Mt. St. Helens type eruption around 10,000 yBP (*Robin et al.* 1987).

Volcán de Colima is the historically most active volcano of Mexico, with at least 52 eruptions since AD 1560. Recent activity shows a pronounced cyclic character with 4 eruption cycles, each enduring about 100 years. An eruptive cycle is usually subdivided in the following stages (Figure 2.8): 1. Open crater a following cycle-ending explosion, 2. lava ascent and dome growth, 3. lava spills over crater rim or leaks out a flank vent, accompanied by block-and-ash-flows, 4. intermittent minor to major explosive activity (VEI 2-4), and 5. major plinian to subplinian explosive eruption (\sim VEI 4) to terminate the cycle. The current cycle started after a major explosive event in 1913, the actual state is presumably between stage 3 and 4 with explosions of a VEI of 2-3 (*Luhr* 2002).

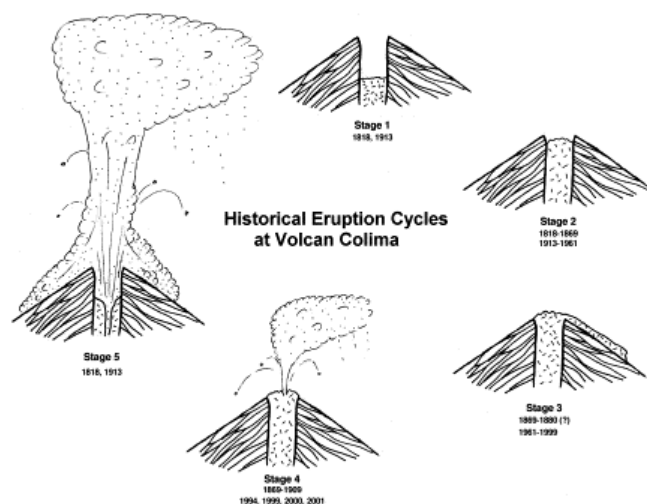


Figure 2.8: Schematic depiction of the five stages of eruption cycles of Colima volcano. Explanation see text. From *Luhr* 2002.

Volcán de Colima usually erupts andesitic lavas with ~ 61 wt% SiO_2 , the cycle-ending major explosions (e.g. 1818 and 1913), as well as 1976 and 1981/82 lava flows, involve more mafic andesites with ~ 58 wt% SiO_2 . This change in composition is attributed to a periodic recharge of deeper, mafic magma into a more differentiated magma reservoir and may be interpreted as a precursor for a cycle-terminating explosion in near future. The magma of the current eruption cycle contains 2-3.5 wt.% H_2O , which is significantly lower than the water contents of the 1896-1913 cycle. This indicates a lower explosivity of the current eruptive cycle (*Luhr* 2002).

The andesites of Colima show a porphyritic texture with plagioclase (13-25 vol%), orthopyroxene (2-4 vol%), clinopyroxene (3-4 vol%), and minor hornblende ($< 0.5\%$) as phenocrysts. Ti-oxides and olivine can occur as xenocrysts; the groundmass amounts to 59-68 vol% (*Luhr* 2002).

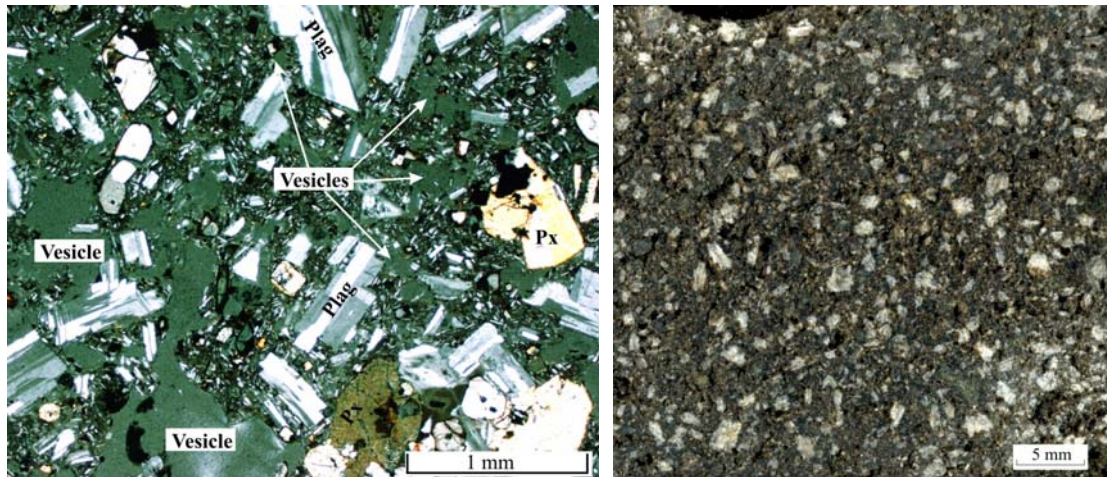


Figure 2.9: Left: Thin section of a Colima 1999 andesite under partly polarized light. The vesicles are irregularly shaped and form a highly interconnected network. Plagioclase phenocrysts are generally twinned and smaller than 1.5 mm. Ortho- and clinopyroxenes represent the second abundant phenocryst phase. The groundmass is rich in plagioclase microlites. Right: Polished sample section of a 1999 block-and-ash-flow sample with ~20% porosity. The samples are mostly high-crystalline with comparatively small phenocrysts.

In the course of two field campaigns in 2004 and 2005 the density distribution of four locations within the 1998/99 pyroclastic deposits on the south flank and products of a 2005 pyroclastic flow near Montegrande valley have been measured. Permeability measurements have been performed on block-and-ash-flow samples from Cordoban and San Antonio valley (1999 eruption), on lava flow samples from El Playón valley (1961 eruption), and on pumices and scoriae from the 1913 explosive eruption.

2.1.4 Krakatau, Indonesia



Figure 2.10: Anak Krakatau with the remnants of Rakata island in the background. The islands of Krakatau lie in the Sunda strait between Java and Sumatra. Photo courtesy Volcanological Survey of Indonesia, 1979, map: Face of the Earth™.

The caldera of Krakatau lies in the Sunda Strait between the Indonesian islands of Java and Sumatra, $6^{\circ}6' \text{ S}$, $105^{\circ}25' \text{ E}$ (Figure 2.10). It is part of the Sunda Arc, a 5400 km long chain of volcanoes parallel to a zone of subduction of the Indo-Australian plate beneath the Sunda plate and Burma microplate. Within this trench, the Sunda Strait represents a transitional area from oblique subduction under Sumatra ($\sim 55^{\circ}$), to near frontal subduction under Java ($\sim 13^{\circ}$; *Mandeville et al.* 1996).

The former Krakatau island, consisting of the three volcanoes Rakata, Danan and Perbuwatan, was mostly destroyed during the catastrophic caldera forming eruption of 1883. Only a remnant of Rakata volcano was left, the adjacent islands of Sertung and Panjang were covered by massive pumice fall. This VEI 6 eruption caused more than 36,000 fatalities, predominantly resulting from tsunami floodings over Indonesian coastlines. Since 1927, the cone of Anak Krakatau ('Child of Krakatau') formed within the 1883 caldera (*Francis & Oppenheimer* 2004, *Siebert & Simkin* 2002-).

Pumices of the 1883 eruption (Figure 2.11) have SiO_2 contents of 68.1 % to 70.1 %, covering the dacite to rhyodacite field of *LeBas et al.* (1986; *Mandeville et al.* 1996). Since 1972, Anak Krakatau shows frequent activity, consisting mostly of the extrusion of basaltic andesite lava flows, accompanied by minor explosive activity (VEI 1-2).

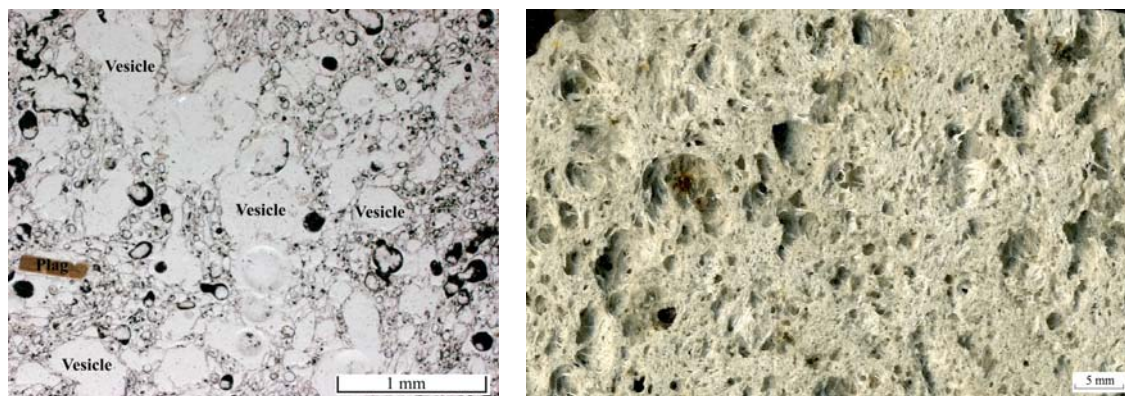


Figure 2.11: Left: Thin section of a highly vesicular pumice of the 1883 explosive eruption. Bubble size ranges from 20 μm to more than 7 mm, the size distribution is highly polydisperse. Especially large vesicles are often coalesced. The phenocryst content is rather low, the most abundant mineral phase is plagioclase (with a brownish appearance due to the partly polarized light). Right: Highly porous, white pumice from Rakata island (porosity ~ 85 vol%).

Density measurements have been performed by S. Kremers, D. Richard and O. Spieler on six locations (on Sertung, Rakata, Panjang, and Anak Krakatau), during a field campaign in March 2005. For the permeability investigations, white pumices of the 1883 eruption and basaltic andesites from the Anak Krakatau crater rim have been used.

2.1.5 Kelut, Indonesia

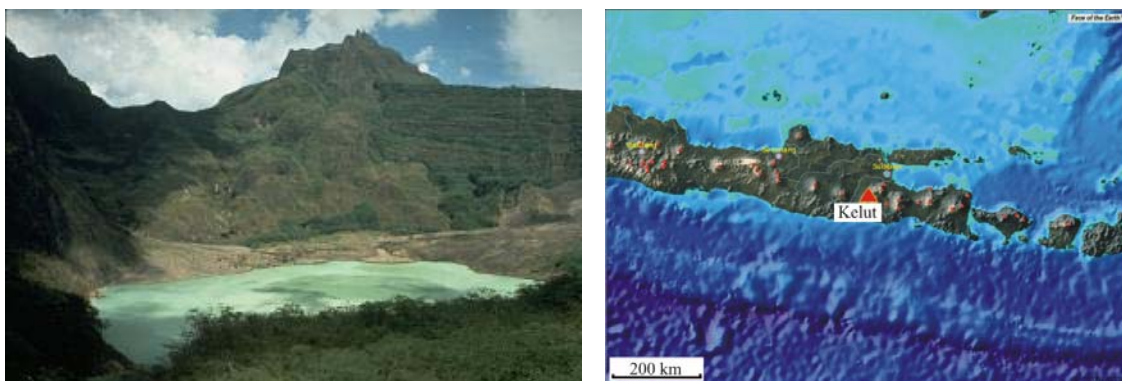


Figure 2.12: Crater lake of Kelut volcano, eastern central Java. Photo by Dan Dzurisin, 1980 (U.S. Geological Survey), map: Face of the Earth™.

Kelut is a 1731 m high stratovolcano, situated in the eastern part of Java ($7^{\circ}56'$ S, $112^{\circ}18'$ E; Figure 2.12). It consists of a cluster of summit lava and numerous craters, giving the volcano a rather irregular profile. Since AD 1000 more than 30 eruptions have been reported from Kelut, often accompanied by outpouring of the crater lake, leading to catastrophic lahars with numerous fatalities. Most eruptions are short (few

hours) but violent, and have usually a moderate magnitude in terms of erupted material volume (*Bourdier et al. 1997*). The most recent eruption (Feb 1990), started with a series of phreatic explosions, after 24 years of dormancy. A subsequent small plinian phase sustained for four hours and predominantly produced light grey pumices and dark scoriae. The VEI 4 eruption totalled $\sim 0.13 \text{ km}^3$ of erupted tephra (*Bourdier et al. 1997*, *Siebert & Simkin 2002-*).

Juvenile products of the 1990 eruptions (Figure 2.13) are basaltic andesites with $\sim 55 \text{ wt.}\% \text{ SiO}_2$ and a total alkali content of $\sim 3.9 \text{ wt.}\%$ (*Bourdier et al. 1997*).

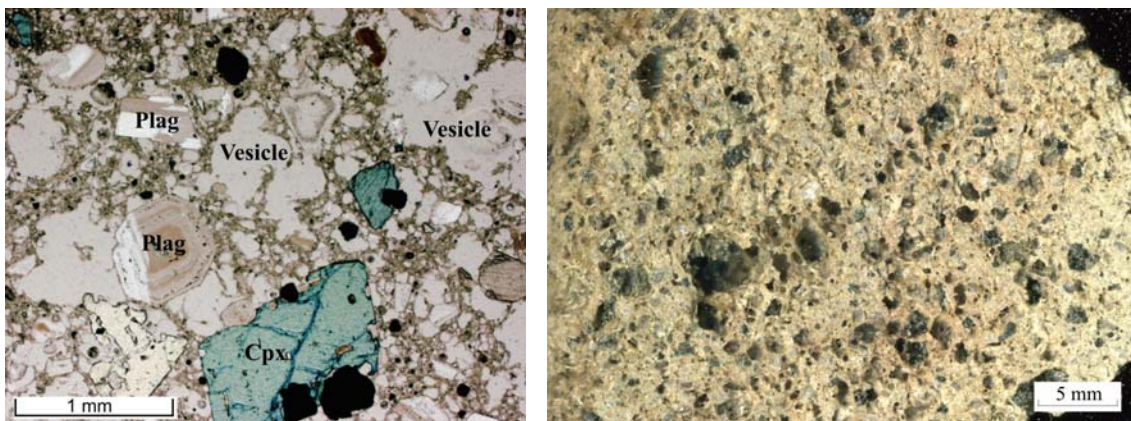


Figure 2.13: Left: Thin section of Kelut pumice, with a polarization angle of $\sim 80^\circ$. Phenocrysts are predominantly zoned plagioclase, clinopyroxene and orthopyroxene. Vesicles are polydispersely distributed, with sizes ranging from $\sim 30 \mu\text{m}$ to 2 mm. Large vesicles are deformed and often coalesced. Right: polished surface of a pumice from the Kelut 1990 eruption ($\sim 48 \text{ vol}\%$ porosity). The samples show a high crystallinity.

In March 2005, pyroclast density distributions were measured by O. Spieler, D. Richard and S. Kremers on six sites, permeability measurements were conducted on three pumices and one scoria sample from the 1990 eruption products.

2.1.6 Merapi, Indonesia

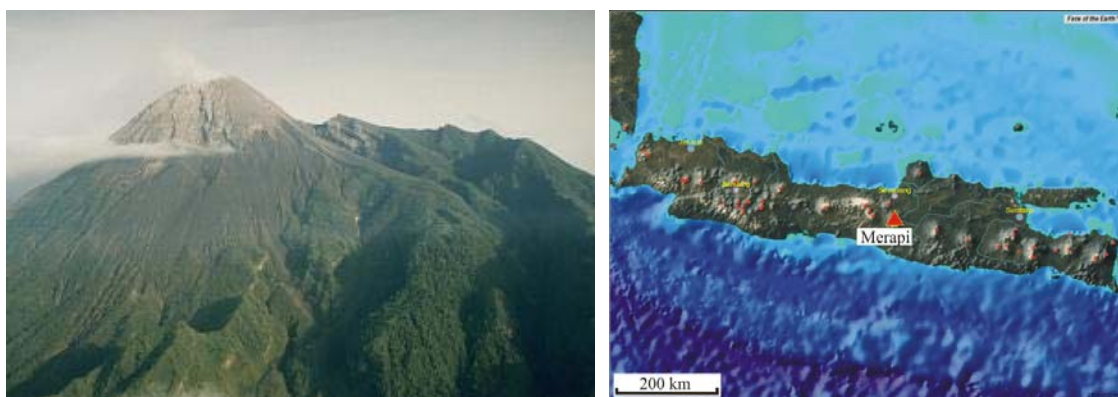


Figure 2.14: The 2968 m high Merapi volcano in central Java; Photo by Yustinus Sulistiyo, 1994 (Volcanological Survey of Indonesia), map: Face of the Earth™.

Merapi in central Java ($7^{\circ}32' S$, $110^{\circ}26' E$; Figure 2.14) is one of Indonesia's most active volcanoes. It is a 2968 m high basalt to basaltic-andesite stratovolcano, and the youngest and southernmost volcano of a NNW-SSE trending volcanic chain. The eruptive style of Merapi changed from frequent plinian to subplinian explosions (~ 3000 -250 yBP) to a dome-building and block-and-ash-flow dominated activity, with occasional small to moderate Vulcanian explosions (19th and 20th century). Merapi is eponymous for gravity-driven volcanic flows formed by non-explosive disintegration and collapse of parts of the dome or viscous lava flows. The explosivity of the most recent eruptions is estimated at VEI 2 (Andreastuti *et al.* 2000, Siebert & Simkin 2002-).

The 1992-2002 eruptive phase consisted of different stages of dome growth with varying effusion rates. In April 1994, lava extruded through a new vent. A catastrophic collapse event of this new dome structure occurred on November 22, 1994, and the accompanying southward directed block-and-ash-flow caused nearly 100 casualties (Voight *et al.* 2000). The samples investigated in the laboratory were collected in 1996 by O. Spieler and D.B. Dingwell from Boyong valley and represent deposits of this November 1994 event. Field density measurements were performed by B. Scheu and L. Schwarzkopf on six locations within the 1998 block-and-ash-flow deposits at the western flank of Merapi.

Samples of recent Merapi eruptions reveal whole-rock SiO_2 contents of ~ 55.5 wt% and total alkali contents of ~ 6.0 wt%, and are described as basaltic andesites with a relatively high-K tendency (Gertisser & Keller 2003). The solid phase of the dome rocks consists of 40-50 % plagioclase and pyroxene phenocrysts (1-2 mm) and a

microcrystalline phase. The porosity varies between 13 and 46 vol%, the pore texture is characterized by a very irregular shaped, complex ‘dendritic’ network of deformed bubbles (Figure 2.15).

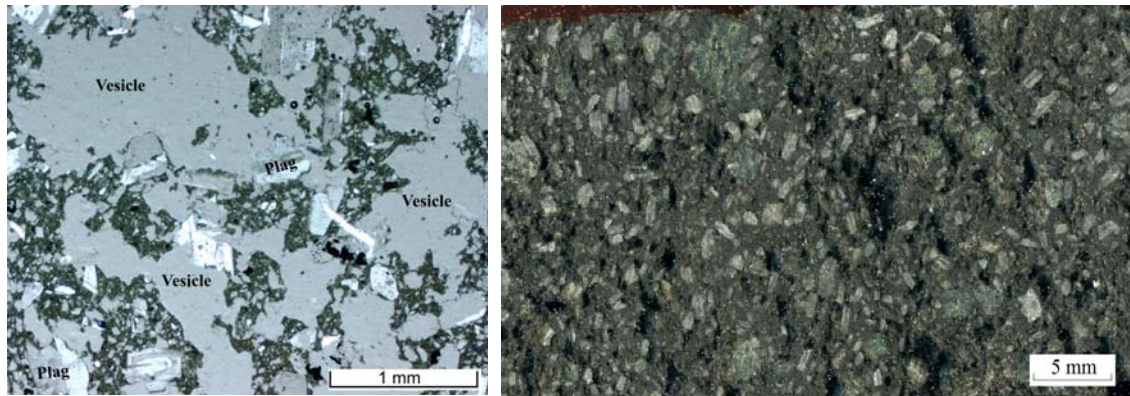


Figure 2.15: Left: Thin section of a Merapi andesite with ~35 vol% porosity under partly polarized light, showing a network of large, irregular shaped and highly interconnected pores. A population of smaller, macroscopically isolated vesicles range between 20 and 60 μm , the large vesicles can reach up to 2 mm. Phenocrysts (mainly plagioclase and pyroxenes) grew to a maximum size of 2 mm. Right: Merapi andesite sample MP C with ~45% porosity. Phenocrysts are abundant, but comparatively small.

2.1.7 Soufrière Hills, Montserrat, UK

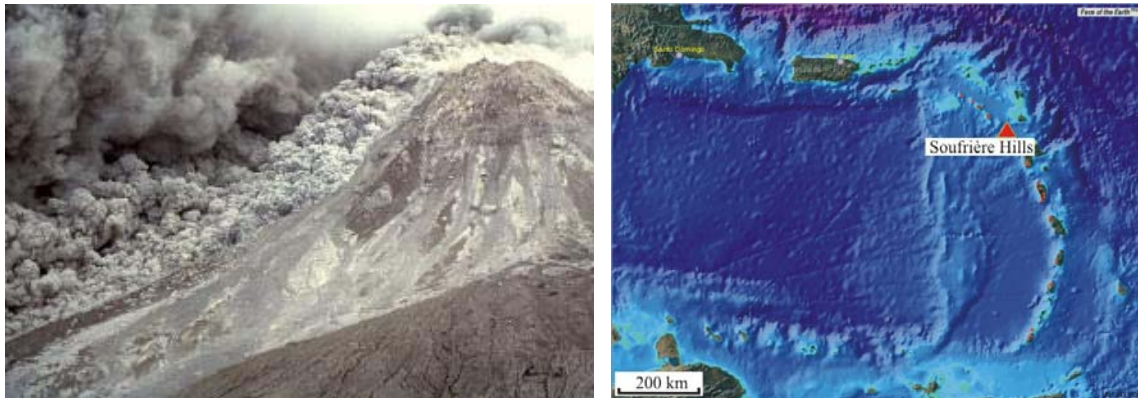


Figure 2.16: Pyroclastic flow on January 16, 1997, travelling down the southern flank of Soufrière Hills volcano on Montserrat island, Lesser Antilles islands, West Indies. Photo by *Richard Heard*, 1997 (Montserrat Volcano Observatory), map: Face of the Earth™.

Soufrière Hills Volcano is a 915 m high andesitic stratovolcano situated on the island of Montserrat (UK), which is part of the Lesser Antilles islands (16°43' N, 62°11' W, Figure 2.16). The Lesser Antilles island arc was formed by a westward subduction of Atlantic oceanic crust under the Carribbean plate. Volcanic activity at

Montserrat island started in early Pliocene. Five different eruptions centres have been active since then, of which Soufrière Hills is the youngest (*Roobol & Smith 1998, Harford et al. 2003*).

Two historical eruptions are recorded: an early 17th-century eruption, during which Castle peak lava dome was formed, and the ongoing active phase that started 1995. The recent eruption started with long-term small-to-moderate explosions with ash eruptions starting in 1995, and was later accompanied by dome growth, block-and-ash-flows, pyroclastic flows and surges, and a lateral blast caused by a debris avalanche on Dec 26, 1997. In July and August 1997, a series of pyroclastic flows reached Montserrat's capital Plymouth and almost entirely destroyed it. The 1995-2003 eruptive episode is classified as VEI 3 (*Robertson et al. 1998, Druitt et al. 2002, Siebert & Simkin 2002-*).

The andesites of Soufrière Hills Volcano typically show SiO₂ contents of 58-62 wt%. The solid phase is composed of 60-75 % phenocrysts (> 100 µm), 20-30 % microlites, and rhyolitic glass with SiO₂ contents of 76-79 wt%. The main phenocrysts are plagioclase (30-35 %), amphibole (6-10 %), and orthopyroxene (2-5 %) (*Horwell et al. 2001, Murphy et al. 2000*). The porosity of Soufrière Hills eruptive products range from extremely dense dome rocks (~2.5 vol% porosity) to pumices with ~68 vol%. For this work permeability and fragmentation behaviour have been analysed on three pumice samples.

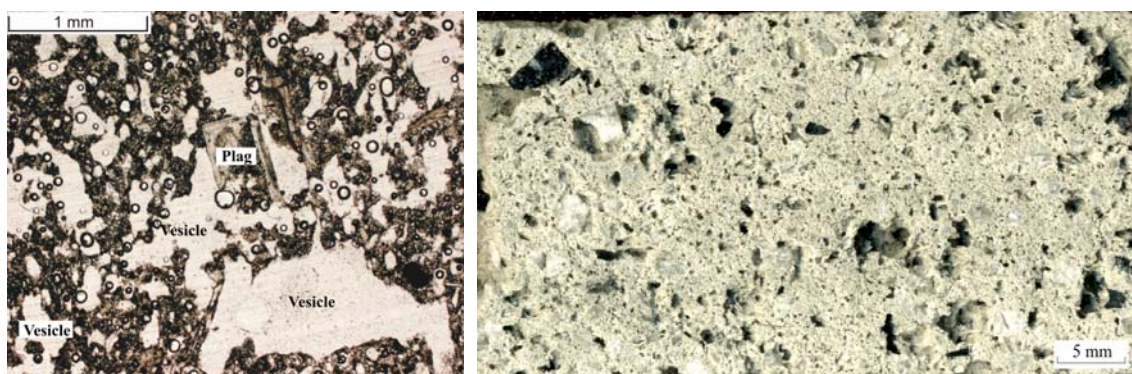


Figure 2.17: Left: The thin section of a Soufrière Hills pumice sample shows irregular vesicles with a high degree of interconnection. The size of the vesicles varies strongly and ranges from a few tens of µm to up to 1.5 mm. Plagioclase and hornblende phenocrysts can reach up to 10 mm and are often fractured. Right: Pumice from Montserrat with ~ 75 vol% porosity. Bubbles are slightly deformed; crystals were often ripped apart during fragmentation (*Kennedy et al. 2005*).

2.1.8 Campi Flegrei, Agnano-Monte Spina, Italy

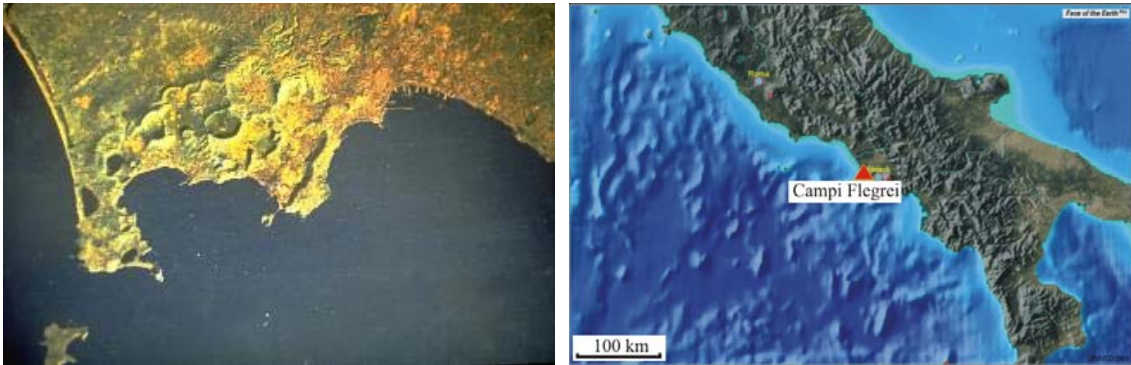


Figure 2.18: Satellite image of the Gulf of Pozzuoli and Naples. The Phlegrean Fields consist of a large caldera with a high number of smaller crater structures inside. Image from National Aeronautical and Space Administration (NASA), 1984, map: Face of the Earth™.

The Campi Flegrei ('Phlegrean Fields') represent a 13-km-wide caldera structure situated on the Gulf of Pozzuoli, on the western outskirts of Naples (40°49' N, 14°8' E). The caldera is a convoluted structure resulting from two main collapses, related to the formation of the Campanian Ignimbrite, 37,000 yBP, and the Neapolitan Yellow Tuff, 12,000 yBP. Following the last caldera collapse, about 60 eruptions have taken place from various subaerial and also submarine vents. Three major phases of activity took place in younger history: 12,000-9500 yBP, 8600-8200 yBP, and 4800-3800 yBP. The Agnano-Monte Spina (AMS) eruption occurred during the last major eruptive episode, about 4100 yBP, and represents the highest-magnitude eruption of this phase (VEI 5). Two eruptions have occurred in historical time: one at Solfatara in the founding year of the city of Munich (1158), and one in 1538 at Monte Nuovo (*Orsi et al.* 1996, *De Vita et al.* 1999, *Siebert & Simkin* 2002-).

Permeability and fragmentation investigations have been performed on pumices of the 4100 yBP AMS eruption. Products of this event are generally classified as trachytes to alkali-trachytes, with SiO₂ contents between ~58.5 wt% and ~61.0 wt%, and (Na₂O + K₂O) contents between ~11.3 wt% and ~12.4 wt%. The pumices are of porphyritic texture, with phenocrysts of plagioclase and alkali-feldspar, clinopyroxene, biotite, and apatite (*De Vita et al.* 1999). The porosity of the pumices ranges between 69 and 84 vol% (Figure 2.19).

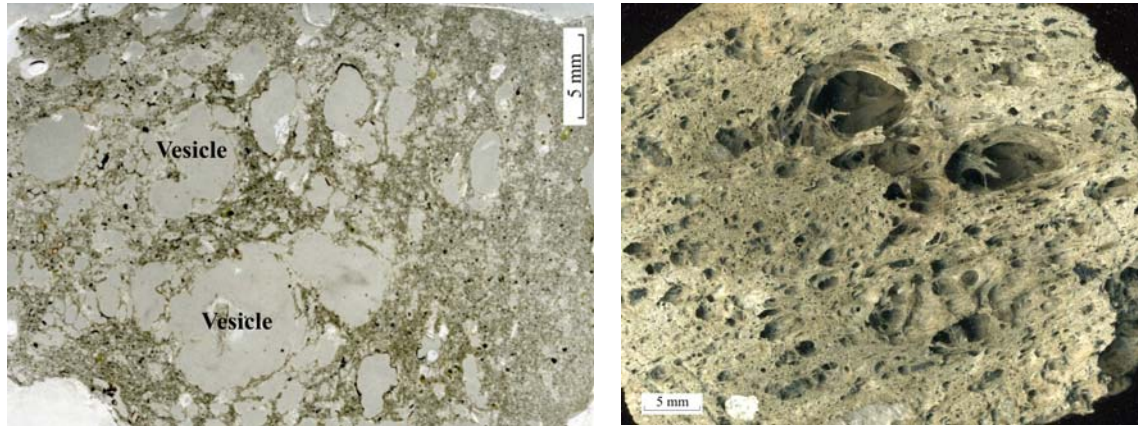


Figure 2.19: Left: Thin section of an Agnano-Monte Spina pumice with ~80% porosity. The pumice is highly inflated, large vesicles can reach cm-scale in these samples and are highly coalesced. A smaller vesicle population ranges between 30 and 100 μm . Plagioclase and clinopyroxene represent the dominant phenocryst phases. Right: Pumice sample with a highly inflated central part.

2.1.9 Stromboli, Italy



Figure 2.20: Stromboli, the NE-most of the Aeolian islands, seen from the west. Photo by *Guiseppina Kysar*, 1999 (Smithsonian Institution), map: Face of the Earth™.

Stromboli is a 924 m high stratovolcano which forms the NE-most of the Aeolian islands in the Tyrrhenian sea ($38^{\circ}47' \text{ N}$, $15^{\circ}12' \text{ E}$; Figure 2.18). It is characterized by persistent mild explosive activity (and is actually eponymous for this kind of eruptive behaviour), with occasional major explosions and paroxysms, and lava flows. The VEI for this kind of activity is specified to 2 (*Siebert & Simkin 2002-*).

The composition of Stromboli pumices and scoriae has remained relatively constant since the beginning of the ‘Strombolian activity’ between the 3rd and 7th century AD. Silica contents range in the order of 48.2 wt% and 51.5 wt%, K_2O contents are generally high with values between 1.5 wt% and 2.5 wt%. This classifies

Strombolian eruptive products as high-K to shoshonitic basalts, with a prevalence of the latter (Rosi *et al.* 2000, Francalanci *et al.* 2004).

In this study, pumices and scoria samples (Figure 2.21) with porosities ranging from 50 vol% to 81 vol% have been investigated.

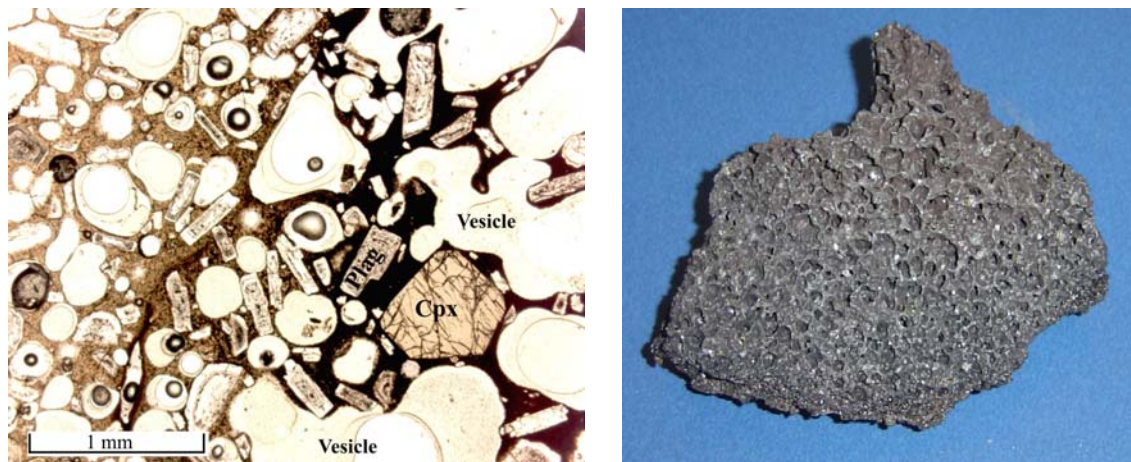


Figure 2.21: Left: Thin section of Stromboli scoria under non-polarized light. The vesicles are spherical to regularly rounded and range between $\sim 100 \mu\text{m}$ to several mm. A small vesicle fraction is not present. The phenocryst phase is represented mainly by plagioclase and pyroxenes. Right: Typical high-vesicular scoria sample from Stromboli. The length of this sample is $\sim 8 \text{ cm}$, its porosity 58 vol%.

2.1.10 Monte Pilato, Lipari, Italy

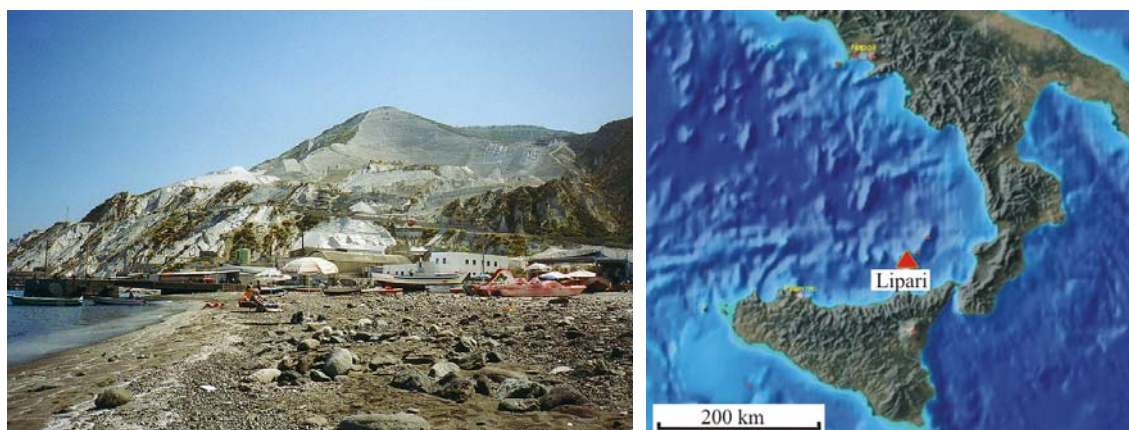


Figure 2.22: Aquacalda pumice mine on Monte Pilato, located on the north coast of Lipari island, the largest of the Aeolian islands. Map: Face of the Earth™.

Lipari is the largest of the Aeolian islands and is located north of Vulcano island ($38^{\circ}20' \text{ N}$, $14^{\circ}57' \text{ E}$). It is entirely formed of volcanic material, and contains numerous small stratovolcanoes, craters and lava domes. The island was formed in three major

eruptive cycles: The first from 223 to 188 kyBP, the second 102-53 kyBP, including the formation of Monte St. Angelo stratovolcano, and the third cycle from 40 ky to present. This last period included the eruption of the Monte Guardia sequence 22,600-16,800 yBP, and the latest eruptive activity on Lipari, the Monte Pilato eruption in the 6th to 7th century AD. This eruption produced several layers of surge and pumice deposits (Figure 2.22) and in its last stage formed the Rocche Rosse obsidian flow (*Dellino & La Volpe* 1995, *Siebert & Simkin* 2002-).

The eruptive products of the Monte Pilato eruptive sequence are rhyolitic with ~74.3 wt% SiO₂, ~4.1 wt% Na₂O and ~4.7 wt% K₂O (*Gioncada et al.* 2003). Pumices and foamed rhyolites used for permeability and fragmentation analyses are brownish to light grey and show porosity values between 35 vol% and 80 vol%. Vesicles are predominantly elongated in flow direction (Figure 2.23).

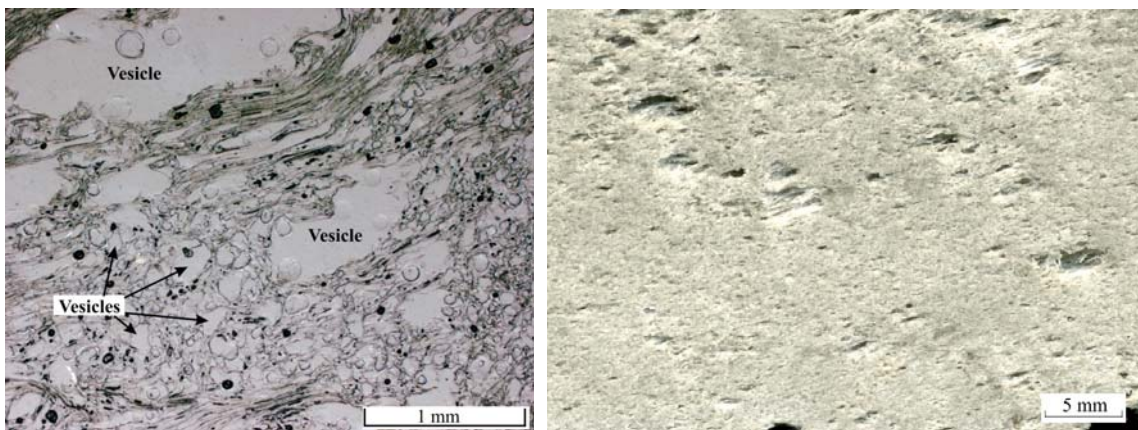


Figure 2.23: Left: Thin section of a Lipari pumice under simply polarized light. The crystal-poor rhyolite shows vesicles of various size populations, ranging from ~ 30 μm to several mm. Vesicles are in some places strongly deformed by shearing and are elongated in a preferred direction. Right: Pumice from Aquacalda pumice mine. The porosity of this variety is about 57 vol%. The major portion of the vesicles is small (< 200 μm). The samples are generally poor in crystals.

2.1.11 Santorini, Greece

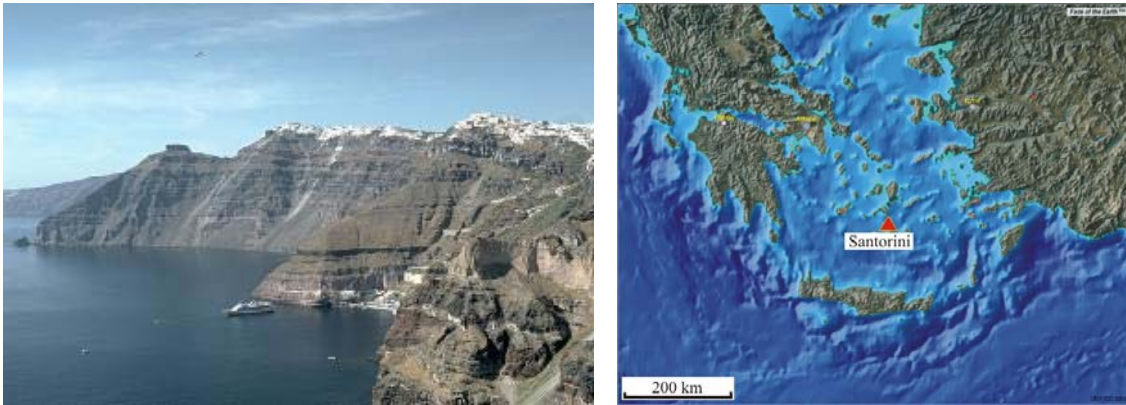


Figure 2.24: The southern crater rim of the Santorini caldera, with the city of Thera on top. Santorini is part of the Cyclades islands in the Aegean sea. Photo by *Lee Siebert*, 1994 (Smithsonian Institution). Map: Face of the Earth™.

Santorini is an active volcanic island group in the South Aegean Volcanic arc ($36^{\circ}24' \text{ N}$, $25^{\circ}23' \text{ E}$; Figure 2.24). It consists of the islands Thera, Therasia, Aspronisi, and Palea Kameni and the intra-calderic island of Nea Kameni. Santorini is build of several overlapping volcanoes, cut by four different caldera structures. The oldest of these calderas formed 180,000 years ago, the youngest ~ 3600 yBP in the course of the Late-Bronze-Age Minoan eruption. The latest eruptive activity was 1950 and produced a small lava dome on Nea Kameni (*Druitt et al.* 1989, 1999; *Pfeiffer* 2001; *Siebert & Simkin* 2002-).

The 1640 BC Minoan eruption was a VEI 6 plinian caldera forming eruption that produced about $6.3 \times 10^{10} \text{ m}^3$ of tephra. The resulting pumices are mostly white to pinkish in colour and of rhyodacitic composition ($\sim 70.9 \text{ wt\% SiO}_2$, $4.9 \text{ wt\% Na}_2\text{O}$, and $3.1 \text{ wt\% K}_2\text{O}$). They contain 3-20 wt% euhedral to subhedral phenocrysts, set in vesicular glass. Glasses show SiO_2 contents ranging from 73.4 to 75.0 wt% (*Druitt et al.* 1999, chapter 4). The pumices investigated in this work derive from western Thera island and range between 78.3 and 84.4 vol% porosities (Figure 2.25).

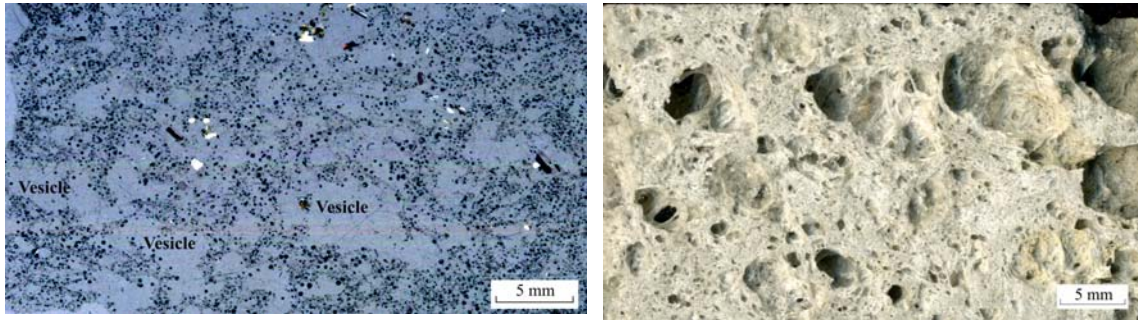


Figure 2.25: Left: Santorini Minoan pumice thin section of suboptimal quality (the black dots are grinding material). Large vesicles are often highly expanded to cm-scale and coalesced. The material is generally poor in crystals (3-20 wt% phenocrysts; *Druitt et al.* 1999), with plagioclase and orthopyroxene as the major phenocrysts. Right: Close view of a light-grey Santorini pumice (~85 vol% porosity) from the Minoan eruption ~1640 BC.

2.1.12 Mt. Unzen, Japan

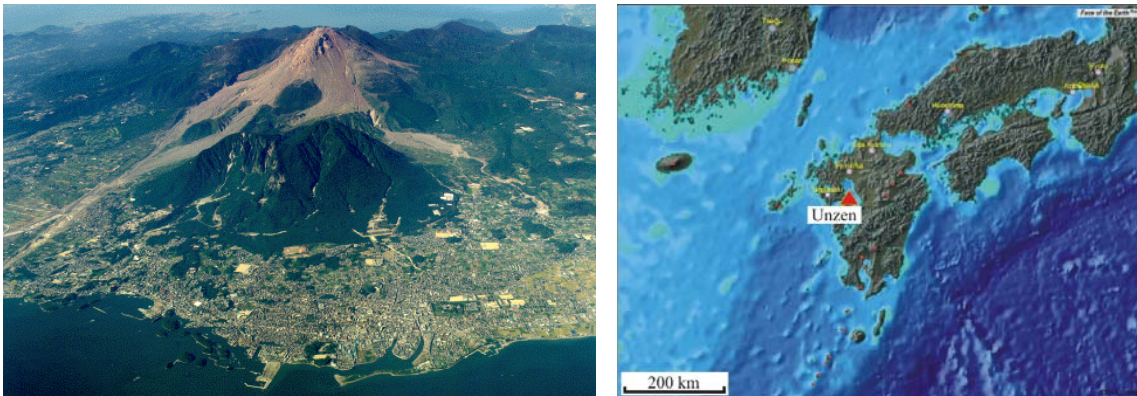


Figure 2.26: Aerial photograph of Unzen volcanic complex, taken from the east, with pyroclastic flow deposits of the 1990-95 eruption. Mt. Unzen is located on Kyushu, the southernmost Japanese islands; Photo from Unzen-Decade Volcano page, taken on Oct. 13, 1995 by Nagasaki Photo Service, Map: Face of the Earth™.

Unzen volcano is situated on Shimabara peninsula on Kyushu, the southernmost of the four major Japanese islands (32°45' N, 130°17' E, elevation ~1500 m asl; Figure 2.26). It is located in a volcanotectonic back-arc depression, known as the Unzen Graben, and its activity is related to a steep subduction of the Philippine Sea Plate below the Eurasian Plate. Three complex stratovolcanoes, Kinugasa on the north, Fugen-dake at the east-center, and Kusenbu on the south, form the andesitic-to-dacitic Unzen volcanic complex. Onset of volcanic activity in the Unzen region was about 500 ky ago. Active phases, comprising mainly lava dome growth, around Mt. Fugen (the central

peak of Unzen volcano) occur every 4000-5000 years. Historical eruptions are reported from 1663, 1792, and 1990-95. (Nakada *et al.* 1999, Siebert & Simkin 2002-)

The samples investigated here derive from the 1990-95 eruptive phase. This eruption started on 17 November 1990 with small phreatic explosions. The first lava extrusion occurred in May 1991 and continued until February 1995, with varying extrusion rates. Dome growth was accompanied by frequent dome collapse events and resulting pyroclastic flows (one of which lead to 43 fatalities on 3 June 1991), and few minor explosive events. The VEI of this eruptive episode is 1 (Nakada *et al.* 1999, Siebert & Simkin 2002-).

The SiO₂ content of dome lavas remained relatively constant throughout the 1990-95 eruption, at ~65 wt%. With a total alkali content around 6.0 wt%, the rocks are classified as dacites according to Le Bas *et al.* 1986. The dome rocks are porphyritic with 23-28 vol% phenocrysts (Nakada & Motomura 1999). The phenocrysts are predominantly idiomorphic plagioclase (An₄₀₋₅₀), hornblende, and biotite, and exhibit average sizes of about 5 mm but can reach up to 2 cm. The porosity of the erupted material ranges from ~3 vol% at the very dense dome rocks up to 54 vol% at breadcrust-bombs. The pores can reach up to 2 cm in size and are very irregular in shape and often attached to phenocrysts. The rocks are irregularly pervaded by systems of macroscopic fractures. Field density measurements on 37 sites have been performed during two field campaigns in 2000 and 2001 by U. Kueppers, B. Scheu, O.Spieler and J. Gottsmann.

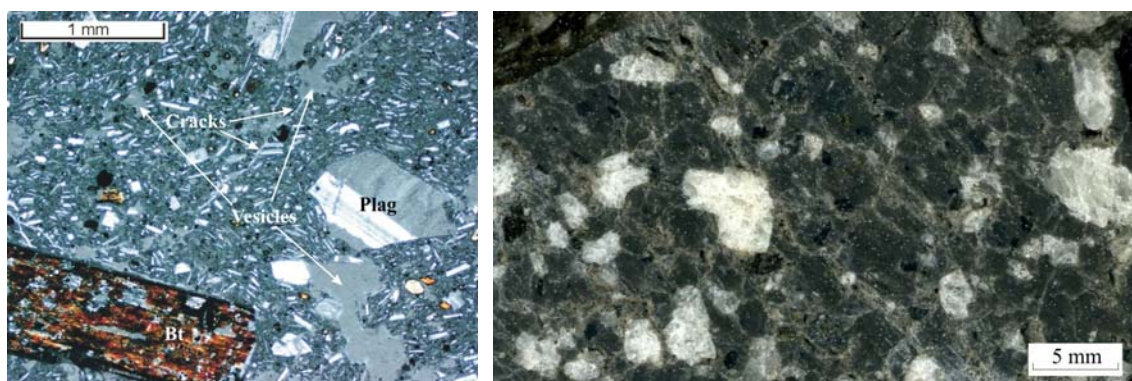


Figure 2.27: Left: Thin section of a dense (~5 vol% porosity) porphyritic Unzen dome rock. Plagioclase, biotite, and hornblende phenocrysts can reach sizes of >1 cm, pyroxenes and oxides are minor components. The groundmass is highly crystalline with mainly plagioclase microlites of up to 50 μ m. Vesicles in this rock variety are generally small (few are greater than 2 mm), highly deformed, and often attached to existing crystals. The samples are often interlaced with fractures and microcracks. Right: Polished surface of an Unzen dacitic dome rock. The samples are often pervaded by a complex network of fractures. Phenocrysts are generally large.

2.1.13 Pinatubo, Philippines

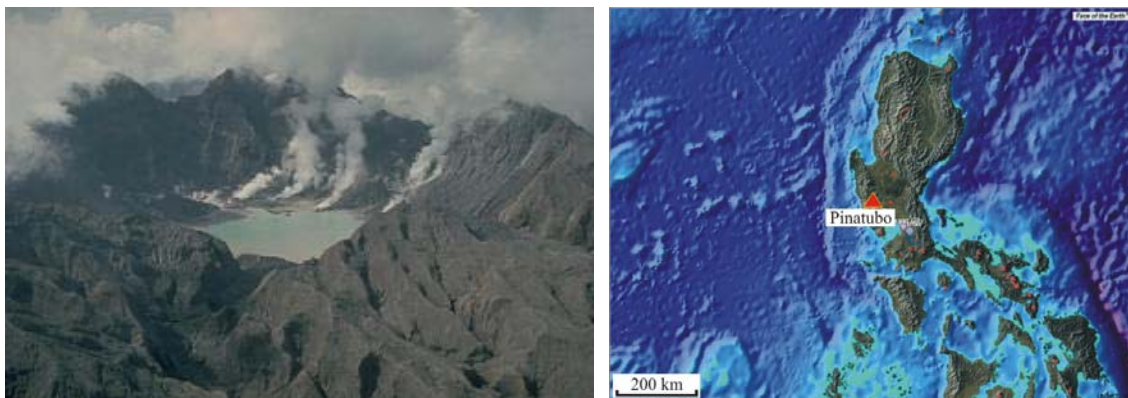


Figure 2.28: The remnants of Pinatubo volcano after the 1991 plinian eruption. Pinatubo is situated on western central Luzon island, Philippines. Photo by Chris Newhall, 1991 (U.S. Geological Survey), map: Face of the Earth™.

Mt. Pinatubo is a stratovolcano located approximately 100 km NW of Manila, central Luzon island, Philippines (15°8' N, 120°21' E; Figure 2.28). At least six major eruptive periods are documented from modern Pinatubo volcano during the last 35,000 years. However, it is most famous for its recent VEI 6 plinian eruption in 1991, one of the world's largest of the 20th century. This eruption formed a 2.5 km-wide summit crater, reduced the mountains height from 1745 to 1486 m, and ejected about 1.1×10^{10} m³ of tephra. During the climactic phase of the eruption, solely dacitic magma was ejected (~65 wt% SiO₂), producing basically two varieties of dacitic pumices: a white (phenocrysts-rich) and a grey (phenocrysts-poor) type (Figure 2.29; *Hoblitt et al* 1996, *Pallister et al.* 1996, *Hammer et al.* 1999, *Siebert & Simkin* 2002-). These two varieties have been used for laboratory experiments, the determined porosities range from 55 to 78 vol%.

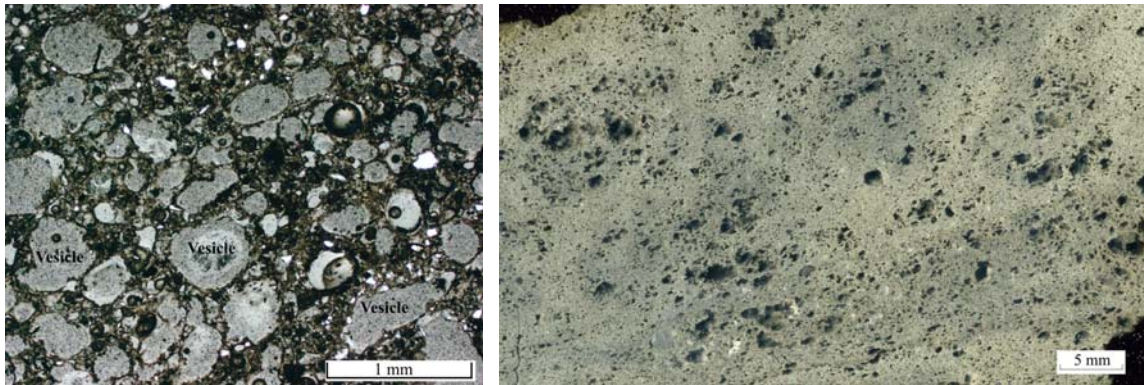


Figure 2.29: Left: Thin section of a grey (crystal poor) pumice of the 1991 eruption of Mt. Pinatubo. Many vesicles have spherical shapes. The larger vesicle population has diameters of 300-600 μm , small vesicles are $\sim 50 \mu\text{m}$. Phenocrysts (mainly plagioclase) are generally small. Right: Pinatubo grey pumice with $\sim 75 \text{ vol}\%$ porosity. Bubbles are often spherical and generally small, as well as the variability of bubble sizes.

2.1.14 Sample overview

Table 2.1: Overview of the samples used for permeability and/or fragmentation experiments

Sample	Origin	Eruption	Rock type	Av. Porosity [%]
LIP B	Lipari	Mte. Pilato, 6 th /7 th AD	Rhyolite, Pumice	57.0
LIP C	Lipari	Mte. Pilato, 6 th /7 th AD	Rhyolite, Pumice	69.3
LIP E	Lipari	Mte. Pilato, 6 th /7 th AD	Rhyolite, Pumice	38.5
LIP F	Lipari	Mte. Pilato, 6 th /7 th AD	Rhyolite, Pumice	79.8
MUZ 2000 A	Mt. Unzen	1990-95	Dacite, Dome/ BAF	4.3
MUZ 2000 D	Mt. Unzen	1990-95	Dacite, Dome/ BAF	16.2
MUZ 2000 E	Mt. Unzen	1990-95	Dacite, Dome/ BAF	16.6
MUZ 2000 G	Mt. Unzen	1990-95	Dacite, Dome/ BAF	34.5
MUZ 2001 A	Mt. Unzen	1990-95	Dacite, Dome/ BAF	7.1
MUZ 2001 B	Mt. Unzen	1990-95	Dacite, Dome/ BAF	5.7
MUZ 2001 C	Mt. Unzen	1990-95	Dacite, Dome/ BAF	21.3
MUZ 2001 F	Mt. Unzen	1990-95	Dacite, Dome/ BAF	35.6
MUZ BKB	Mt. Unzen	1990-95	Dacite, Breadcrust Bomb	43.6
MUZ VUL 01	Mt. Unzen	1990-95	Dacite, Breadcrust Bomb	47.1
MP A	Merapi	1990-2002	Andesite, BAF	14.0
MP B	Merapi	1990-2003	Andesite, BAF	35.5
MP C	Merapi	1990-2004	Andesite, BAF	45.5
CF S	Campi Flegrei	Agnano-Monte Spina	Trachyte, Pumice	75.6
SNT	Santorini	Minoan	Rhyodacite, Pumice	82.3
STR_Br	Stromboli	2003	Basalt, scoria	61.5

Sample provenance and preparation

STR Bi	Stromboli	2003	Basalt, Pumice	75.0
PIN A	Pinatubo	1991	Dacite, crystal-poor pumice (grey)	61.0
PIN B	Pinatubo	1991	Dacite, crystal-rich pumice (white)	65.0
PIN C	Pinatubo	1991	Dacite, crystal-rich pumice (dark-grey)	57.4
PIN GFL	Pinatubo	1991	Dacite, crystal-poor pumice (grey)	75.4
MTSR	Montserrat	1995-recent	Andesite, Pumice	74.0
Au B1	Augustine	1986	Andesite, dark-grey BAF	9.4
Au C1	Augustine	1986	Andesite, black BAF	38.0
Au P4	Augustine	1986	Andesite, Pumice	70.0
Au P1	Augustine	1986	Andesite, Pumice	48.0
Co C6	Colima	1999	Andesite, BAF	15.0
Co D2	Colima	1999	Andesite, BAF	22.0
Co E4	Colima	1999	Andesite, BAF	44.0
Co P3	Colima	1913	Andesite, Pumice	62.0
Co P4	Colima	1913	Andesite, Pumice	64.6
Be B1	Bezymianny	1956	Andesite, Pyroclastic flow deposit	25.2
Be C3	Bezymianny	1956	Andesite, Pyroclastic flow deposit	38.3
Be D2	Bezymianny	2000	Andesite, BAF	45.4
Be E1	Bezymianny	2000	Andesite, BAF	50.9
Ke C3	Kelut	1991	Basaltic andesite	28.0
Ke D4	Kelut	1991	Basaltic andesite	47.8
Ke D9	Kelut	1991	Basaltic andesite	47.3
Kr A11	Anak Krakatau	recent	Basaltic andesite lava	22.7
Kr D4	Anak Krakatau	recent	Basaltic andesite lava	41.5
Kr E6	Anak Krakatau	recent	Basaltic andesite scoria	65.2
Kr S2	Krakatau	1883	Rhyodacite, Pumice	73.4
Kr R4	Krakatau	1883	Rhyodacite, Pumice	84.4
Kr TP	Krakatau	?	Rhyodacite, Tube pumice	78.1

2.2 Sample preparation

In most instances the experiments have been conducted on coplanar cylindrical shaped samples with a diameter of 25 mm and varying lengths of up to 60 mm (Figure 2.30). In order to cover a widest possible range in textural and chemical properties, samples have been chosen to derive from (a) different types of pyroclastic deposits including dome rocks, pumices, scoriae and breadcrust bombs and (b) different volcanic settings (see chapter 2.1). The sample cylinders were drilled from the clasts parallel to a macroscopically detectable flow alignment, in order to possibly reproduce an original orientation. Subsequently the samples were cut and polished to the desired length.



Figure 2.30: Pumice clast with a drilled sample cylinder. Height of the cylinder is 60 mm, the diameter is 25 mm.

2.3 Laboratory porosity determination

For this study, porosity values were determined in the laboratory using a helium pycnometer (high precision) and directly in the field (high number) according to the method for field density measurements described by *Kueppers et al. 2005*. The latter method will be described in Chapter 3.2.



Figure 2.31: Density and porosity of the samples were determined in the laboratory using a helium pycnometer (Micromeritics AccuPyc 1330).

To determine the volumetric fraction of the accessible (“open”) and total (“open” + “closed”) pore space of a sample cylinder in a non-destructive manner, a helium-pycnometer (Micromeritics AccuPyc 1330) has been used (Figure 2.31). The measuring method is based on the exact determination of the amount of Helium gas displaced by a samples solid phase volume. A weighed sample (as powder, fragments, or in well defined geometries) is therefore placed in a test cell with known volume. The gas pressures observed upon filling the measuring chamber and then discharging it into a second empty chamber allow the determination of volume displaced. Since helium atoms rapidly fill the tiniest pores of the sample, only the truly solid phase (or matrix) and the non-accessible pores of the sample are excluded from gas infiltration. If the mathematical volume of the sample cylinder (= total porosity + matrix) is known, then

the volumetric fraction of the rocks open porosity (Φ_{op}) can be achieved easily according to

$$\Phi_{op} = (V_{math} - V_{pyc})/V_{math}, \quad (2.1)$$

with V_{math} being the measured mathematical volume and V_{pyc} the volume determined by the pycnometer (i.e. matrix + isolated pores). The density ρ_m of the samples matrix (including the closed porosity) can then be calculated via

$$\rho_m = m_s/V_{pyc}, \quad (2.2)$$

with m_s being the mass of the sample, its bulk density ρ_b is

$$\rho_b = m_s/V_{math}. \quad (2.3)$$

To determine a rocks total and closed porosity, a portion of the material is milled to a fine powder in order to open all the closed pore sections. The density ρ_p of the powder represents the samples matrix density excluding the closed pores, so the total porosity is obtained with

$$\Phi_{tot} = (\rho_p - \rho_b) / \rho_p. \quad (2.4)$$

3 Field porosity investigations

3.1 Introduction

Investigations of explosive volcanism and the modelling of related processes require profound knowledge of the physico-chemical properties of the rock material involved. Vesicularity and density highly influence the rheological properties as well as the fragmentation behaviour of the magma. Since the overpressurized gas in the pore space is considered to be one of the driving forces of an explosive eruption, the porosity distribution of erupted pyroclasts may reflect the degree of a volcano's explosivity, and give valuable insights into pre-eruptive conditions of a volcanic conduit.

Direct observation of volcanic conduit rocks is restricted to the investigation of eroded edifices (which, due to their age, are often highly chemically and physically altered), or drilling projects (which represent a major technical challenge and are exceedingly expensive). It can be assumed that within the volcanic edifice the physical and textural properties of silica-rich magma are, due to high melt viscosity, subject to only minor changes. Hence information on the temporal variability of the ascending magma's vesicularity can be easiest achieved via the measurement of a statistically reliable amount of representative erupted samples (*Kueppers et al. 2005*).

In order to relate density/porosity distributions of eruptive products to specific volcanic settings and eruption characteristics, the results of field campaigns on seven volcanoes of the circum-Pacific area ("Ring of Fire") have been evaluated and compared. The density of more than 3200 pyroclastic-flow and block-and-ash-flow samples of St. Augustine (Alaska), Bezymianny (Kamchatka), Unzen (Japan), Merapi, Kelut, Krakatau (all Indonesia) and Colima (Mexico) were measured directly in the field. Data from Unzen derive from 2000 and 2001 field campaigns by U. Kueppers, B. Scheu, O. Spieler and J. Gottsmann (published in *Kueppers et al. 2005* and *Kueppers 2005*), Merapi density data have been measured in 2002 by B. Scheu and L. Schwarzkopf. Kelut and Krakatau have been investigated by O. Spieler, D. Richard and S. Kremers in 2005. In addition, density data from *Hoblitt & Harmon (1993)* of the 1980 Mt. St. Helens eruption have been used for comparison.

3.2 Field based porosity determination

The total porosity of samples is easily acquired by measuring its bulk density. If then the mean density of the solid phase (the matrix density ρ_P as defined in Chapter 2.3) of the material is known, the sample's porosity can be calculated according to equation (2.4). To determine of the matrix densities a representative number of samples from each volcano (or, if it obviously represents an exceptional depositional environment, also from a single measurement site) have been grinded to powder. The density of the powder was measured with the helium pycnometer (see Chapter 2.3). The mean density value was then used to calculate each rock's porosity.

Density measurements of porous media usually involve time-consuming procedures like water saturation (e.g. *Belikov et al.* 1964, *Schopper* 1982) or surface impregnation/ coating (e.g. *Houghton & Wilson* 1989, *Polacci et al.* 2003), or they are done via pycnometric methods (e.g. Chapter 2.3). All these measurements are commonly done in the laboratory, and require sampling and sample transportation. However, in order to reliably evaluate the density distribution of volcanic deposits, an adequate number of measuring locations, as well as a statistically reliable amount of samples measured per location is required. A number of 60 measurements per spot was found to meet this requirement. Since transportation of this amount of samples with a total weight of several hundreds of kg per volcano would represent a disproportionate effort, density measurements were conducted directly in the field.

The measuring setup developed for this purpose (*Kueppers et al.* 2005) is based on the Archimedean principle, which states that the buoyant force of a body is equal to the weight of the displaced fluid. A dry sample's bulk mass therefore must be weighed in air and subsequently under water (Figure 3.1). To prevent water infiltration into the accessible pore space, the samples were placed in plastic bags, which, when evacuated using a battery-powered vacuum pump, tightly cover the samples surface. To keep the vacuum in the plastic bag, it was sealed with silicon glue.

If the density of the water, ρ_{H_2O} , is assumed to be 1 g/cm^3 , the bulk density of the rock can be calculated according to

$$\rho_{\text{sample}} = (m_{\text{air}} / (m_{\text{air}} - m_{H_2O})) \rho_{H_2O}, \quad (3.1)$$

where m_{air} and $m_{\text{H}_2\text{O}}$ are the masses of the sample in air and submerged under water, respectively. The method and required equipment are described in detail in *Kueppers et al.* (2005).

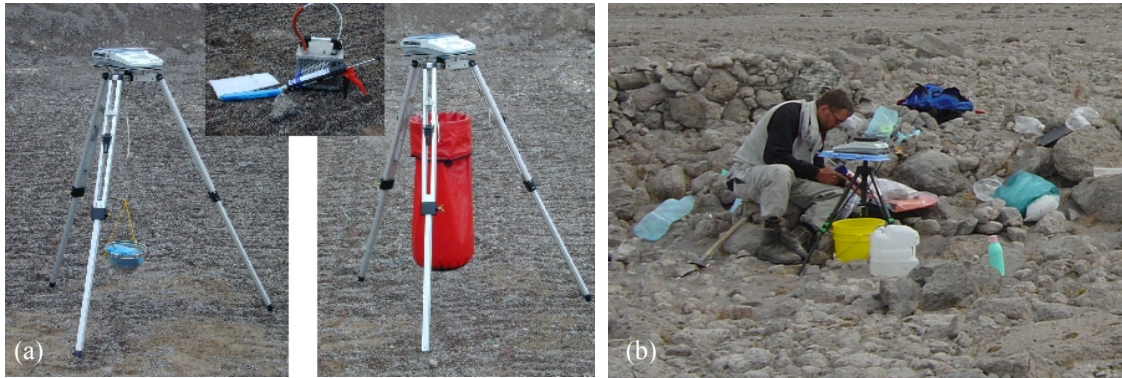


Figure 3.1: (a) The setup used for field density measurements with the battery-powered balance fixed on a tripod and the holding device for the sample (left) inside the waterproof container (right). The inset (top) shows the battery-powered vacuum pump, the silicon injection device and plastic bags. (b) Field density measurements on Augustine Island.

3.3 Field porosity measurements – results

3.3.1 St. Augustine

Density measurements have been performed on 8 sites within the deposits of the 1986 eruptive phase: 4 sites within pumice flow/ pumiceous pyroclastic flow deposits (PPF; unit 86pp, according to *Waitt & Begét 1996*), 3 sites within lithic pyroclastic flow deposits (LPF; unit 86pl) and one lahar flow deposit (LahF, also unit 86pp) (Figure 3.2). For the porosity determination, an average matrix density of 2.64 g/cm^3 has been measured for the porous pumice flow deposits (LOK 1, 2 and 9), and 2.78 g/cm^3 for the remaining locations.

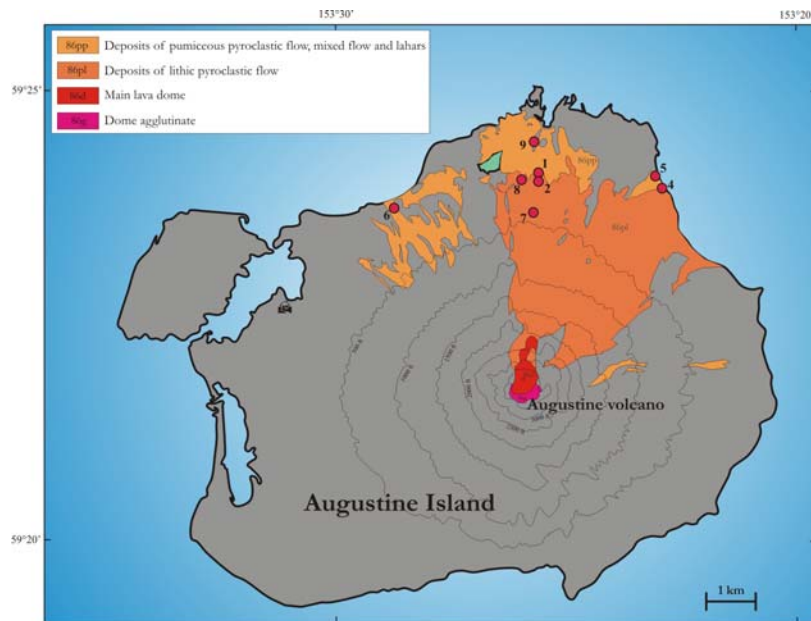


Figure 3.2: Locations of density measurements on Augustine island. LOK 1 and 2 represent pumice flows (levees) within the lithic-rich pyroclastic deposits, LOK 5 and 9 are deposits of pumiceous pyroclastic flows. LOK 4, 7 and 8 are deposits of lithic pyroclastic flows/ block-and-ash-flows, and LOK 6 lahar and “mixed-flow” deposits. Modified from the Geological Map of Augustine Island by *Waitts & Begét 1996*.

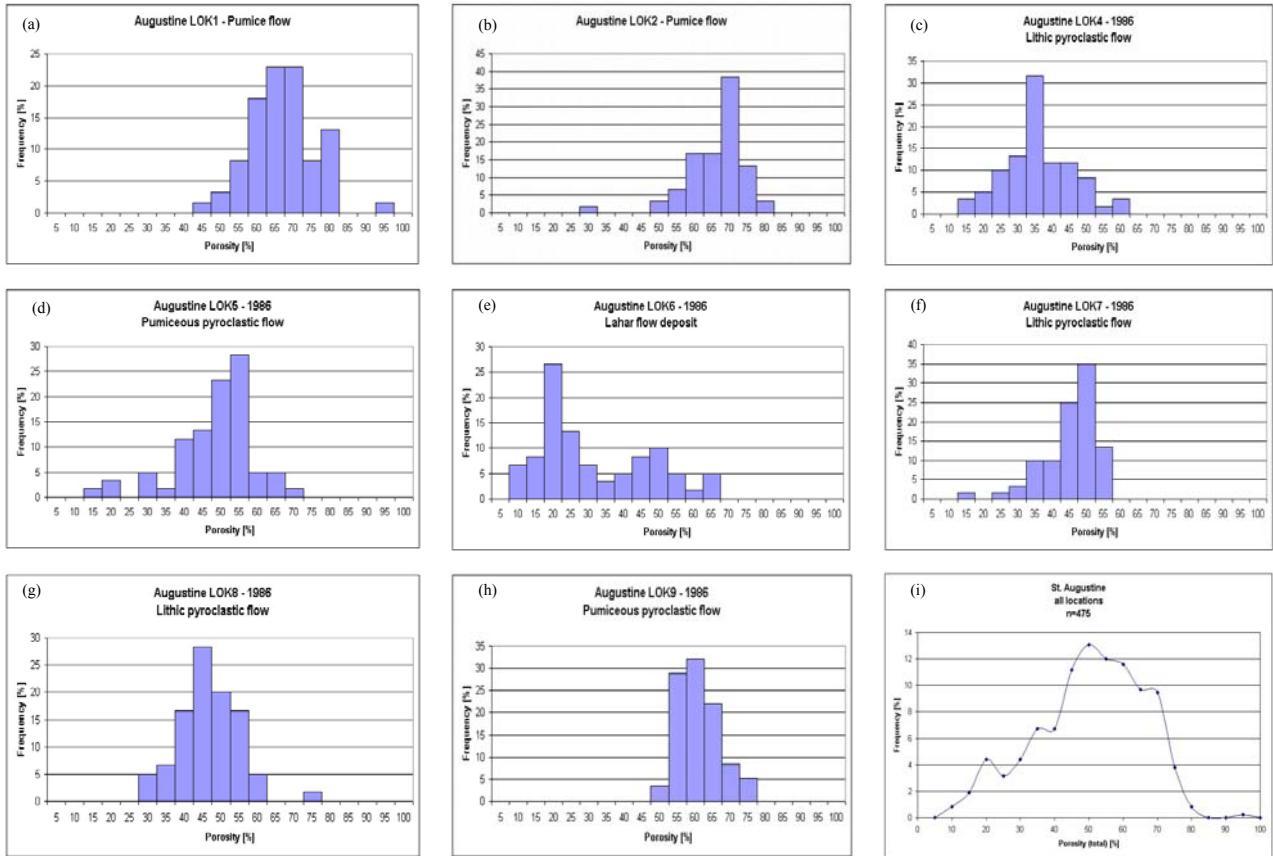


Figure 3.3 (a-h): Porosity distribution of eight locations; fraction of the total amount of measurements plotted in increments of 5 vol%. (i) displays the distribution of the entire data set (n=425).

The porosity distributions of the single locations in Figure 3.3 confirm that different depositional environments yield distinct distributive patterns with different mean- and peak-porosity values. PPF sites show unimodal distributions with mean porosities between 45.5 (LOK 5) and 63.6 vol% (LOK 2). As LOK 5 was close to the shoreline, a post-depositional modification of the porosity distribution by elutriation of low-density particles cannot be excluded. The same accounts for LOK 4. LPF locations also show unimodal patterns, with slightly lower mean porosity values between 33.5 (LOK 4) and 44.5 vol% (LOK 8). The lahar deposit (LOK 6) displays a low mean porosity (28.9 vol%) and an indication of bimodal porosity distribution. Post-deposition fluvial transportation is likely responsible for the depletion of less dense material.

A coherency between mean porosities and the deposit types is evident in Figure 3.4. The entire dataset of Augustine volcano (Figure 3.3 (i)) shows a nearly unimodal and Gaussian porosity distribution, with a porosity peak at ~50 vol%. The mean porosity value is 47.5 vol% and the mean density is 1.44 g/cm³. The comparatively broad character of the distribution curve reflects the diversity of deposit types and

eruptive stages occurring on Augustine volcano: highly explosive activity (VEI 4) with emplacement of pumiceous pyroclastic-flow deposits at the beginning of the eruption, followed by lava dome extrusion with associated block-and-ash flows.

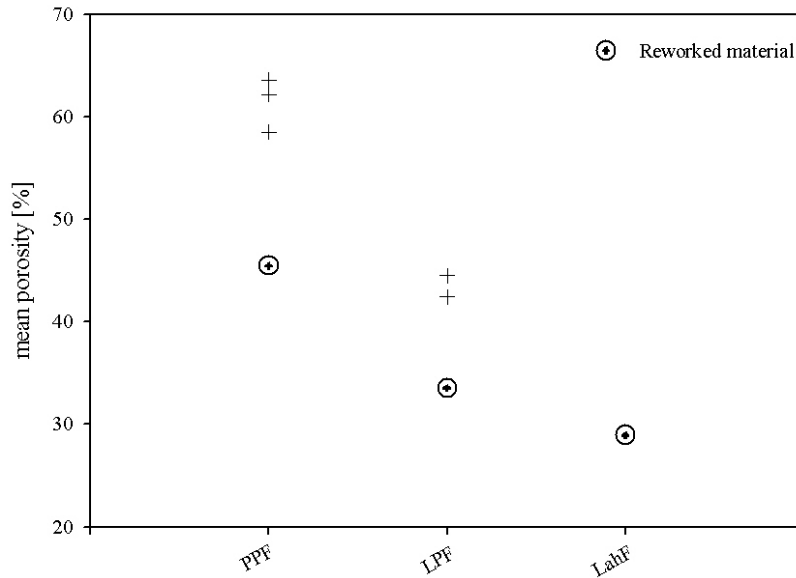


Figure 3.4 Mean porosity values of the 8 locations, subdivided into 3 groups of deposits: Pumice flow/pumiceous pyroclastic flow deposits (PPF), lithic pyroclastic flow deposits (LPF) and lahar flow deposit (LahF). The locations subject to fluvial reworking show a considerable loss of less dense material.

3.3.2 Bezymianny

At Bezymianny volcano, density measurements have been performed on 3 sites within the deposits of the 1956 lateral blast eruption (LOK 3, 5 and 7), and on 2 locations with products of 2000 block-lava effusion and block-and-ash-flow activity (LOK 2 and 6) (Figure 3.5). As mean matrix density for the porosity calculation, 2.67 g/cm^3 has been used for the 1956 eruption samples, and 2.72 g/cm^3 for the 2000 BAF samples.

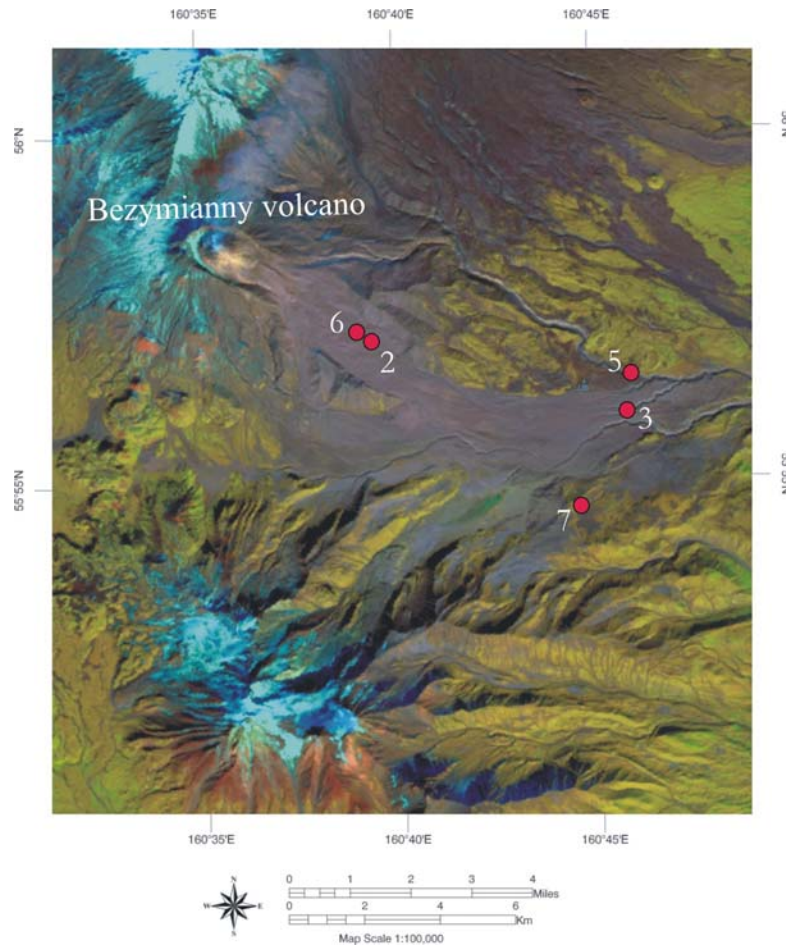


Figure 3.5: LANDSAT image of Bezymianny volcano with the locations of the 5 measurement sites. Locations 3, 5, and 7 represent deposits of the 1956 sector-collapse induced lateral blast event, locations 6 and 2 are BAF deposits of 2000.

Figure 3.6 shows the porosity distributions of the 5 investigated locations. Porosity values range from 10 to 60 vol%, the mean value for all locations is 35.70 vol%, with a mean density of 1.73 g/cm³. All locations of 1956 eruption show a slight bimodal distribution with a maximum at the more porous mode. This pattern is confirmed by the compiled plots of the whole dataset (f) but is more prominent in the 1956-deposits (h). The bimodality of these kind of eruptive products is in good agreement with results of *Hoblitt & Harmon* 1993, who investigated the density distribution of products of the 1980 lateral blast of Mt. St. Helens. They ascribe the bimodal distribution to two distinct vesicle nucleation events: the first population formed during magma ascent and cryptodome formation, the second upon rapid decompression due to the sector collapse. They also conclude that for the early bubble nucleation to occur, the volatile content in the magma has to be greater than a threshold value of 0.2-0.4 wt%. At magma portions with lower bulk water content, the confining pressure during the cryptodome formation

stage hinders gas exsolution and bubble growth. As the eruptive scenario of the 1956 Bezymianny eruption is assumed to be comparable to the Mt. St. Helens 1980 lateral blast, a similar explanation may account for the bimodal porosity distribution of Bezymianny products. The mean values of only the 1956 deposits are 32.4 vol% porosity and 1.80 g/cm³ density.

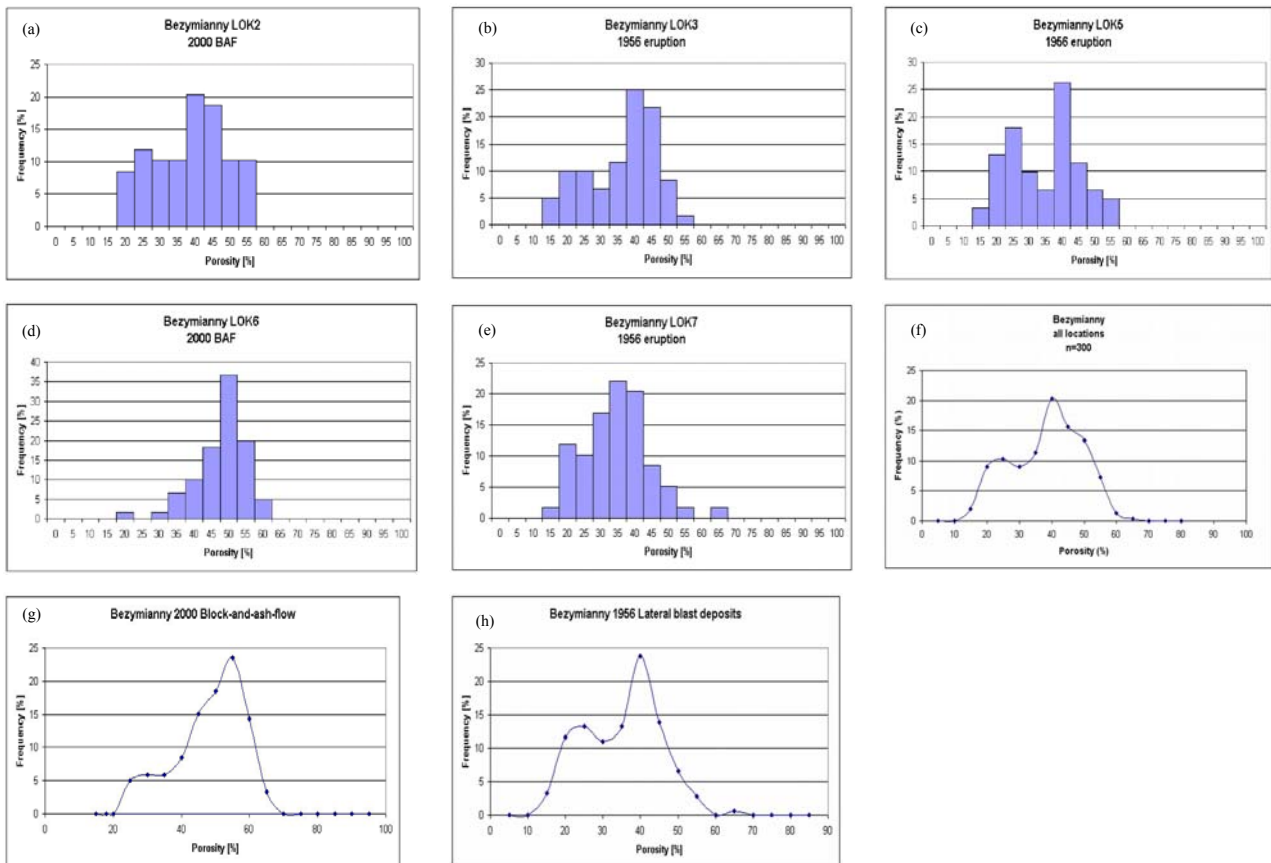


Figure 3.6: Porosity distribution of 5 locations of Bezymianny volcano, plotted in 5 vol%-steps as fraction of the total amount of measurements. (f) displays the distribution of the entire data set ($n=300$), (g) the distribution of the 2000 eruption products, (h) the distribution of only the 1956-eruption samples. A bimodal pattern is evident for all sites of the 1956 eruption.

3.3.3 Colima

Five locations have been measured at Volcán de Colima during two field campaigns in 2004 and 2005. The samples from San Antonio and Cordoban valleys are products of the 1998/99 pyroclastic and block-and-ash-flows; “Montegrande valley” and “LPF” samples are from early the 2005 explosive activity (Figure 3.7). Results show an overall low porosity in which the majority of rocks range between 1 and 30 vol%; a few outliers show porosities up to 63 vol% (Figure 3.8). The mean porosity of the entire dataset is 16.4 vol%, the mean bulk density 2.28 g/cm^3 , and the mean matrix density for the porosity determination 2.73 g/cm^3 . The low mean porosity may be an indication of a low volatile content of the magma, or effective degassing of the magma prior to eruption. These results are in good accordance to the general low water content of recent activity products measured by *Luhr 2002*.

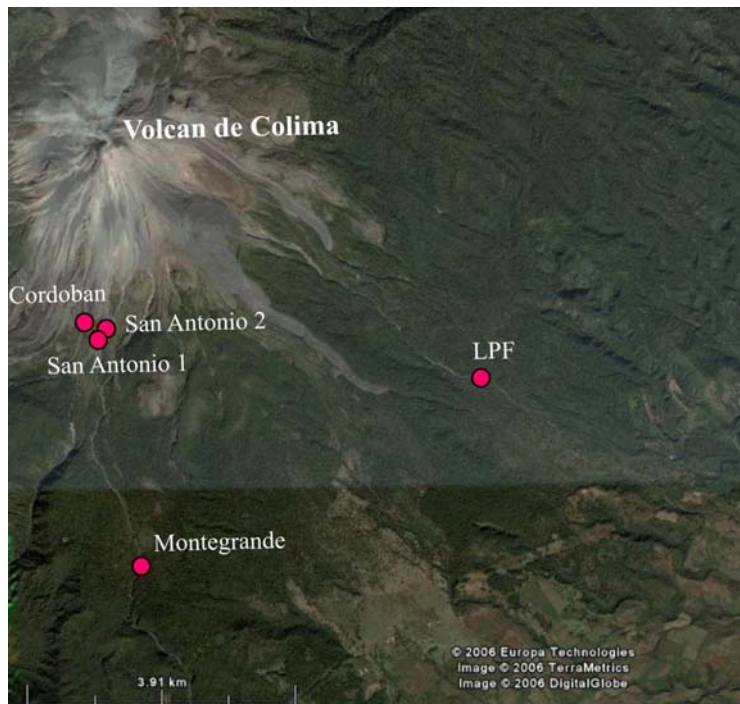


Figure 3.7: Satellite view of Volcán de Colima with the five of the field density measurements. Background image from GoogleEarth™.

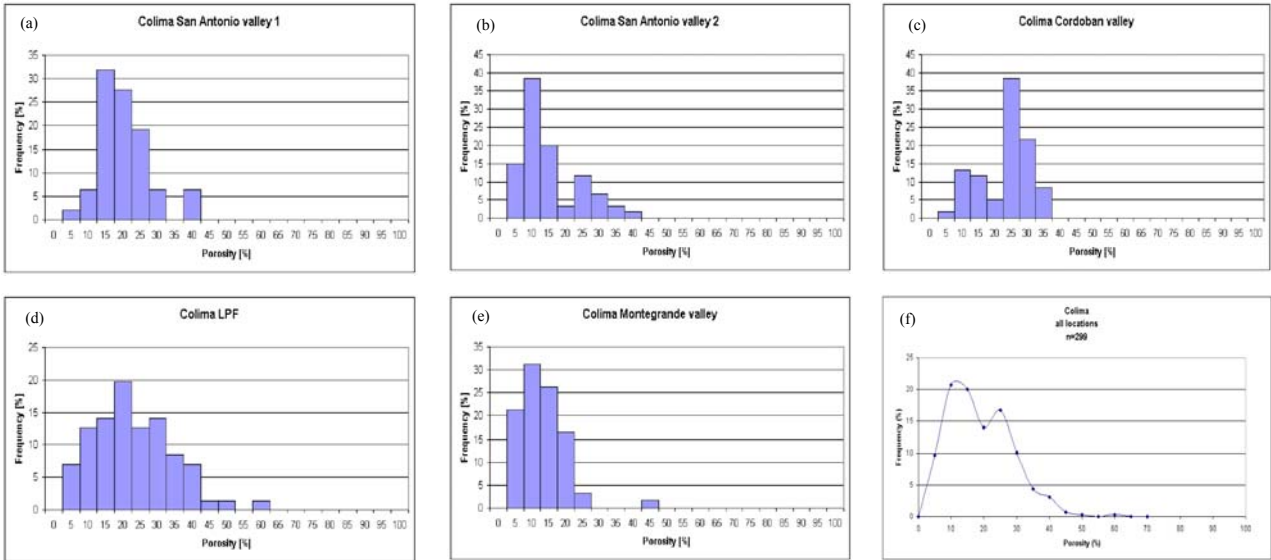


Figure 3.8: Porosity distribution for 5 locations of deposits of 1998/99 and 2005 explosive activity. Porosities are generally low with peaks between 10 and 25 vol%. (b) and (c) show a slight bimodal character with a low at 20 vol%. The compiled dataset of all locations (f) shows a slight bimodality and a mean porosity of 16.4 vol%.

3.3.4 Krakatau

Products of the 1883 explosive eruption of Krakatau volcano have been investigated on 6 sites on the three island surrounding the newly arisen Anak Krakatau island: two locations on Panjang (or Lang) island, three on Rakata island (the remnant of the destroyed Krakatau island) and one on Sertung (or Verlaten) island (Figure 3.9).



Figure 3.9: Satellite image of Krakatau archipelago with the sampling sites on Sertung, Panjang, and Rakata islands. In the centre lies the currently active Anak Krakatau. Background image from GoogleEarth™.

The results show without exception high to very high porosity values (45 to 92 vol%), with narrow unimodal distribution patterns (Figure 3.10). Mean porosity of the entire dataset is at 76.9 vol%, mean density 0.58 g/cm³. The high porosity of the products reflects the high volatile content and explosivity of this eruption.

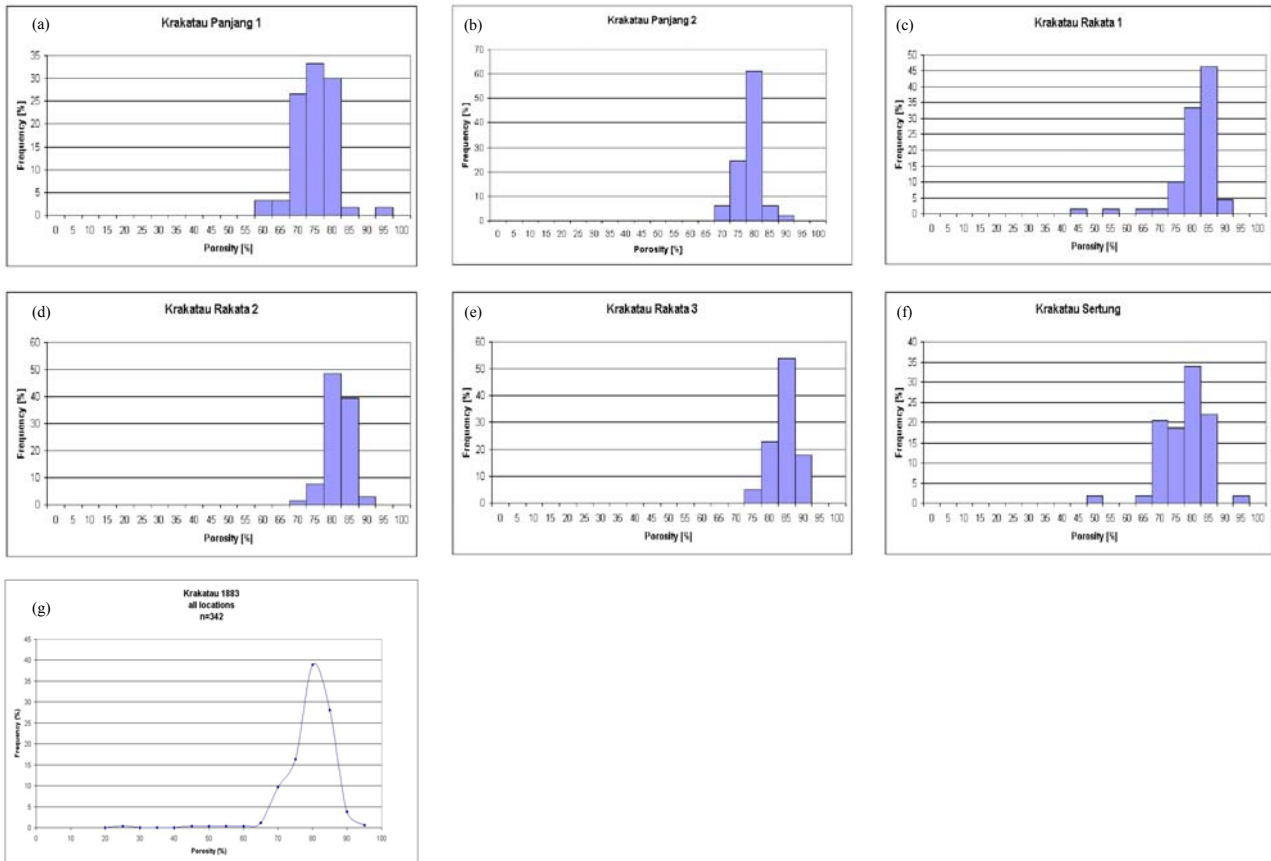


Figure 3.10: Porosity distribution of products of the 1883 plinian eruption, taken from six localities on three islands of the Krakatau archipelago. Porosities are exceptionally high, with peak porosities between 75 and 80 vol%. Porosity data compilation (g) shows a unimodal distribution with a pronounced peak around 80 vol%.

3.3.5 Kelut

On Kelut volcano, three sites with products of the 1990 eruption have been examined (Figure 3.11). This eruption involved melt-water interaction (phreatomagmatic) and a short plinian phase. The results show generally high porosities, and an unimodal distribution, but slightly higher variance than that of Krakatau. The

entire dataset displays an almost Gaussian distribution with a mean porosity at 66.16 vol% (Figure 3.12). The mean density of the samples is 0.93 g/cm³.



Figure 3.11: Satellite image of Kelut volcano showing the three sampling locations R1-3. The outcrops represent pumice and dark scoriaceous pumice deposits from the 1990 explosive eruption. Background image from GoogleEarth™.

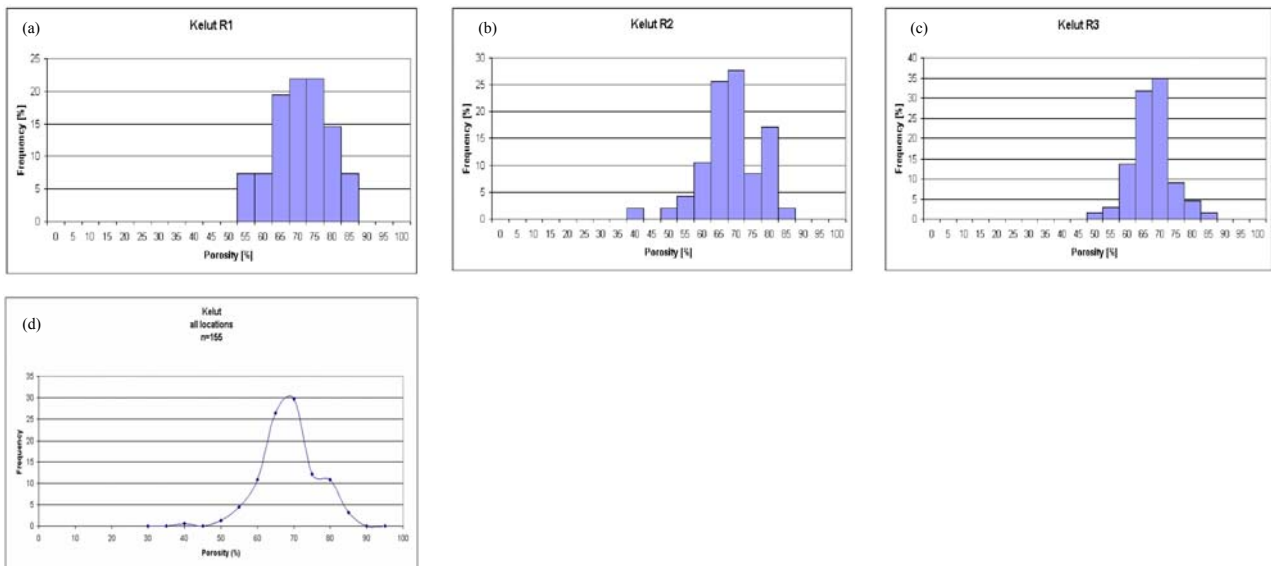


Figure 3.12: Results of porosity determinations on three sites on Kelut’s western flank. The plots show consistent peak abundances at porosities around 70 vol%. Mean porosity of the whole data is 66.16 vol%.

3.3.6 Merapi

Six locations have been investigated in Jurangjero valley on Merapi's western flank: D1-3 represent sites within the lower, middle and upper unit of a 1998 block-and-ash-flow deposit, respectively. D4-6 were equally sampled on a more proximal position of the same flow (Figure 3.13). For the calculation of porosity a mean matrix density of 2.82 g/cm^3 has been assumed.

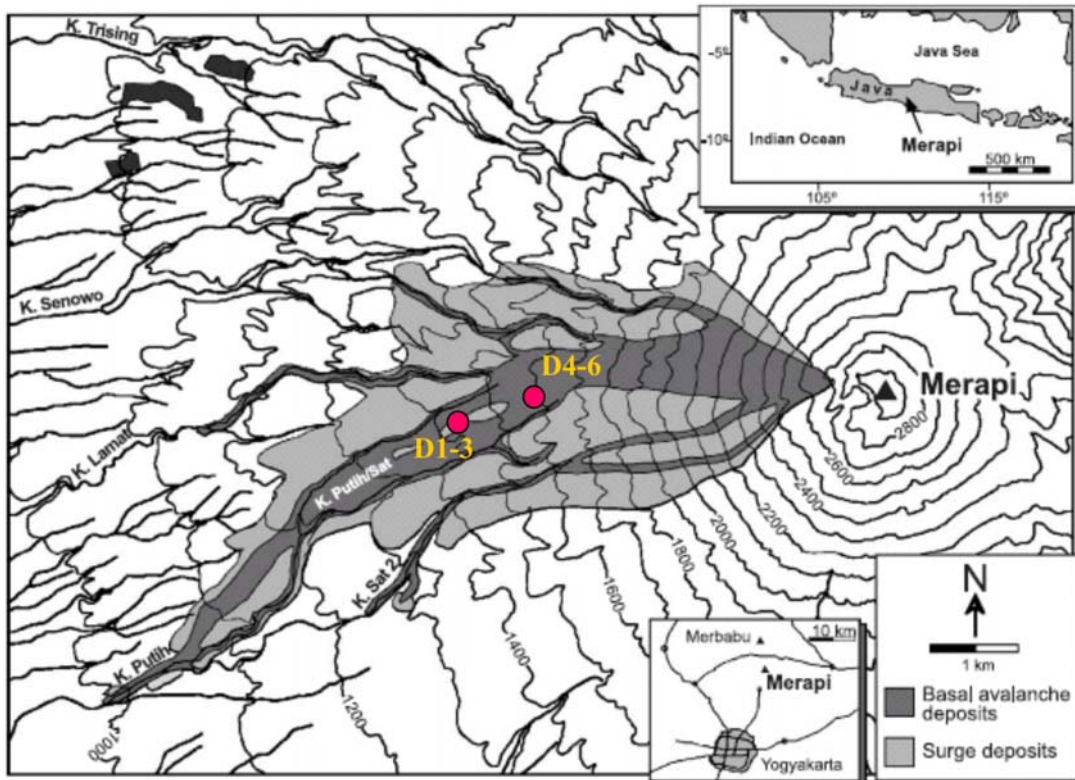


Figure 3.13: The two locations of the six measuring points taken on Merapi volcano. D1-3 are distal deposits of a 1998 Jurangjero valley block-and-ash-flow, D4-6 were taken on a site closer to the dome. On each location 60 samples from a lower, middle and upper section of the flow have been measured, respectively. Modified from *Schwarzkopf et al.* 2005.

The results of the measurements show vaguely bimodal distributions for D1-D4. This bimodality is also evident for the total data compilation, indicating at least two bubble growth stages in the Merapi andesite (Figure 3.14). The mean porosity of the entire dataset is 26.21 vol%, its mean density 2.08 g/cm^3 . The mean porosity variation within a respective deposit location, from upper (U) to lower (L) level is displayed in Figure 3.14 (h). It shows trends in the opposite direction for the distal (decreasing with depth) and proximal sites (increasing with depth). The compiled mean porosity values

(in vol%) (Figure 3.14 (i)) indicate no apparent change in sample density with distance from the dome. The lack of a systematic correlation between porosity distribution and (a) runout distance and (b) stratigraphic position is consistent with the chaotic, unsorted character of Merapi-type block-and-ash-flows.

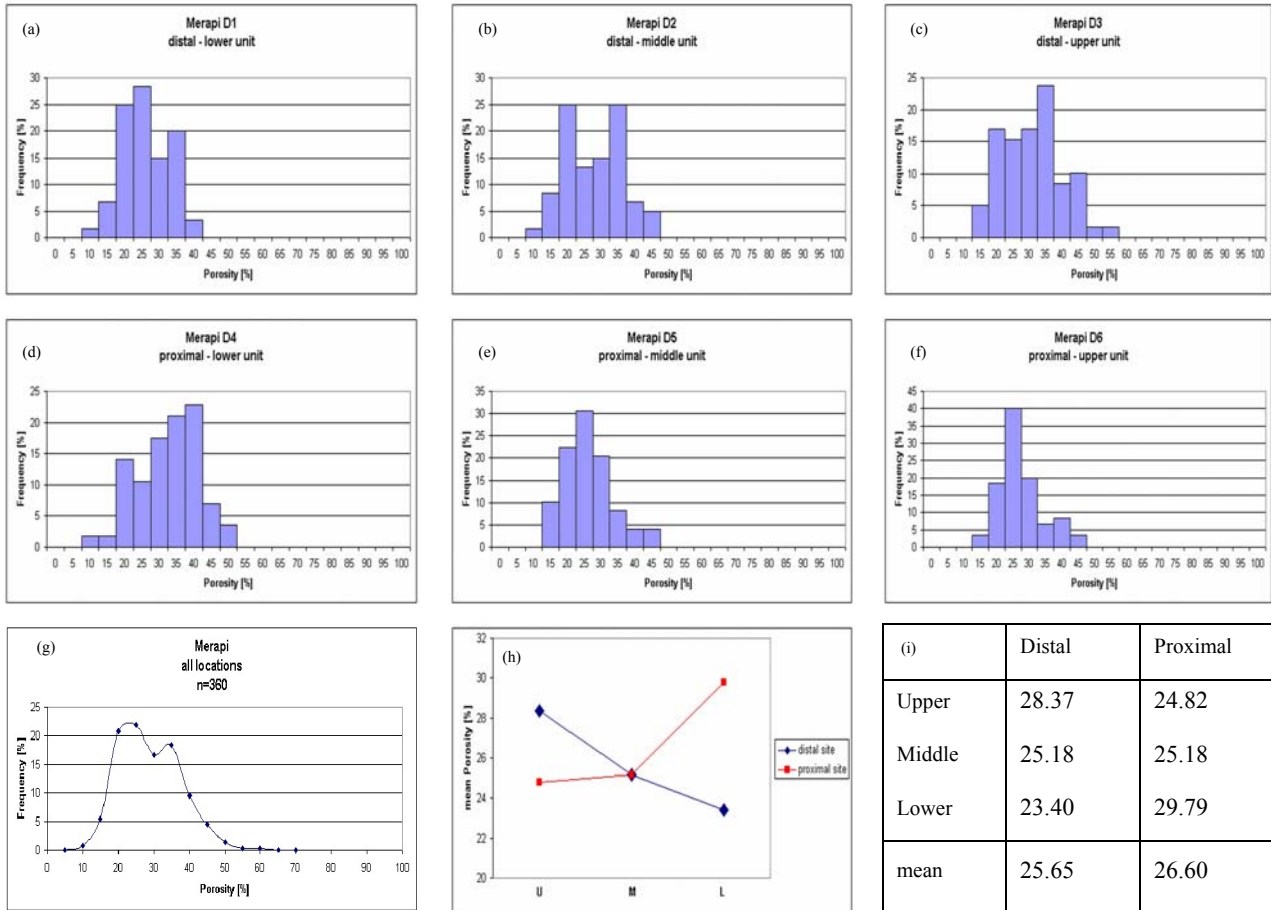


Figure 3.14: Porosity distributions of three distal (D1-3) and 3 proximal (D4-6) measuring points from Merapi’s western flank. The compiled distribution (g) shows a slight bimodal character with a peak at ~20 vol% porosity. (h) displays the mean porosity variation within a respective deposit location, from upper (U) to lower (L) level. The compiled mean porosity values (in vol%) (i) indicate only narrow differences between the distal and proximal sites.

3.3.7 Unzen

Unzen volcano has been extensively sampled in two field campaigns 2000 and 2001. More than 1000 density data have been obtained from 37 locations (Figure 3.15) and been published and interpreted in *Kueppers et al.* 2005 and *Kueppers* 2005. The deposits of the 1990 -95 eruption from four valleys and the dome have been analysed.

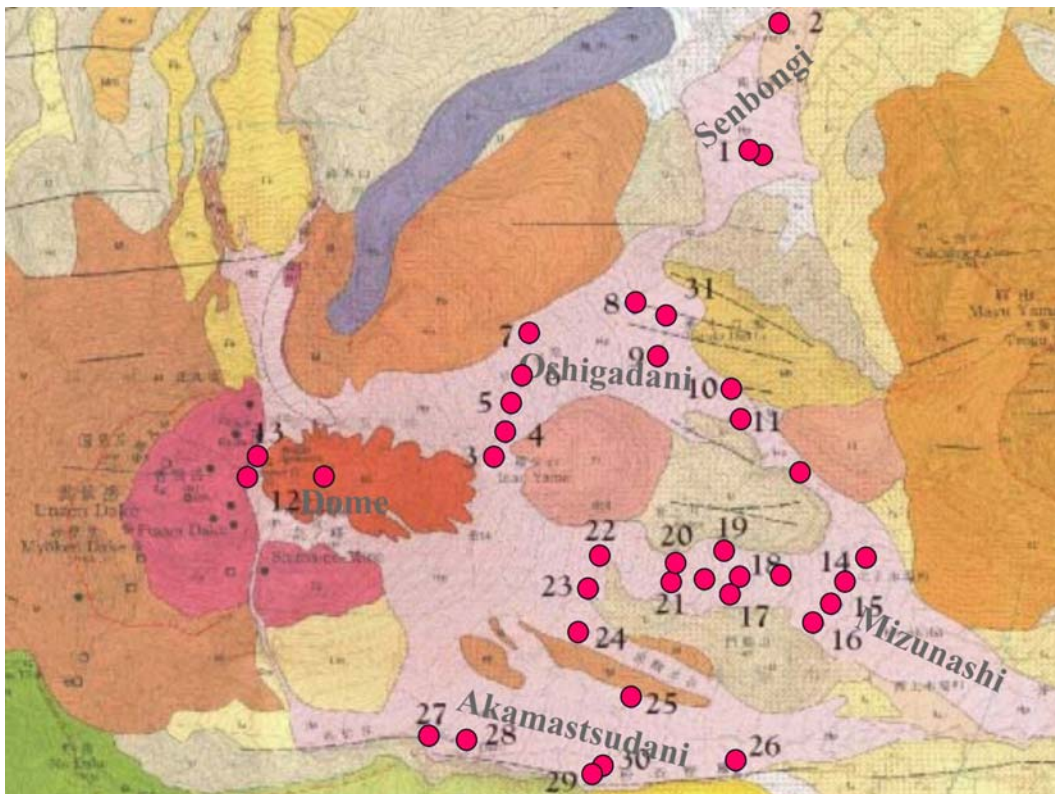


Figure 3.15: Locations of the 37 measuring points on Unzen volcano investigated by U. Kueppers and B. Scheu in two field campaigns in 2000 and 2001 (Modified from *Kueppers* 2005, geological map from *Watanabe & Hoshizumi* 1995).

For this work, the block-and-ash-flow density results have been recalculated to porosity values using a mean matrix density of 2.60 g/cm^3 . The results show peak porosities around 25 vol%, except the somewhat denser dome samples ($\sim 20 \text{ vol\%}$). The mean porosity of all samples is 23.2 vol%; a slight bimodality can be detected especially at the entire dataset (Figure 3.16). As mean density 1.93 g/cm^3 has been determined.

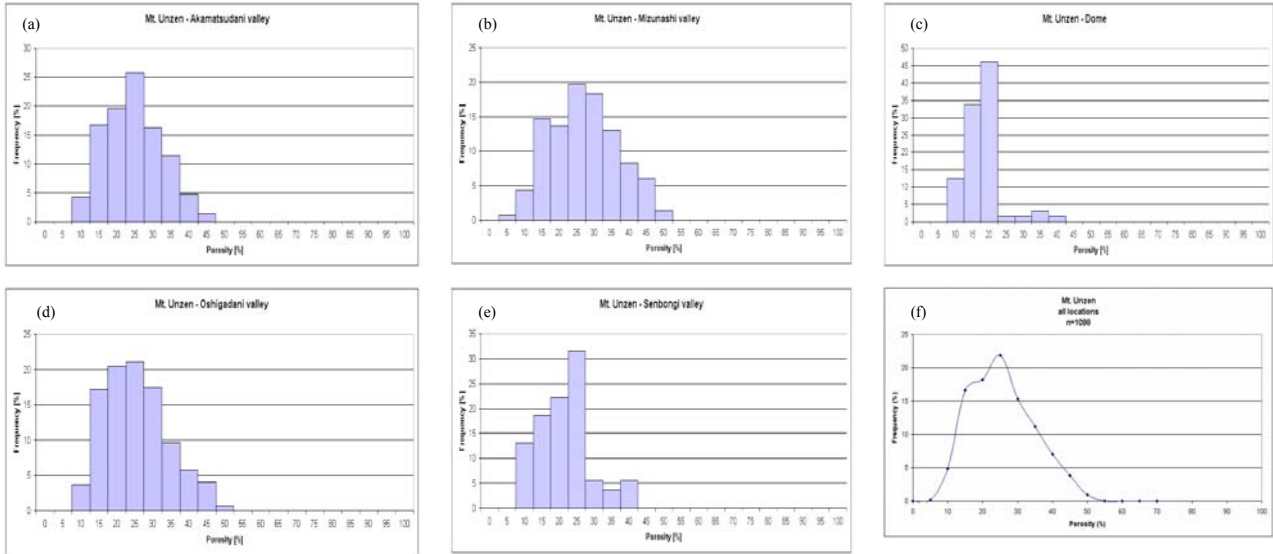


Figure 3.16: Porosity distributions of Unzen volcano. The result of four valleys and the dome region have been compiled. The total number of measurements is 1098. The diagram of the entire dataset delivers a mean porosity of 23.2 vol%.

3.4 Interpretations

3.4.1 Correlations between porosity distributions and eruptive behaviour

In order to compare the porosity distributions of the seven volcanoes described above and to relate distinct distribution patterns to specific volcanic environments and eruptive styles, the porosity-frequency plots of the primary deposit datasets (i.e. without lahar deposits) of these volcanoes have been compiled in Figure 3.17. Additionally, the Mt. St. Helens data from *Hoblitt & Harmon (1993)* are plotted for comparison. To convert their density dataset to porosity values, a mean matrix density of 2.69 g/cm^3 has been used. The diagram 3.17 illustrates the tremendous bandwidth of the physical state of the investigated volcanic material: with samples from <1 vol% to 95 vol%, the entire range of possible porosities has been covered by the field studies. Interpretable parameters of this data compilation comprise:

- the range of porosity covered by the deposits of a volcano,
- the shape of the distribution (unimodal, bimodal, Gaussian etc.),
- the relative and absolute position of the porosity peak and mean porosity value, respectively.

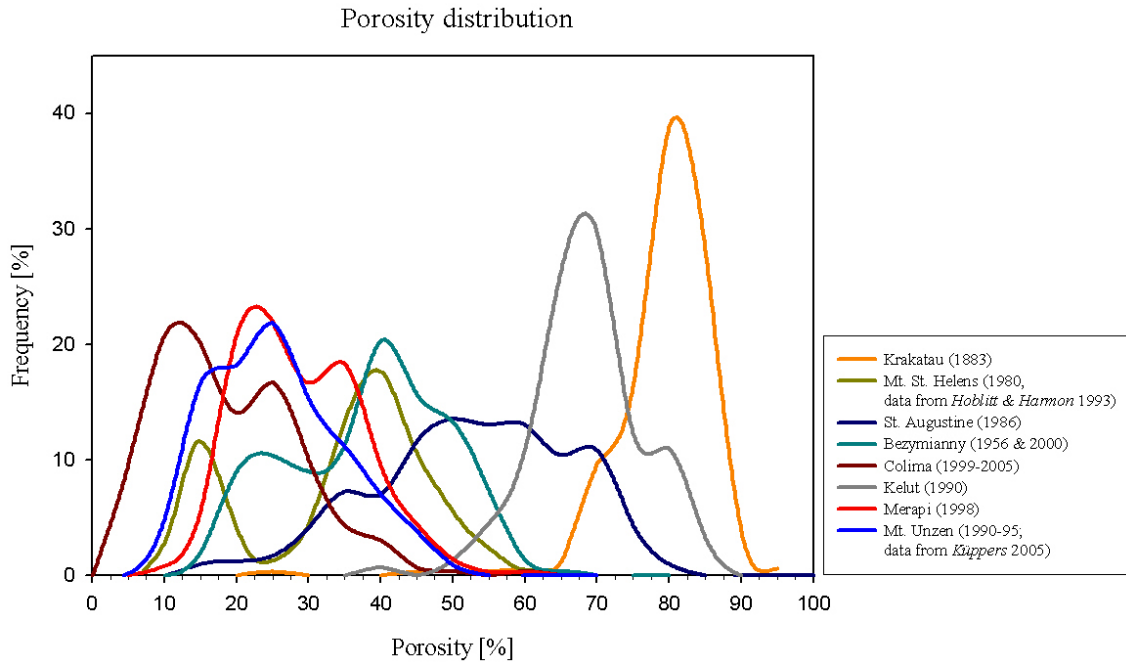


Figure 3.17: Compilation of the porosity distribution datasets of primary deposits of all eight investigated volcanoes.

The “broadness” (variance) of a volcano’s porosity distribution curve reflects its variability in (a) primary volatile content of the magma, and (b) the effectiveness of degassing processes prior to eruption (this effectiveness actually depends on the magma permeability and the time available for gas loss - which, in turn, depends the magma viscosity and the duration of magma ascent). In addition, post- or syneruptive sorting processes may affect the porosity/ density distribution. A distal fallout deposit for example exhibits *per se* a much smaller variability in clast sizes and densities than a block-and-ash-flow or gravity-induced debris flow. Many deposits, especially when they are older in age, may have been reworked which would present an altered porosity distribution.

The shape of the distribution reflects most likely the number of nucleation events the magma has been exposed to during ascent. Usually these different events correspond to differences in the physical conditions of the magma (pressure, temperature, chemical gradients; see Chapter 1.2). Rapid changes of external conditions (e.g. decompression during an explosive eruption) strongly affect bubble growth kinetics and may allow, for example, the sudden nucleation of a new population of vesicles. If this new population is restricted to a specific type of magma in terms of chemical composition or level in

magma column, different peaks in the porosity distribution of an eruptions deposit will be the result.

The position of porosity peak(s) can be seen as a representative measure for a combination of (a) the initial gas content of the magma, and (b) the (dis)ability of the magma to degas to the atmosphere or the country rock, i.e. its permeability. Magma with high volatile content and low permeability retain a comparatively big amount of potential energy in the form of overpressurized gas, thus its eruption may be assumed to be highly explosive.

Taking the criteria mentioned above into account, the porosity distributions of the eight investigated volcanoes can be interpreted and generally classified according to their eruptive styles. In this way, the volcanoes can be subdivided into three groups:

- (a) dome forming eruptions with occasional explosions but predominantly gravitational-driven block-and-ash-flow/ debris flow activity (VEI 1-3)
- (b) cryptodome formation preceding a sector-collapse-induced lateral blast (VEI 5)
- (c) explosive eruptions with subplinian to plinian phases (VEI 4-6)

Colima, Merapi and Unzen represent the first group of dome building volcanoes. Their porosity distributions show mean values clearly below 30 vol% (16.4-26.2) and a slight bimodality (Figure 3.18a). Bezymianny 1956 and Mount St. Helens 1980 eruptions are two examples of lateral blast eruptions with preceding cryptodome growth. In both cases, the porosity of the resulting pyroclasts shows a distinct bimodal distribution, with the higher peak at ~40 vol%. The mean porosity values vary around 30 vol% (28.2 and 32.4, respectively) (Figure 3.18b). Krakatau 1883, Kelut 1990 and Augustine 1986 serve in this work as examples of highly explosive eruptions with subplinian to plinian activity. Due to its change in eruptive style during the 1986 activity period, Augustine volcano may here be seen as a link between the less explosive dome growth group and the high explosive activity group with pyroclastic flows and pumice ejection. The dataset including all seven primary deposit locations (i.e. without the lahar deposit) accordingly delivers a rather broad and flat porosity distribution (Figure 3.18c). If, however, only the products of the explosive phase (i.e. the pumice flows and pumiceous pyroclastic flows) are taken into account (Figure 3.18d), the resulting curve shows a slightly bimodal distribution (likely reflecting the mixture of pyroclastic flow and fallout deposits) with a mean porosity at 61.4 vol%, and is therefore in better accordance with evenly explosive Kelut volcano (both VEI 4).

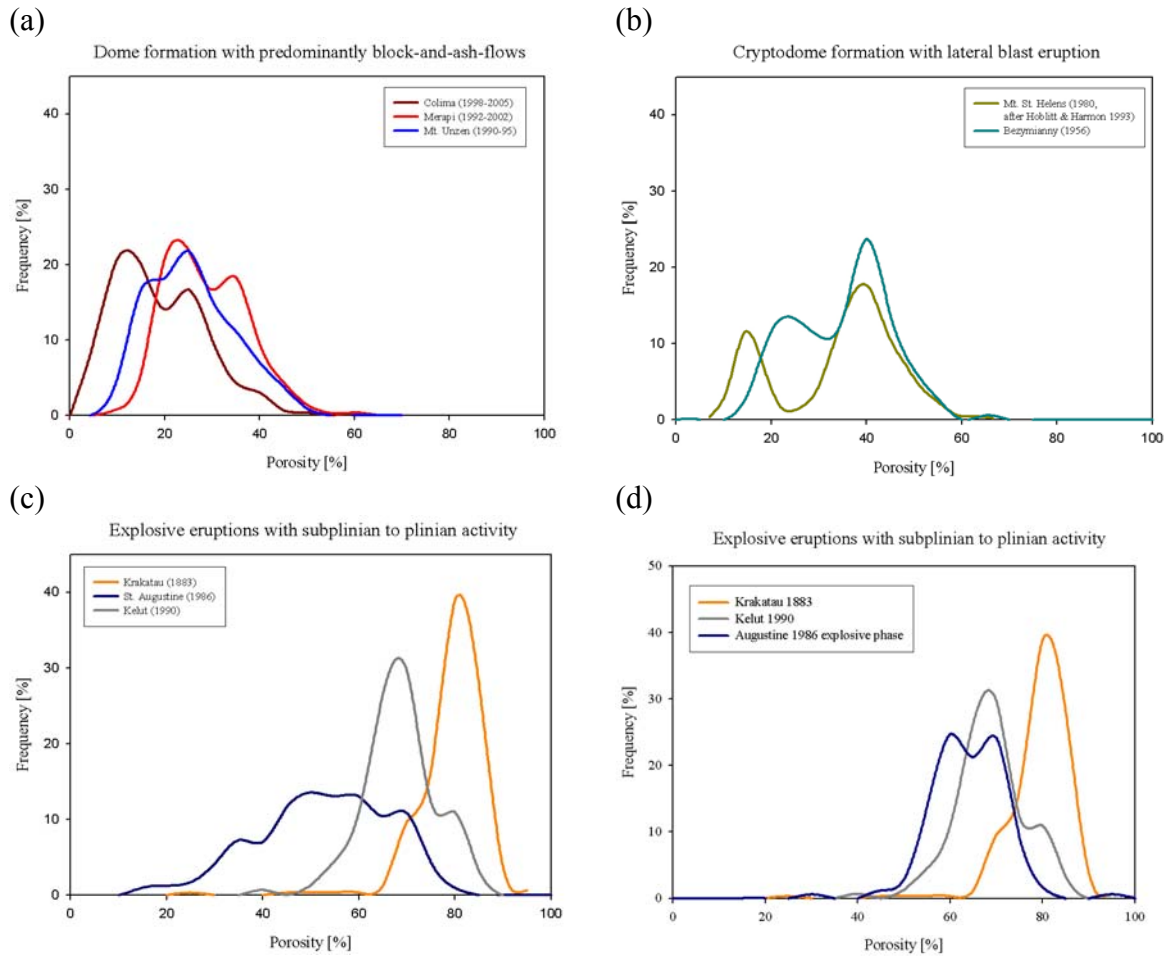


Figure 3.18: The porosity distributions of the eight investigated volcanoes can be interpreted and generally classified according to their eruptive styles: Dome forming eruptions with occasional explosions but predominantly gravitational-driven block-and-ash-flow/ debris flow activity (a), cryptodome formation preceding a sector-collapse-induced lateral blast (b), and explosive subplinian to plinian eruption (c). The broad distribution of Augustine in (c) becomes better defined with a smaller variance, if only the pumiceous pyroclastic deposits are taken into account (d).

3.4.2 Correlations between porosity and the size of volcanic eruptions

Volcanic Explosivity Index

The Volcanic Explosivity Index (or VEI) was introduced by *Newhall & Self* (1982) as a measure for the size of a volcanic eruption. It is a semi-quantitative logarithmic scale and is based on a combination of erupted tephra volume, eruption plume height and a subjective description of observers. The VEI ranges from 0 (“non-explosive”) to 8 (“colossal”). A VEI 6 eruption, for example, corresponds to an erupted

tephra volume of 10-100 km³ (*Newhall & Self* 1982, *Simkin & Siebert* 2002-, *Mason et al.* 2004)

As mentioned above, the averaged pore volume of a volcanic deposit should allow inferences on the explosive potential of an eruption. Although the VEI scale is a very general classification of the explosive style of an eruption and mostly integrates over longer periods of activity, it may in this context serve as a reference measure. In Figure 3.19 the mean porosity values of eight distinct eruptions or, in the case of Augustine, eruptive phases are plotted versus their VEI classification after *Simkin & Siebert* (2002-). The distribution indicates a rough general positive relation of the mean porosity with the VEI value. Exceptions can be noted especially at the low-porosity deposits of Colima, Unzen and Merapi. These show no coherency within this correlation. The deviation of the two cryptodome-dominated eruptions of Bezymianny and Mount St. Helens towards higher VEI scales is however not surprising, and reflects a different style of depressurization: During the formation of a cryptodome, volatile exsolution and thus porosity development is suppressed by the lithostatic pressure of the overlying material. Nevertheless, the exsolved gas in the (limited) pore volume should be able to bear a higher amount of overpressure than in an environment without the additional lithostatic load. Upon rapid decompression, a highly compressed gas in a comparably small total pore volume may therefore cause a large, cataclysmic explosive response to the removal of the confining load. This scenario lead to the VEI 5 eruptions of Mt. St. Helens and Bezymianny which generated material with no more than ~30 vol% porosity.

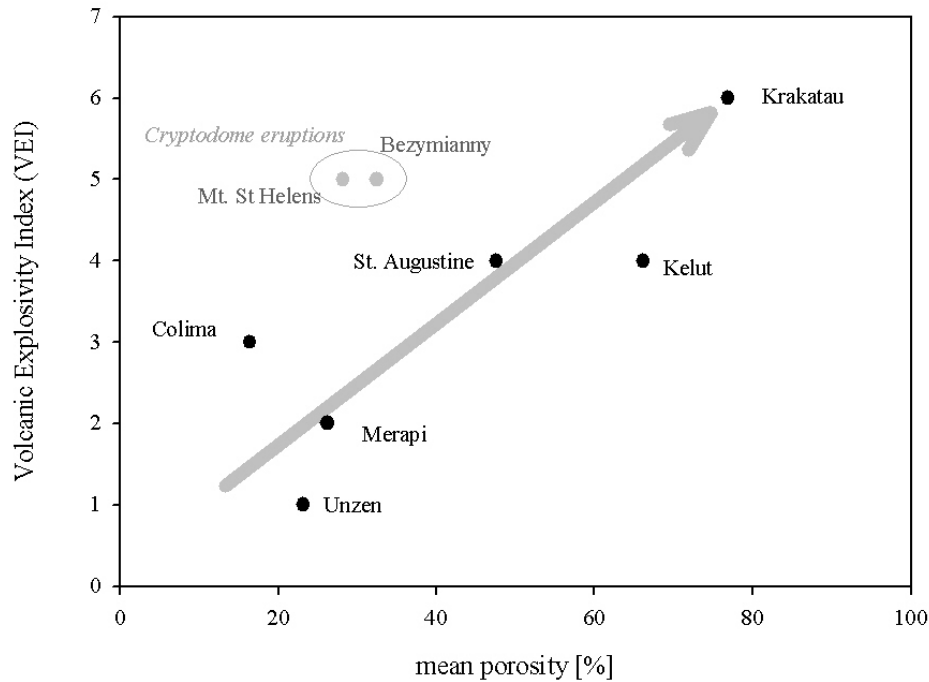


Figure 3.19: Mean porosities plotted versus the Volcanic Explosivity Index (VEI) defined by *Newhall & Self* (1982). If the cryptodome eruptions of Bezymianny and Mt. St. Helens are treated separately, a rough general positive trend can be observed.

Eruption Magnitude

A significant problem with the use of the VEI scale is that it is mainly based on an estimated tephra bulk volume of the respective eruption and does not account for the deposit density. As the density of tephra deposits may vary considerably (e.g. a layer of inflated pumice versus a densely welded ignimbrite), two eruptions with the same volume of erupted rhyolitic magma may produce extremely different bulk tephra deposits and thus different VEI measures. Additionally, the consideration of only the amount of erupted material provides only limited information on the intensity of an eruption, since it does not account for the time span involved, (*Mason et al.* 2004). A solution to this dilemma has been proposed by *Pyle* (1995, 2000). He suggests a combination of two parameters to better describe the characteristics of an eruption: the eruption magnitude M and the eruption intensity I . The logarithmic M is entirely based on the mass of erupted material (in kg):

$$M = \log_{10}(\text{mass}) - 7, \quad (3.2)$$

Similarly, the intensity scale depends on the mass eruption rate in kg/s:

$$I = \log_{10}(\text{mass eruption rate}) + 3 \quad (3.3)$$

The mass eruption rate is commonly estimated according to direct observations, so data are not available for every eruption. The scales of both parameters are chosen in a way to be comparable to the VEI scale.

Using the mean bulk density values determined in the field campaigns, it is possible to calculate M from the easier obtainable bulk tephra volumes of an eruption, listed e.g. in digital databases like *Siebert & Simkin 2002*- (Table 3.1).

Table 3.1: Compilation of Tephra volume, measured mean density, calculated erupted mass and the explosivity scales M and VEI.

Eruption	Tephra volume (m ³) ^b	Mean density (kg/m ³)	Erupted mass (kg)	Magnitude M	VEI ^b
Colima 1998-rec	2,40E+06	2280	5,47E+09	2,74	3
Krakatau 1883	2,00E+10	570	1,14E+13	6,06	6
Augustine 1986	1,00E+08	1440	1,44E+11	4,16	4
Unzen 1990-95	4,70E+06	2000	9,40E+09	2,97	1
Kelut 1990	1,30E+08	730	9,49E+10	3,98	4
Merapi 1992-2002	1,10E+07	2080	2,29E+10	3,36	2
Bezymianny 1956	2,80E+09	1800	5,04E+12	5,70	5
Mt. St. Helens 1980	1,20E+09	1930 ^a	2,32E+12	5,36	5

a - mean density value calculated from density data from *Hoblitt & Harmon (1993)*; b – data from *Siebert & Simkin 2002*-

As M accounts for both the tephra volume and mean density, a closer correlation between porosity and eruption magnitude can be expected and becomes verified in Figure 3.20. Now also the low porous eruption deposits fit very well into the trend. This correlation seems to react even more sensible to changes of the eruption mechanism, as the deviation of Bezymianny, Mount St. Helens and also Kelut is bigger in Figure 1.20 compared to Figure 1.19. All these eruptions are characterized by not only pure explosive (Vulcanian or Plinian) eruption mechanism. Because of the assumed high energetic character of the lateral blast eruptions, the data points of Bezymianny and Mount St. Helens still deviate from a possible linear relation. Also the Kelut 1990 eruption does not closely fit this approximate trend, most likely because it was comparatively short (and had therefore a relatively low total tephra output), but -due to its phreatomagmatic character- intense.

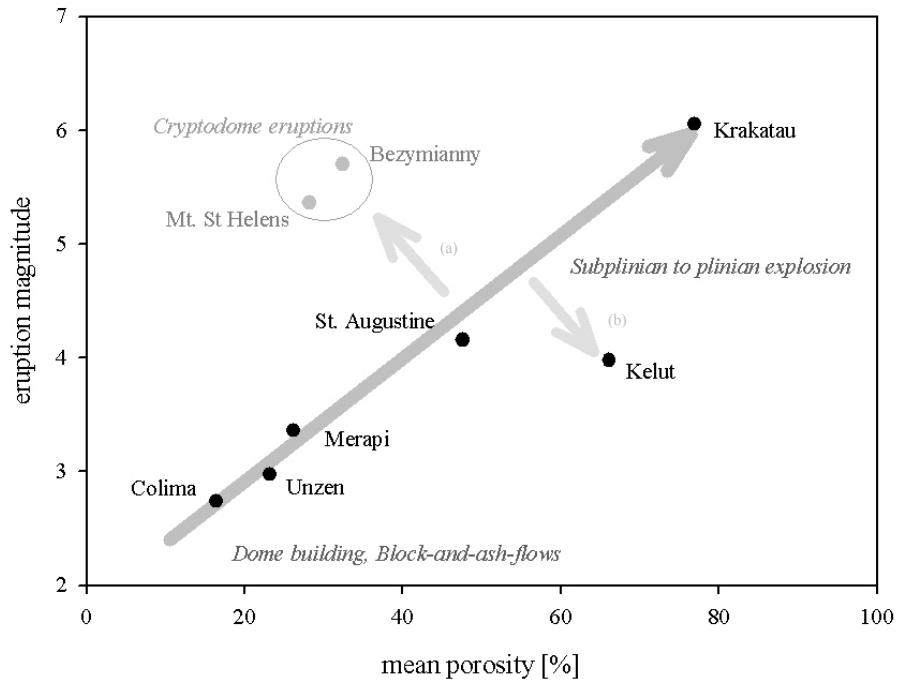


Figure 3.20: Relationship between the mean porosity of an eruption and the eruption magnitude as defined by Pyle (1995, 2000). A general positive trends with deviation can be observed (a) towards low porosity/ high magnitude, possibly due to hindered bubble growth e.g. in cryptodomes, and (b) towards high porosity/ low magnitude, possibly due to a short eruption duration and subsequent comparatively low total magma output, but high, phreatomagmatic explosivity.

4 Permeability measurements on volcanic rocks – influences of texture and temperature

4.1 Factors controlling permeability

4.1.1 Basic parameters

Permeability is defined as the ability of a porous medium to allow fluid flow through its pore space in response to an applied pressure gradient. It is commonly described by Darcy's Law that relates the pressure gradient over a sample and its dimensions to the flow rate of a fluid through the sample in a linear relationship:

$$Q = k \frac{A}{L} \Delta p \quad (4.1)$$

Here, Q is the flow rate, A is the samples cross-sectional area, L its length and Δp the pressure gradient. The permeability coefficient k defines the slope of the linearity; its SI-unit is m^2 . In the present form, equation (4.1) bears a limited validity, since (a) it only accounts for incompressible fluids (i.e. liquids), (b) it is normalized for the viscosity of water (the primary derivation of Darcy's equation was based on hydrological investigations of groundwater flow; *Darcy* 1856) and (c) it assumes laminar flow conditions. Accordingly, when regarding flow processes of a gaseous phase at high flow rates, additional permeability-controlling factors have to be taken into account: The viscosity of the gas phase μ_g , and a non-linear term, basically depending on the Reynolds number and the flow velocity, to correct for the turbulent flow conditions (see Chapter 4.2.2, equations. (4.5) and (4.6)).

4.1.2 Textural parameters

It seems obvious that the filtration of a fluid through a porous medium strongly depends on the actual volume fraction of pore space. Indeed, it can be shown either theoretically (e.g. *Rose* 1945a-c, *Kozeny* 1927, *Carman* 1956, *Dullien* 1979, *Katz & Thompson* 1986, *Johnson et al.* 1986) or empirically (e.g. *Eichelberger et al.* 1986; *Klug*

& Cashman 1996; Saar & Manga 1999; Blower 2001a) that porosity and permeability are linked by a complex positive relationship. This is not surprising, as a higher proportion of pore volume is generally expected to lead to a greater probability of pore connectivity and the formation of a fluid-flow providing pathway. However, as will be shown below, the relationship between k and Φ is not a unique one, because many other textural parameters may play an important role concerning gas flow properties. Among these parameters are (a) the connection geometry (i.e. intergranular pore spaces in clastic sediments vs. bubble interconnections), (b) the pore sizes, (c) pore shape and (d) pore size distribution (Figure 4.1).

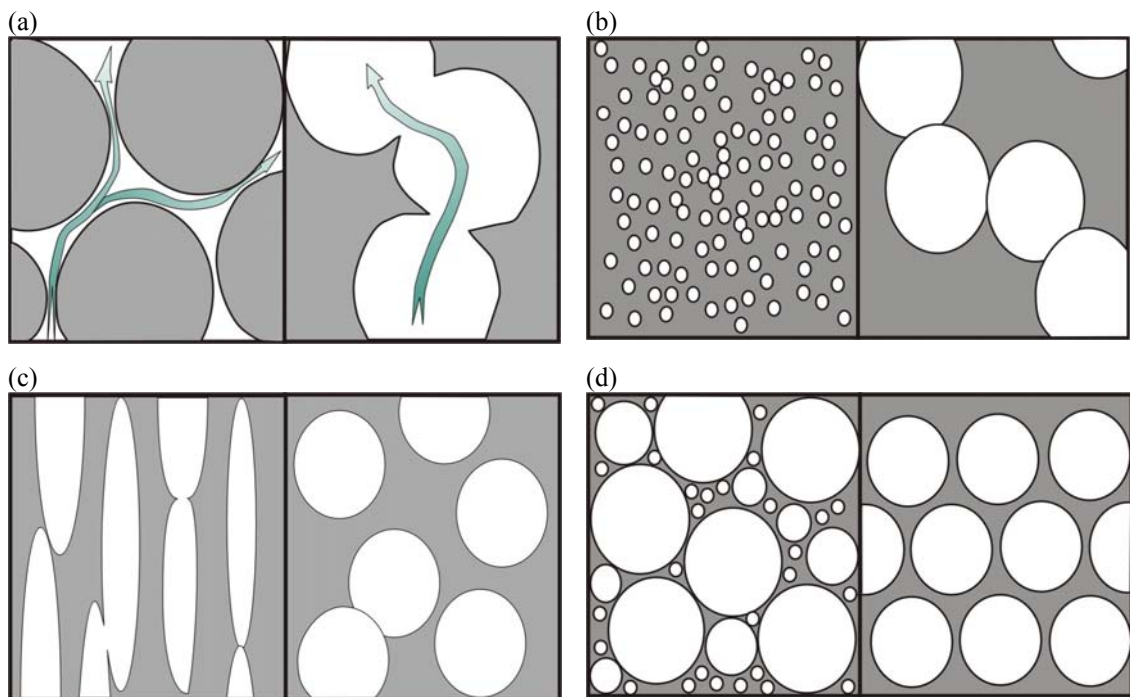


Figure 4.1 Textural parameters that may influence the permeability of a porous medium: a) pore interconnection geometry; in clastic sediments (e.g. sandstones) fluid flow is possible through the spaces between the grain components (“concave” porosity), whereas in volcanic rocks filtration occurs through bubble-bubble interconnections (“convex” porosity). b) Pore size; although the resulting total porosities might be identical, larger pore sizes lead to (1) wider pore interconnection aperture sizes and thus a lower resistance to fluid flow (Blower 2001a) and (2) to a higher probability of pore connectivity (Navon & Lyakhovskiy 1998). c) Pore shape; elongated pores with higher aspect ratio (length/width) cause a permeability anisotropy: permeability is increased along the axis of elongation and decreased perpendicular to this direction, with no change in the actual value of total porosity (Blower 2001a). d) Pores size distribution; a polydisperse bubble distributions allow much higher total porosities without necessarily leading to interconnected pores. Permeability can thus be very low at high pore volume fractions (Blower 2001a).

Models that mathematically relate permeability to porosity and pore geometries have been suggested by *Rose (1945a-c)*, *Kozeny (1927)*, *Carman (1956)*, *Dullien (1979)*, *Katz and Thompson (1986)*, *Johnson et al. (1986)*, and *Blower (2001b)*, for example. Most of them recommend a power-law relationship between k and Φ . A comprehensive compilation of permeability-porosity theories is given in *Saar (1998)*. Two of these models, which will be referred to further in this work, are described in more detail below.

The empirical Kozeny-Carman equations are based on capillary tube models and relate permeability to the porosity of a porous medium in cubic proportionality, thereby including quantities such as surface density, tortuosity, and pore shape (e.g. *Carman 1956*; *Schopper 1982*). According to *Doyen (1988)* and *Klug & Cashman (1996)*, these equations can often be simplified to power-law relations with exponents n of 3.0 – 3.8 and a constant of proportionality c (Figure 4.2):

$$k(\Phi) = c \cdot \Phi^n ; \quad 3.0 \leq n \leq 3.8. \quad (4.2)$$

Similarly other models describing gas-flow through fractures predict a cubic relationship between gas flow rate and crack aperture (and thus crack volume) under laminar flow conditions (“cubic law for fracture flow”; e.g. *Lamb 1945*; *Langlois 1964*).

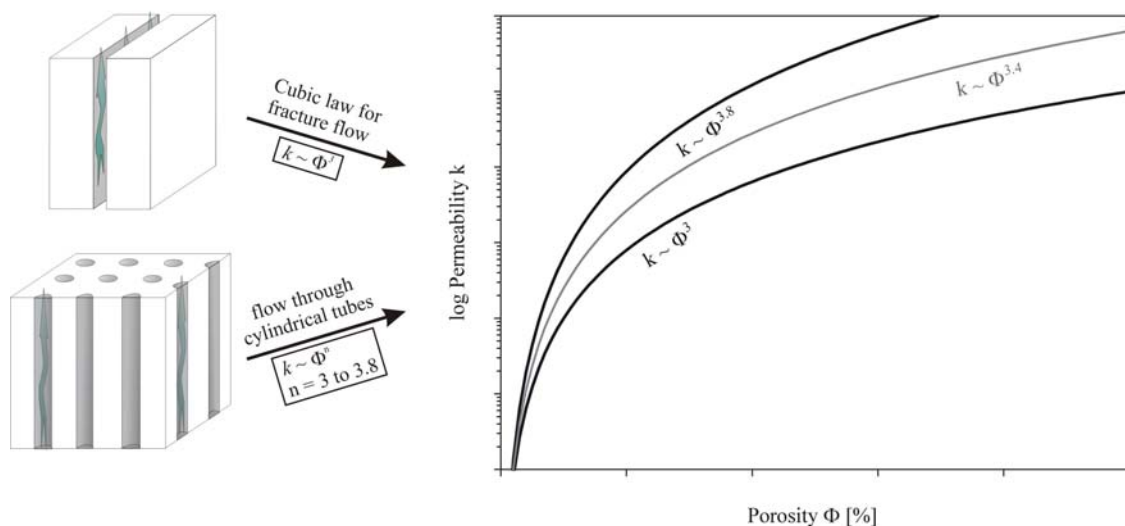


Figure 4.2: Schematic depiction of the theoretical predicted permeability-porosity relations according to Kozeny-Carman equations, which are based on flow behaviour through cylindrical tubes, and fracture flow models. Both recommend power-law relations with exponents ranging from 3 to 3.8.

Percolation theory deals with fluid flow through a random media by mathematically describing the probability of connectivity in a disordered lattice and generally predicts a permeability-porosity relationship in the form

$$\begin{aligned} k(\Phi) &= c \cdot (\Phi - \Phi_{cr})^n & \forall \Phi \geq \Phi_{cr} \\ k(\Phi) &= 0 & \forall \Phi < \Phi_{cr} \end{aligned} \quad (4.3)$$

where c is a magnitude-defining constant and n is the power-law exponent dependent on the pathway geometry. Φ_{cr} is a critical porosity (“percolation threshold”) below which no connected, continuous network of pores and thus no permeability can be expected. For media with idealized, spherical bubbles (FPS – fully penetrable sphere model), $n = 2$ and $\Phi_{cr} \sim 30\%$ (Figure 4.3; Saar & Manga 1999; Blower 2001a; Feng *et al.* 1987; Sahimi 1994, 1995; Mukhopadhyay & Sahimi 1994).

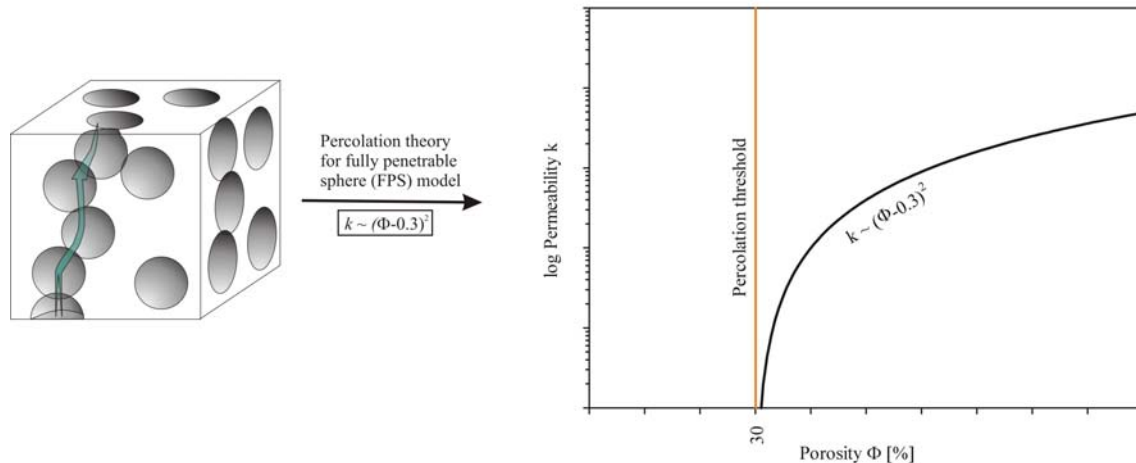


Figure 4.3: Schematic depiction of the theoretical permeability-porosity trend according to the percolation theory for a medium with fully penetrable, spherical bubbles. The model predicts a percolation threshold at $\sim 30\%$ porosity, below which no filtration can be expected, and an increase of k to the square of the porosity above that threshold.

In recent experimental volcanological research, the permeability, as a physical parameter of volcanic rocks, has increasingly become an object of interest, especially in terms of its direct influence on volcanic degassing processes and thus eruption mechanisms. Mentionable in this context are the works of Eichelberger *et al.* (1986), Westrich & Eichelberger (1994), Klug & Cashman (1996), Saar & Manga (1999), Melnik & Sparks (2002), Srouga *et al.* (2003), and Burgisser & Gardner (2005). A selected compilation of permeability measurement results of previous workers is displayed in Figure 4.4.

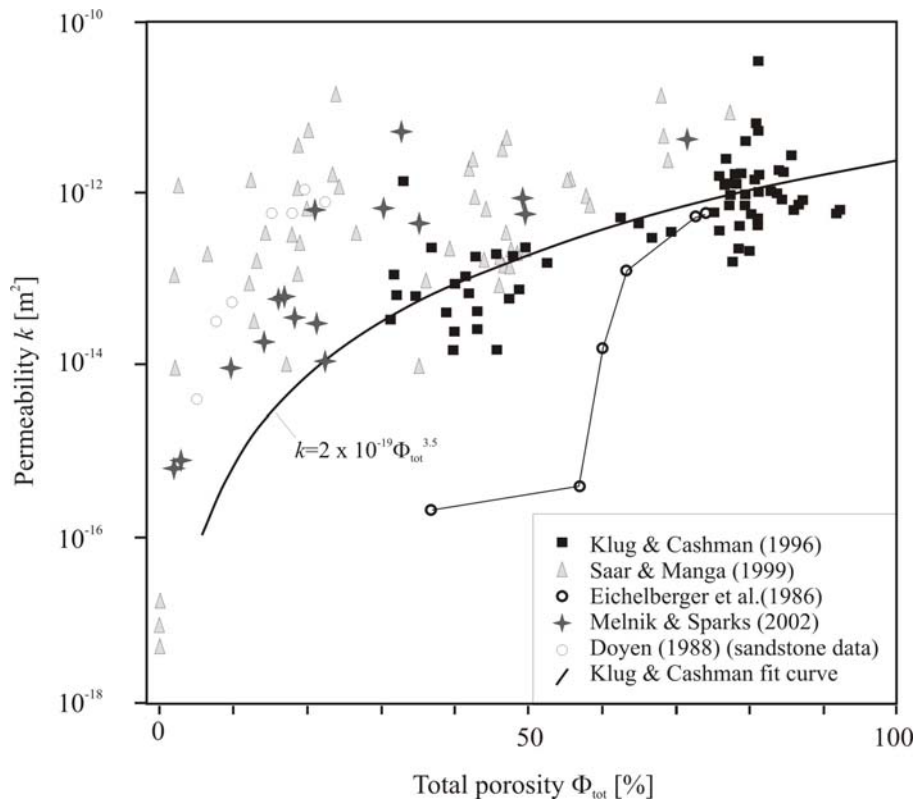


Figure 4.4: Permeability data of previous workers, plotted semi-logarithmically against the total porosity. The results show steady-state measurements on natural porous media from *Eichelberger et al.* (1986), *Klug & Cashman* (1996), *Saar & Manga* (1999), *Melnik & Sparks* (2002) and, for comparison, sandstone permeabilities from *Doyen* (1988). The trend line represents the Kozeny-Carman-based best fit curve for the data from *Klug & Cashman* ($k \propto \Phi^{3.5}$).

Regarding experimental permeability data of five previous studies, the following essential statements can be made. (1) Permeability values of vesicular igneous rocks predominantly range from 10^{-14} to 10^{-11} m². (2) Permeability generally increases with porosity. (3) Permeability data may vary by more than three orders of magnitude at a given porosity. In particular point (3) emphasizes the aforementioned extraordinary influence of rock textures and inhomogeneities on permeability. *Klug & Cashman* (1996) fit their data distribution according to a power-law trend based on Kozeny-Carman relation with an exponent of 3.5; *Saar & Manga* (1999) describe a continuous divergence of permeability results of vesicular flow-basalt from a percolation-theory-based power-law trend towards lower porosities and higher permeabilities (when normalized by a characteristic bubble area value), and interpret this displacement as a consequence of increasing bubble deformation and elongation; the steep increase in permeability values of *Eichelberger et al.* (1986) at about 60 % porosity was interpreted as the transition from a closed to an open (connected) porous system;

Melnik & Sparks (2002) approximate their data variation with the equation $\log(k(\Phi) = -10.2(100\Phi)^{0.014/\Phi}; \Phi > 0.03$.

4.2 Permeability measurements - method

4.2.1 Experimental setup

Permeability measurements were conducted on a modified setup of a shock-tube based fragmentation apparatus (*Alidibirov & Dingwell 1996a, b; Spieler 2001, Spieler et al. 2003, 2004a, b*). In order to realistically simulate strongly transient volcanic gas filtration processes, the method is based on an unsteady-state (or “pressure decay”) measuring principle (e.g. *Brace et al 1968, Innocentini et al. 2000, Liang et al. 2001*): a sudden decompression above the sample causes (a) gas filtration through the sample, if the initial pressure difference (ΔP_i) is lower than a fragmentation threshold pressure (ΔP_{fr} ; \rightarrow permeability experiment), or (b) sample fragmentation due to expansion of the gas phase in the pore space of the sample, if $\Delta P_i > \Delta P_{fr}$ (\rightarrow fragmentation experiment, Chapter 5).

The fragmentation bomb, originally designed to investigate fragmentation behaviour of volcanic rocks by rapid decompression, consists of a high-pressure autoclave, which sustains up to 100 MPa of gas pressure, and a low-pressure collecting tank representing the atmosphere (Figure 4.5). The two parts are separated by an arrangement of metal diaphragms – the decompression event is triggered by exceeding the diaphragm’s strength. For the investigation of the temperature dependency of particular rock parameters, the high-pressure autoclave can be externally heated up to 950 °C.

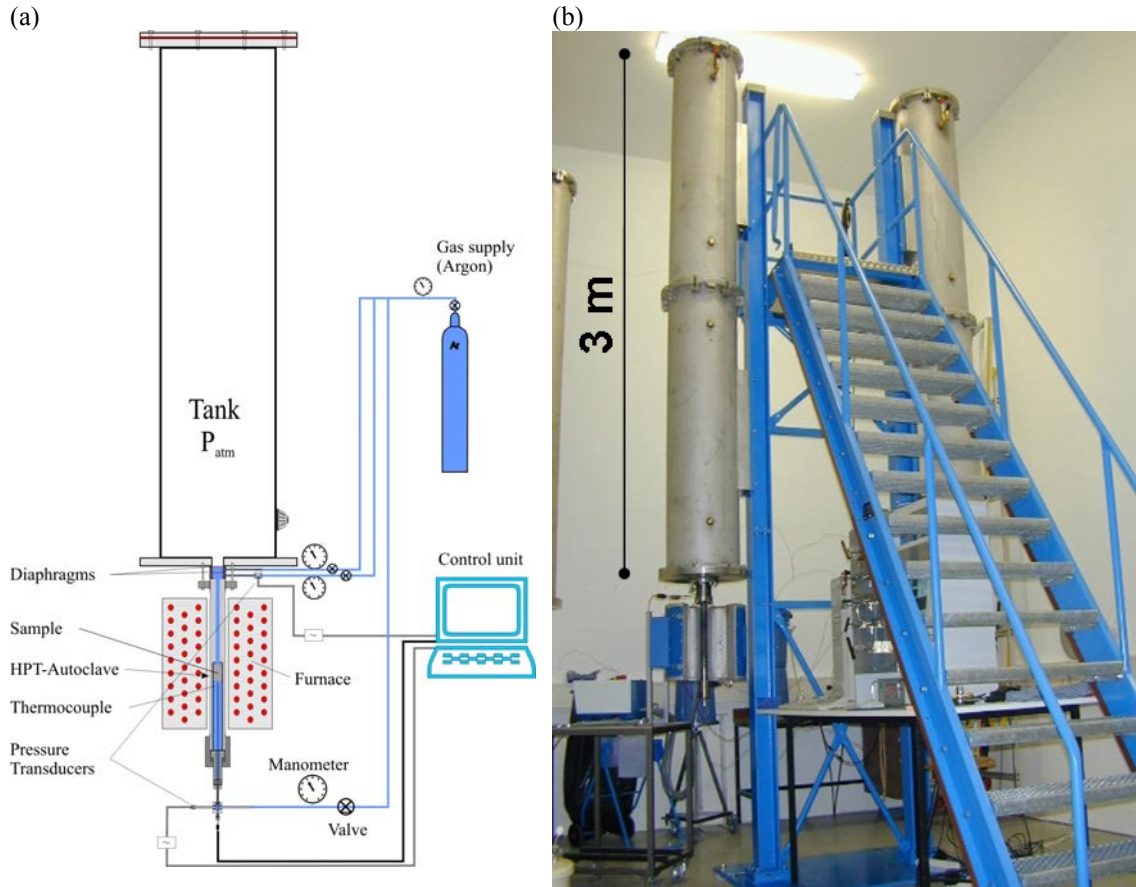


Figure 4.5: (a) Schematic view of the experimental setup for permeability measurements. A high-pressure/ high-temperature steel autoclave is attached to a particle collection tank at atmospheric conditions. The two sections are separated by a set of copper or aluminium diaphragms. Gas overpressure in the autoclave is achieved by supply of Argon gas, the pressure evolution in the autoclave is surveyed by two pressure transducers. The autoclave can be heated with an external furnace. In order to monitor the temperature within the autoclave, a thermocouple can be placed directly below the sample. (b) Photograph of the fragmentation bomb

The essential elements of the experimental setup for permeability and gas flow measurements are illustrated in Figure 4.6: **A** - To install the cylindrical rock sample into the high-pressure autoclave, it is glued gas-tight in a stainless-steel sample holder tube which is then screwed tightly on the lower sealing plug. To pressurize the autoclave argon 4.8 was used. The gas flows into the spaces below and above the sample via capillary tubes and is kept within the autoclave by the lower of two diaphragms. For further details on the multi-diaphragm trigger system see *Spieler* (2001). **B** - After the rarefaction wave, triggered by the opening of the diaphragms, hits the sample surface, the resulting pressure gradient causes the compressed argon gas to flow through the sample, until the gas pressure in the two volumes below and above the

sample is in equilibrium. The pressure trends in these spaces are recorded with two pressure transducers (*Kistler 4075A100*). A detailed description of the experimental procedure is given in Appendix A.

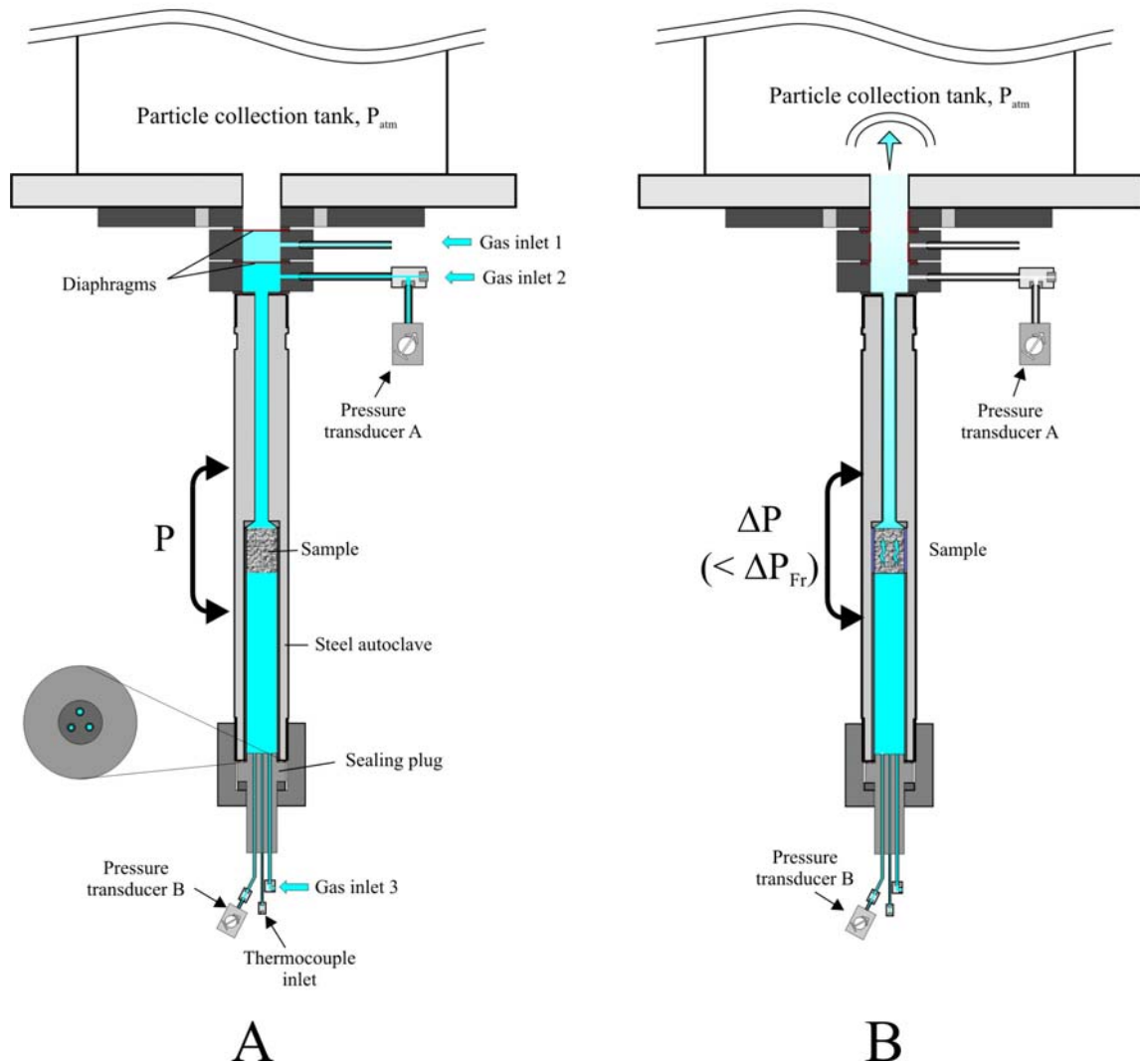


Figure 4.6: Detailed view of the autoclave setup (A) before and (B) after diaphragm rupture. ΔP_{Fr} is the threshold pressure for fragmentation. For further explanations see text.

4.2.2 Data analysis

Following the rupture of the diaphragms, the upper pressure transducer records a steep drop to atmospheric conditions, whereas the lower transducer shows an exponential decay, caused by gas filtration through the sample (Figure 4.7a). Temperature variations recorded by the thermocouple below the sample show a

decrease in temperature at the initial stage of decompression due to the gas expansion and a slight increase later due to heat transfer from the walls of the autoclave. Overall temperature variations within the autoclave are in the order of 10 - 15 °C leading to a variation in gas density of less than 5% (Figure 4.7b).

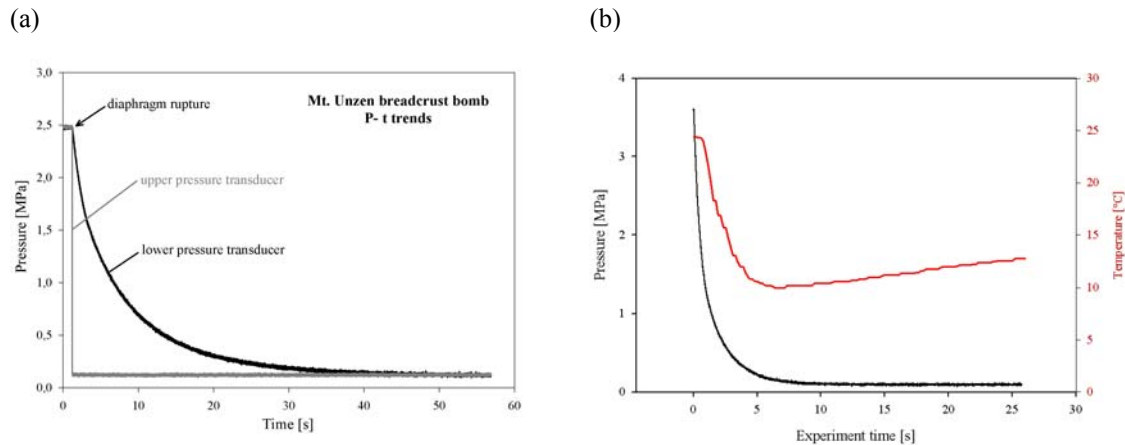


Figure 4.7: (a) Pressure drop curves recorded by the pressure transducers above and below the sample during a permeability experiments. (b) Temperature trend of the gas in the autoclave, recorded directly below the sample cylinder (red curve). For comparison the according pressure evolution in the same chamber is plotted. The temperature drop is caused by the decompression in the lower volume.

Transient filtration code

In order to analyse the experimental data a transient 1D filtration code was developed in cooperation with Dr. Oleg Melnik (Moscow State University). The flow is assumed to be isothermal due to the high heat capacity of the matrix skeleton, the intense heat transfer between the gas and the skeleton, and the low variations of the temperature in the gas volume below the sample. A non-linear friction term is taken into account to describe the rapid filtration processes. Inertia terms are neglected and, therefore, the code is not capable of considering rapid variations of parameters on the timescale of $t_a = L / a$ (where L is the characteristic length scale, for example the length of the sample, and a is the velocity of sound in the gas phase). For typical experimental conditions the value of t_a is on the order of 0.2 ms, which is much shorter than the duration of the filtration experiments (typically several tens of seconds). Therefore, the model cannot describe the propagation of a rarefaction wave through the sample generated by the disruption of diaphragms, but instead concentrates on the flow thereafter.

The basic system of equations for the code is the following:

$$\Phi \frac{\partial}{\partial t} \rho + \frac{\partial}{\partial x} \rho U = 0 \quad (4.4)$$

$$\frac{\partial}{\partial x} p = -\frac{\mu_g}{k} U + C(\text{Re}) \frac{\rho U^2}{\sqrt{k}} \quad (4.5)$$

$$C(\text{Re}) = \frac{\lambda}{\text{Re}^n}; \text{Re} = \frac{\rho U \sqrt{k}}{\mu_g}; p = \rho R T_0 \quad (4.6)$$

In this system Equation (4.4) is the mass conservation equation, Equation (4.5) is the Darcy equation with a non-linear friction term to correct for the turbulent flow conditions (Forchheimer correction) and Equation (4.6) defines parameters and the equation of state for the gas. Here ρ is the density of the gas, U is the filtration velocity, p is the pressure, μ_g is the viscosity of the gas phase, and Φ the void fraction. k is the linear permeability coefficient and $C(\text{Re})$ is the non-linear correction coefficient due to rapid gas flow, depending on the Reynolds number (Re), as a power law. λ is constant, R is the gas constant for argon and T_0 is the initial temperature of the gas. t is the experiment time, and x the position within the sample cylinder.

The system is solved with the following boundary conditions:

$$x = 0: V_a \frac{d\rho}{dt} = -\frac{\pi D^2}{4} \rho U; x = L: p = p_L(t) \quad (4.7)$$

where V_a is the volume of the autoclave below the sample and D is the diameter of the sample. At the bottom of the sample the density of inflowing gas changes due to the evacuation of the gas from the autoclave. Equation (4.7) specifies mass conservation for the gas below the sample. At the top of the sample pressure evolution with time is given. Because the code does not consider the process of diaphragm rupture, the formation of the rarefaction wave and its interaction with the sample, the function $p_L(t)$ is given by:

$$p_L(t) = p_a + (p_0 - p_a) \exp\left(-\frac{t}{\tau_0}\right) \quad (4.8)$$

where p_0 and p_a are the initial and final pressures and τ_0 is a constant defining the rate of pressure drop above the sample. The value of τ_0 influences the stability of the

calculations and is kept as small as possible (~ 0.1 s). For relatively small values of τ_0 , the particular choice has a minor impact on the results.

The code for fixed values of k , λ and n is solved numerically by means of the 2-point Thomas method described in detail in *Melnik and Sparks (2004)*. In order to find a best fit to the experimental data (the evolution of pressure in the autoclave with time) the following functional criteria is used:

$$\Delta = \min_{k,\lambda,n} \int_0^{t_f} (\ln(p_e(\tau)) - \ln(p_c(\tau)))^2 d\tau \quad (4.9)$$

Here t_f is the duration of the experimental record, and p_e and p_c are the measured and the calculated pressures at the bottom of the sample, respectively. Pressure is scaled logarithmically in order to allow both high and low pressure parts of the experimental curve to be fitted. The value of n was fixed for most calculations at $n = 0$, corresponding to the Forchheimer equation (e.g. *Dullien 1979*).

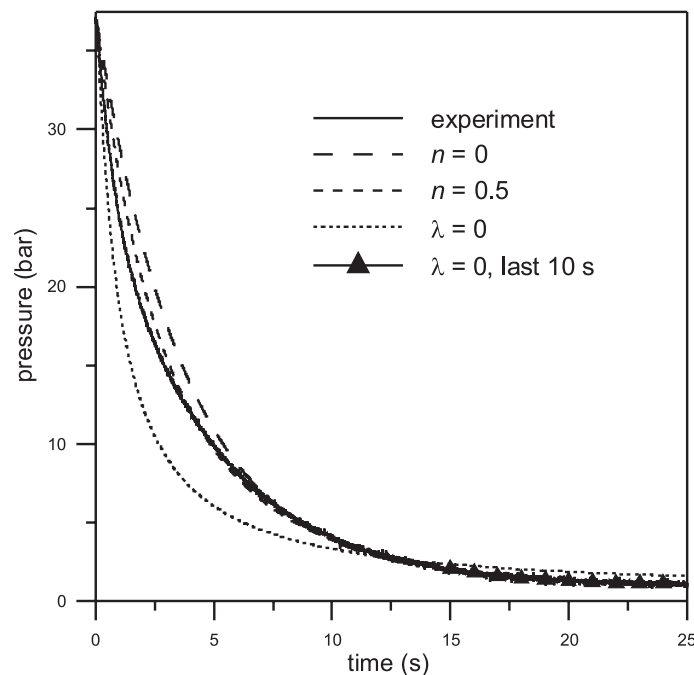


Figure 4.8: Comparison of experimentally measured evolution of autoclave pressure with calculations using different friction models. Explanations see text.

Figure 4.8 shows a comparison of the experimentally measured pressure below the sample with calculations for $n = 0$ and 0.5. Calculated best fit coefficients are for $n = 0$:

$k = 5.29 \cdot 10^{-13} \text{ m}^2$, $\lambda = 111$, $\Delta = 0.18 \cdot 10^{-2}$, and for $n = 0.5$: $k = 5 \cdot 10^{-12} \text{ m}^2$, $\lambda = 136$, $\Delta = 0.88 \cdot 10^{-3}$. For comparison the fit with $\lambda = 0$ is plotted as a dashed line. In this case $k = 1.6 \cdot 10^{-13} \text{ m}^2$. If only the last 10 s of the dataset are used for the determination of linear permeability, the value of k ($6.05 \cdot 10^{-13} \text{ m}^2$) is close to the value determined for $n = 0$. For the same sample and different initial pressures the fit for the data with $n = 0.5$ is always better, but the range of best-fit parameters for different runs is much wider than for the case when $n = 0$. Therefore, in further analysis, the Forchheimer correction to Darcy equation will be used. It is clear from Figure 4.8 that the linear Darcy law alone (i.e. for $\lambda=0$) cannot fit the experimental data well. In the case of large pressure gradients typical for pre-fragmentation conditions in ascending magma during explosive eruptions the resistance to gas escape is strongly non-linear. Therefore transient effects can be very important in this case.

Quasi-static approach

Because during most of the experiment the system behaves quasi-statically (i.e., the discharge rate above and the sample are equal) a simplified method to determine the permeability coefficient can be used. If we neglect the time derivative in Equation (4.4) then the discharge rate is a function of time only. Substituting this relationship into Equation (4.5) gives:

$$\frac{\partial}{\partial x} p(x,t) = -\frac{\mu RT_0 Q(t)}{k p(x,t)} - \frac{\lambda RT_0 Q^2(t)}{\sqrt{k} p(x,t)} \quad (4.10)$$

This equation is an ordinary differential equation for pressure where time acts as a parameter. It can be integrated analytically giving:

$$p(x,t) = \sqrt{\frac{kp^2(0,t) - 2Q(t)RT_0(\mu + Q(t)\lambda\sqrt{k})x}{k}} \quad (4.11)$$

Discharge rate can be determined from the boundary condition at the top of the sample $p(L,t) = p_a(t)$. Substitution of the discharge rate into Equation (4.11) gives pressure profile along the sample which is independent from values of k and λ :

$$p(x,t) = \sqrt{p^2(0,t) \left(1 - \frac{x}{L}\right) + p_a^2(t) \frac{x}{L}} \quad (4.12)$$

Using boundary condition at the bottom of the sample an ordinary differential equation for the evolution of pressure in the autoclave can be derived in the form:

$$\frac{dp(0,t)}{dt} = -\omega Q(p(0,t), p_a(t)); \omega = const \quad (4.13)$$

Best fit parameters calculated using Equation (13) for the same sample as in Figure 4.8 are: $4.55 \cdot 10^{-13} \text{ m}^2$, $\lambda = 128$ and $\Delta = 0.17 \cdot 10^{-2}$, corresponding to a 13% deviance to the transient code. Therefore, the quasi-static approach allows a quick and relatively accurate determination of permeability coefficients and has no stability problems.

4.2.3 Error estimation

For this new experimental setup an series of calculations errors may arise from: (1) measurement of the samples geometry and the gas volume of the autoclave, (2) technical equipment (pressure transducer, thermocouple), (3) conversion of the transducers raw data (voltage) into pressure data (Pa), (4) deviation of the numerically modelled curve from the actually measured pressure decay (Δ), and (5) factors that are not accounted in the model, including temperature variations, non 1D flow effects, and the different forms of non-linear friction laws that are possible. An estimation of the practical precision of these experiments, repeated ten times under the same external conditions, indicates a precision of 3 - 5 % for the permeability constant k . For most of the rock varieties the investigation of samples with diameters of 17 and 25 mm revealed no significant, systematic difference in the permeability values. Therefore for these samples the size of the cylinder scaling on the results is unlikely to be a major influence. Nevertheless, a potential complication may arise from the fact that in certain rock types, large, truncated pores in the drilled cylinders may distort the effective sample geometry, especially in samples with a high bubble to sample size ratio. This may result in artificially low decompression values.

4.3 Permeability measurements - results

To enable a comparability with the results of other studies, the linear permeability coefficient k will be used for further interpretations. The correlation between permeability results calculated with the 1D transient code and the total porosity of the corresponding samples is plotted semi-logarithmically in Figure 4.9. The obtained permeability values range from $2 \cdot 10^{-15}$ to $1.5 \cdot 10^{-10}$ which is in good agreement with the results of previous workers (Figure 4.4). The results show a general positive relationship between porosity and permeability with a high data scatter.

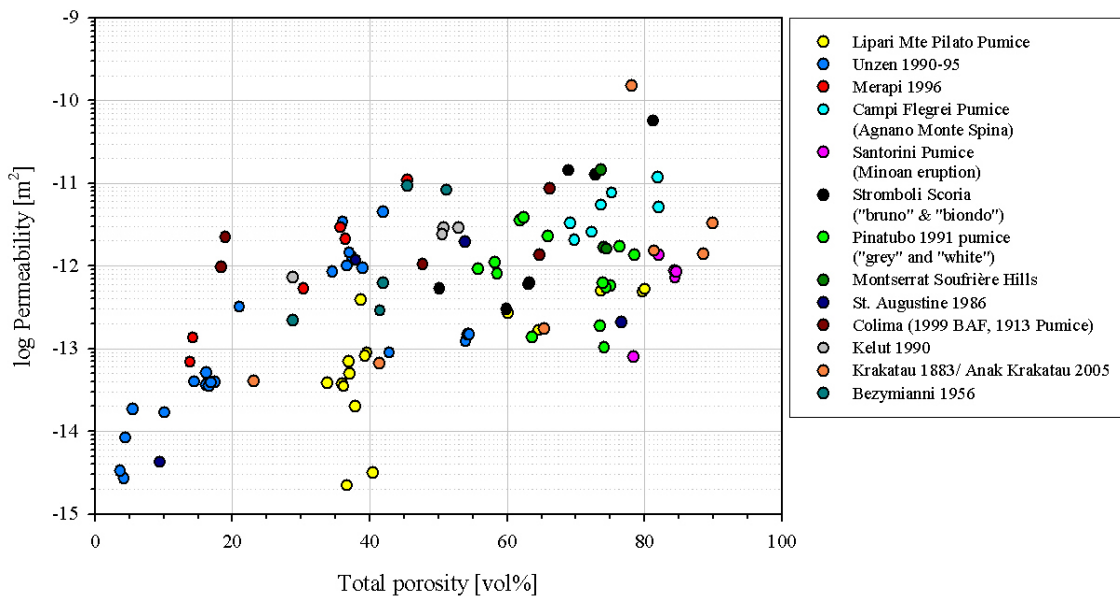


Figure 4.9: The results of unsteady-state permeability measurements on material from 13 volcanoes, shown as a total porosity vs. linear permeability plot. It reveals a general increasing trend with a high scatter.

A comparison of the permeability constants obtained using the 1D-transient code with those obtained using the quasi-static approach is shown in Figure 4.10. Values of k predicted by both methods are similar, with maximum difference of only 0.3 log units (Figure 4.10). This demonstrates that the steady-state approach provides an easy and fast method to determine permeability even from strongly unsteady experiments. However, the method is limited by the length of the dataset. If the experimental timescale is too short, transient effects may become more important.

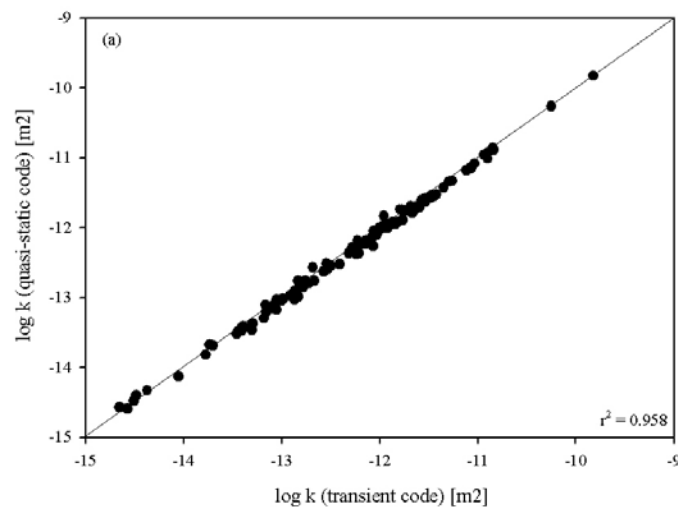


Figure 4.10: Comparison of linear permeability values obtained by transient and quasi-static approaches. A correlation coefficient of 0.958 underpins the applicability of the quasi-static approach.

4.4 Permeability-porosity relationships - interpretations

One of the most apparent features of the data distribution in Figure 4.9 is the enormous scatter of permeability of more than 3 orders of magnitude for a given porosity value. Therefore it is almost impossible to interpret these data according to a simple cause-and-effect correlation. In an attempt to apply k - Φ -models with power-law exponents of three or higher to our data, as for example the Kozeny-Carman based curve of *Klug & Cashman* (1996), the permeability values are either strongly overestimated at low porosities or underestimated for highly porous samples. Therefore it will be proposed to interpret the data using a combination of two different power-law models, each describing gas flow through a different pore structure type (Figure 4.11).

It is evident that gas flow through the samples can still occur below the theoretically predicted percolation threshold for a network of spherical bubbles ($\sim 30\%$ porosity; Figure 4.11, Figure 4.4). This flow might occur through microcracks, most likely to have been generated during cooling processes, or elongated collapsed bubbles, resulting from dynamic processes during magma flow and degassing (*Saar & Manga 1999*). If so, then adequate models to approximate this kind of degassing should be the capillary-tube based Kozeny-Carman relations or the cubic law for fracture flow, both recommending permeability-porosity relations with power-law exponents between 3.0 and 3.8 (e.g. *Doyen 1988; Klug & Cashman 1996*; see Chapter 4.1.2). Indeed we find

that the curves of Equation (4.2) corresponding to $k(\Phi) = c_1 \cdot \Phi^3$ and $k(\Phi) = c_1 \cdot \Phi^{3.8}$, with $c_1 = 1 \cdot 10^{-17}$, bound well most of the data for long-term degassed dome rocks. The intermediate fit $k(\Phi) = c_1 \cdot \Phi^{3.4}$ can be used to describe the general k - Φ trend of this type of volcanic rock (Figure 4.11).

At higher vesicle contents it can be assumed that beyond the percolation threshold of ~ 30 % porosity, the contribution of a interconnected bubble network to the overall degassing increasingly dominates (i.e. for pumice, scoriae, or breadcrust bomb samples). Thus, the theoretical FPS percolation model (Chapter 4.1.2) should be appropriate as a first order approximation. In fact, a set of curves according to Equation (4.3) with $n = 2$ and $c_2 = 2 \cdot 10^{-15}$ does predict the trend of the highly porous volcanic rocks reasonably well. The best fit of the curve is achieved for a slightly higher percolation threshold of $\Phi_{cr} = 33$ (Figure 4.11).

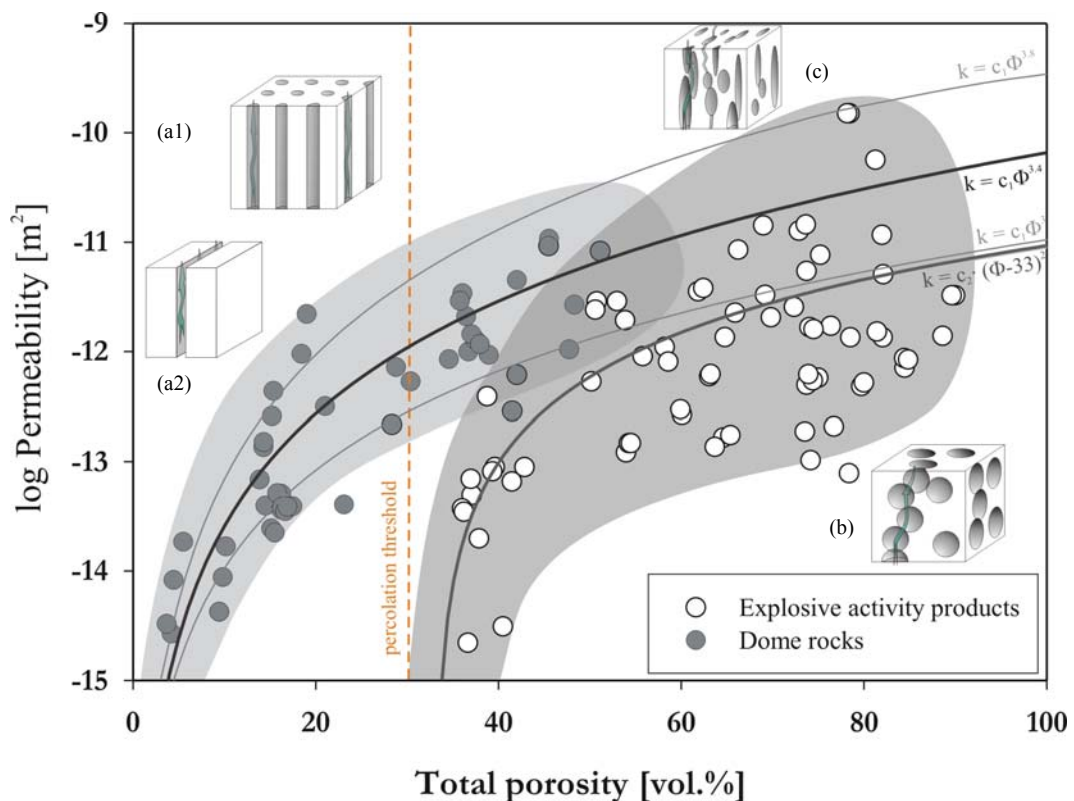


Figure 4.11: A combination of two distinct models might explain the high data separation in the low and medium porous range. Firstly, in the range of 3-30 vol.% an approximation based on a capillary tube model (a1) in combination to fracture flow model (a2) produces the best fit for the data. In this case $c_1 = 1 \cdot 10^{-17}$. Secondly, experimental results on samples with 30 - 80 vol.% can be approximated using the FPS-percolation theory (b) with $c_2 = 2 \cdot 10^{-15}$. The combination of both approaches might be used to represent laminated, possibly cracked, pumices (c).

Although these models indicate general trends and therefore should not be overinterpreted, the fact remains that the sets of curves according to $k(\Phi) = c_1 \cdot \Phi^3$ and to $k(\Phi) = c_2(\Phi - 30)^2$ converge in the region of highly permeable Krakatau, Stromboli, and Campi Flegrei pumices. This observation fits well with the known hybrid character of those pumices' pore structure: a network of coalesced, large, and often tubular shaped bubbles (e.g. Krakatau tube pumices). Likewise, the combination of the two different models helps to explain the outstanding increase in data scattering starting at the range of porosity, at which both pore geometries start to affect the gas flow properties coevally.

The diverse patterns of porosity-permeability dependency described above reflect the different pore structures responsible for the range of permeability values at a given porosity. For instance the permeability of Merapi andesite MP C and Bezymianny andesite BEZ E1 is almost 2 orders of magnitude higher than that of similarly porous Unzen breadcrust bombs (BKB). MP C and BEZ E1 both have ≤ 2 mm wide, irregular shaped, unevenly distributed vesicles giving rise to a relatively high connectivity (Figure 4.12). This pore structure may reflect the long retention period of these rocks in conduit and dome, giving rise to a highly advanced stage of bubble collapse and interconnection. In contrast, explosively erupted material like Pinatubo pumice (PIN B) or Stromboli scoria (STR Br) contain partly elongated, but well distributed bubbles of several millimetres length, with a lower degree of connectivity. Breadcrust bombs represent an extreme example of this kind of pore structure: they may have total porosities of up to 54 % but, due to their short time span available for bubble formation (basically from ejection to trespassing glass transition temperature T_g), small bubble sizes, a rather uniform bubble size distribution and an associated low connectivity. These factors lead to relatively low permeability values (Figure 4.12). So it can be concluded that in this type of volcanic rocks, the distribution of vesicles, rather than the bubble elongation or vesicle size appears to affect the permeability. Another notable fact is that the wide range of the permeability values within a single rock type (e.g. Lipari pumice with ~ 38 vol% porosity, see Figure 4.9) of more than 2 orders of magnitude generally reflects the influence of heterogeneities and sample orientation, especially in rocks with elongated bubbles.

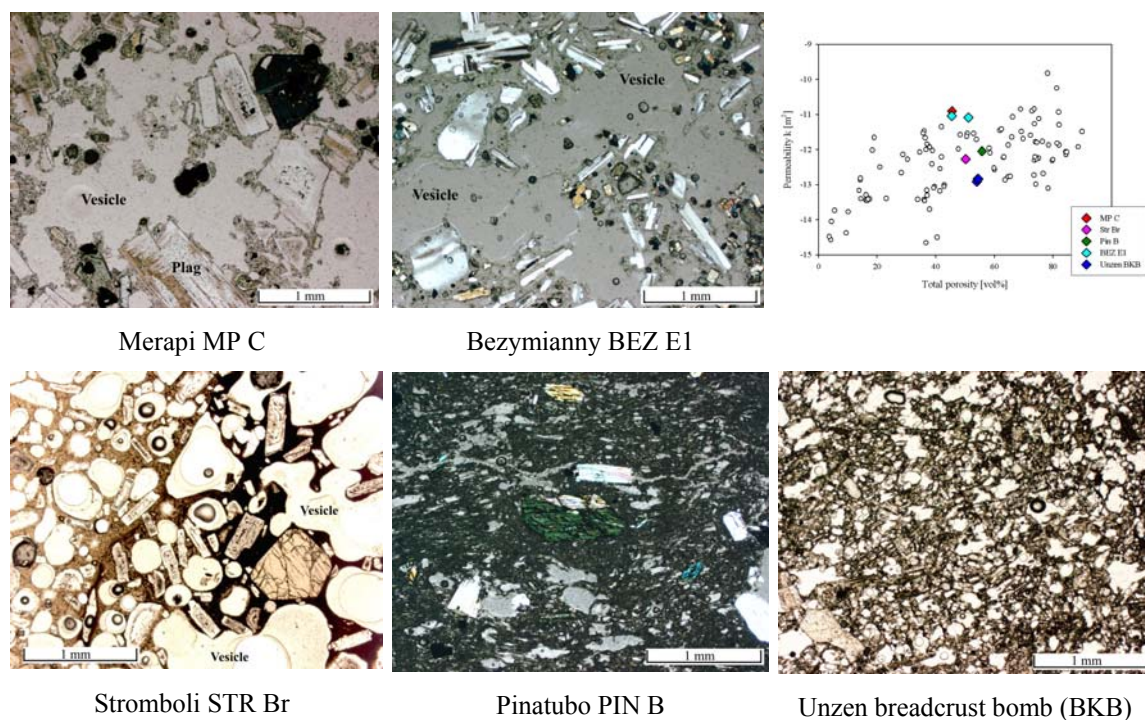


Figure 4.12: Different types of pore structures responsible for the range of permeability values at a given porosity. The samples MP C and BEZ E1 represent products of effusive dome growth, with a network of large, highly deformed and interconnected pores. The samples, STR Br, PIN B and Unzen breadcrust bomb represent products of explosive activity. The bubbles are less deformed and show a lower degree of coalescence. Note that in all the examples shown the permeability of the explosive products is lower than that of the effusive products, despite a similar or higher porosity. This clearly supports the strong influence of pore texture and connectivity on the permeability, rather than the total pore volume.

4.5 High-temperature permeability measurements – experimental difficulties, possible solutions and preliminary results

Volcanic rocks may be subject to post-eruptive alterations which might affect their permeability. Particularly microfracturing during cooling can be considered as a process that might significantly increase the permeability in comparison to that of the original magma. This effect might be negligible at high-porous rocks, as here the degassing predominantly occurs through bubble interconnections (*Melnik & Sparks 2002*), but at dome rocks with a generally low porosity an influence of microfractures may be considerable. Permeability experiments at temperatures close to natural conditions, as they are met for instance in a conduit or volcanic dome, might therefore provide more

realistic data for conduit dynamics models, if they are capable of re-enacting the original, pre-eruptive state of a sample.

4.5.1 Experimental approaches

However, permeability measurements at high temperatures represent, from the experimental point of view, a major technical challenge in terms of operational demands, material deformation and the steadiness of the experimental conditions. The biggest problem in this context is the gas tight fit of the sample-autoclave-interface. In the following section an overview of some of the approaches pursued during this project, and the problems faced, will be given. For the tests, the gas discharge rates of samples cylinders assembled with the respective approach were compared to discharge rates obtained by the standard room-temperature method using crystal bond as a adhesive.

- 1) The first approach was to glue the sample into a steel sample holder, in analogy to the room-temperature setup (Chapter 4.2.1 & Appendix A). As adhesive, a high temperature cement (*Sauereisen No. 13*) was used. At 850°C gas leakage was observed. The cause of this leakage is most probably the different thermal expansion of steel and rock. With an expansion coefficient $\alpha \sim 18\text{-}19 \cdot 10^{-6} \text{ K}^{-1}$ (Wegst 1989) the thermal expansion of steel is considerable larger than that of silicic rocks ($\alpha \sim 5\text{-}10 \cdot 10^{-6} \text{ K}^{-1}$; e.g. Strohmeyer 2003) and the thermal expansion of the HT cement ($4.68 \cdot 10^{-6} \text{ K}^{-1}$; *Sauereisen Zircon potting cement No. 13 datasheet*) is not able to compensate this, resulting in gas leakage between sample and sample holder.
- 2) Ceramic sample holder tubes with lower thermal expansivities (Alsint, $\alpha \sim 8 \cdot 10^{-6} \text{ K}^{-1}$ and fired pyrophyllite, $\alpha \sim 3 \cdot 10^{-6} \text{ K}^{-1}$; α -values from http://www.haldenwanger.de/pdf/materials_e_06.pdf and www.ceramic-substrates.co.uk/material, respectively) were used. Again, the sample cylinders were glued using the high-temperature cement. Problems with this approach were: (a) The Pyrophyllit sample holders were too fragile to withstand the uniaxial pressures required to tighten it against two copper sealing rings above and below the sample holder. (b) The surface of the stronger Alsint (an Al_2O_3 ceramic) sample holder didn't conjoin properly with the cement. Gas leakage therefore most likely occurred through the Alsint-cement interface. (c) The low thermal expansion coefficients of the ceramic

tubes in comparison to that of the sample in few cases caused rupture of the ceramic tube.

- 3) To allow for a dynamical adjustment of the sealing material between sample and sample holder, a borosilicate glass tube was placed around the samples. For a glass tube of a specified glass composition there exists a temperature window above the softening point, in which the glass viscosity causes gravitational collapse of the tube and hence closure of the space between the autoclave and the sample. For borosilicate glass, 850 °C is within this temperature window. However, it was found that the gravitational collapse didn't create a bonding between the glass and the rough sample surface strong enough to withstand to applied gas overpressures. Gas leakage, most likely through the glass-sample interface, was the consequence.
- 4) The following three approaches were based on grouting a powdery substance into the space between autoclave and sample: the sample cylinder is placed in the autoclave, free-standing on the conical shaped inset on top of the sample (in measurement position). Then gradually the powder is filled in the space between sample and autoclave (Figure 4.13). About every 5 mm, the loose powder grains are compressed in a hydraulic press with not more than 10 bar, using a steel tube with 28 mm outer and ~25mm inner diameter as plunger. The procedure is repeated, until the compressed powder coat covers the entire sample length. The advantage of this method is that the sealing compound can be, if required, further compressed during the high-T experiment by moving up a metal tube through the retightening of the lower screw nut. The induced deformation of the powder continuously seals the system. First attempts with this method were conducted using compacted CaF₂-powder. This material is often used as sealing material in high-temperature experimental petrology, since it has a high melting point > 1360 °C. However, the problem in this case was that the Calcium Fluoride grains are too rigid to be mechanically deformable at the applied compressive pressures, and therefore did not form a compact, gas-tight filling. The overpressurized gas in the grain interstices caused – upon rapid decompression – a complete blow-out of the material.
- 5) Though softer pyrophyllite or talcum powder could be compressed to a compact seal, dehydration reactions at high temperatures caused volume reduction of the sealing coat and subsequent gas leakage.

- 6) Granular NaCl, with a melting point 801 °C, turned out to be the most promising material for this approach, since it (due to its plasticity) mechanically deforms in a ductile manner at comparatively low pressures and by that forms a compact quasi-solid body around the sample (Figure 4.13). Further, it has a comparatively high thermal expansion of $\sim 40\text{-}60 \cdot 10^{-6} \text{ K}^{-1}$ (Enck & Dommel 1965), which might lead to additional sealing pressure. The problems of this method are (a) the comparatively low melting point of the salt, which allows, considering impurities, experimental temperatures of max. 750 °C, and (b) uncertainties about the actual applied radial, compressional force on the sample. This force might, for example, be responsible for the narrowing of fractures, which in turn has considerable effects on the permeability. At weaker samples, the compression might even cause sample failure.
- 7) A further approach to solve the problem of gas leakage at high temperature could lie in the use of a second, independent gas pressure system to press a sealing metal foil against the sample cylinders outer surface. This project, however, couldn't be pursued due to difficulties in material acquisition.

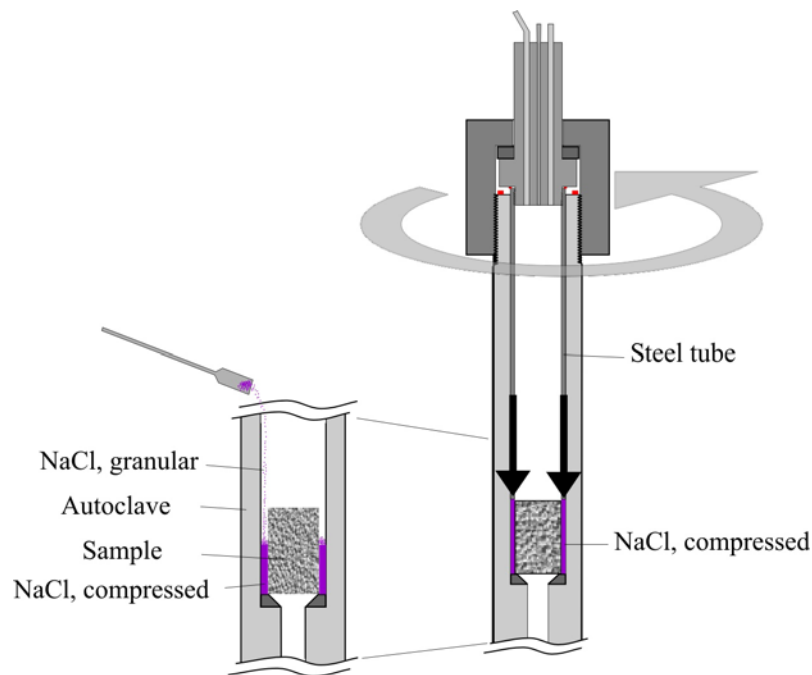


Figure 4.13: Sample mounting for high-temperature permeability measurements. In this setup, the sample cylinder is sealed against the autoclave using compressed NaCl. The salt is carefully filled into the spacing between the autoclave and the sample (left), and is thereby gradually compacted using a steel tube. For the experiment the steel tube is screwed down tightly, so that the tube-salt interface is impermeable (right). During the experiment possible leakage due to thermal expansion can be closed by readjusting the pressure on the salt coating.

4.5.2 High-temperature measurements with a NaCl sealing

Experimental procedure

Considering the NaCl-sealing-method as the most feasible one, permeability measurements have been performed on two samples from Mt. Unzen, one from Merapi and one from Campi Flegrei. The Unzen samples are dacitic dome rocks with a porosity of 4 and 13 vol%, respectively. The Merapi sample is a low-permeable andesitic dome rock with ~36 vol% porosity; the Campi Flegrei sample is a pumiceous trachyte from the 1538 Monte Nuovo eruption with 47 vol% porosity. The sample cylinders are centred in the hottest zone of the autoclave. Investigations of *Spieler* 2001 revealed a temperature gradient of less than 12 °C over the sample length of 60 mm. During the experiments the temperature of the gas below the sample (which is usually 30-40 °C below the furnace temperature) is surveyed with a thermocouple directly at the bottom of the sample cylinder. The experimental procedure after sample installation was as follows:

- a) permeability measurement at room temperature
- b) heating of the autoclave. The final temperature T_{\max} of 750 °C was reached after approximately 60 minutes
- c) thermal equilibration for at least 120 minutes, under argon pressure
- d) rapid-decompression permeability measurement at 750 °C
- e) cooling to room temperature (3-4 h)
- f) permeability measurement at room temperature.

Results

Regarding the resulting pressure trends of the Unzen dacite and Merapi andesite experiments, the following statements can be made (Figure 4.14): (1) The decompression profiles for the room temperature experiments before and after the heat treatment are similar in all three cases. This similarity indicates that at the applied temperature conditions and time scales, independent from textural features and porosity, no permanent changes in the samples pore texture (e.g. fracture healing) occurred. This is, however, not surprising as the temperature of 750 °C is, in the case of Unzen dacites and Merapi andesites, more than 100 °C below the glass transition temperature of the rock's glass phase (*Hess*, pers. comm.), and substantially below the solidus of

representative dacites/ andesites. Accordingly, processes like partial melting or mobilization of the glass phase and subsequent fracture healing cannot be expected in these samples under the given conditions. (2) The gas filtration rate is considerably lower at high temperatures (expressed by a longer pressure equilibration time). This decrease in gas filtration rate might be partially caused by a change in gas properties with higher temperatures: the viscosity of Argon increases from $2.26 \cdot 10^{-5}$ (25 °C) to max. $5.34 \cdot 10^{-5}$ Pas (730 °C; *Verein deutscher Ingenieure* 2002). As the transient code doesn't account for different gas viscosities when calculating k , a temperature-correction is required for the determination of the real permeability value:

$$k_{\text{real}} = k_{\text{calculated}} \cdot (\mu_{\text{Argon, high-T}} / \mu_{\text{Argon, room-T}}) \quad (4.14)$$

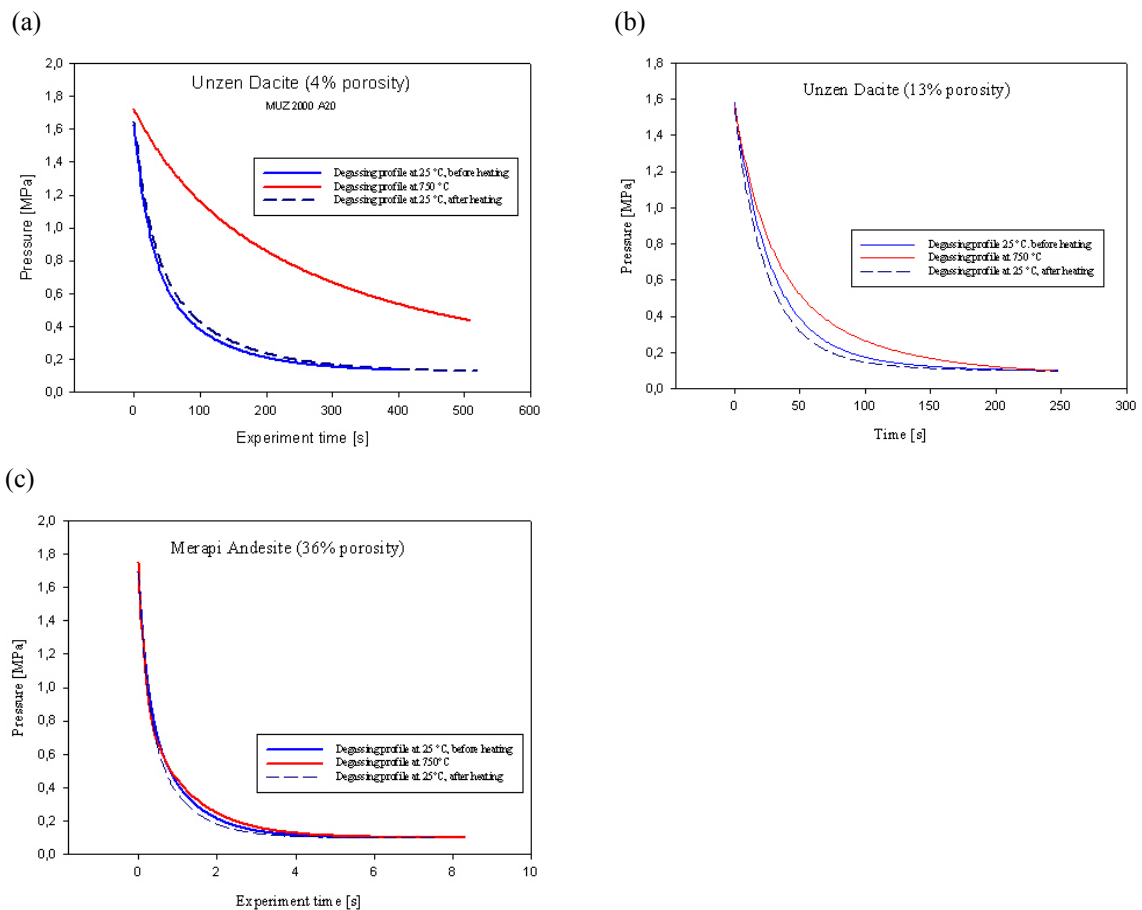


Figure 4.14: (a)–(c) Pressure profiles for Unzen Dacites (4 and 13 vol% porosity, resp.), and a Merapi Andesite (36 vol% porosity). Displayed are the decompression curve at 750 °C, and two curves at room temperature before and after heating, respectively. Filtration rates at high T are generally lower.

Interpretations

The uncorrected and corrected permeability values in comparison to the room temperature data are displayed in Figure 4.15. The results illustrate that the corrected, real permeability of the samples at high temperatures is effectively higher than at room temperature. This allows the interpretation that thermal expansion of the entire sample leads to an extension of the pore interconnections responsible for gas flow.

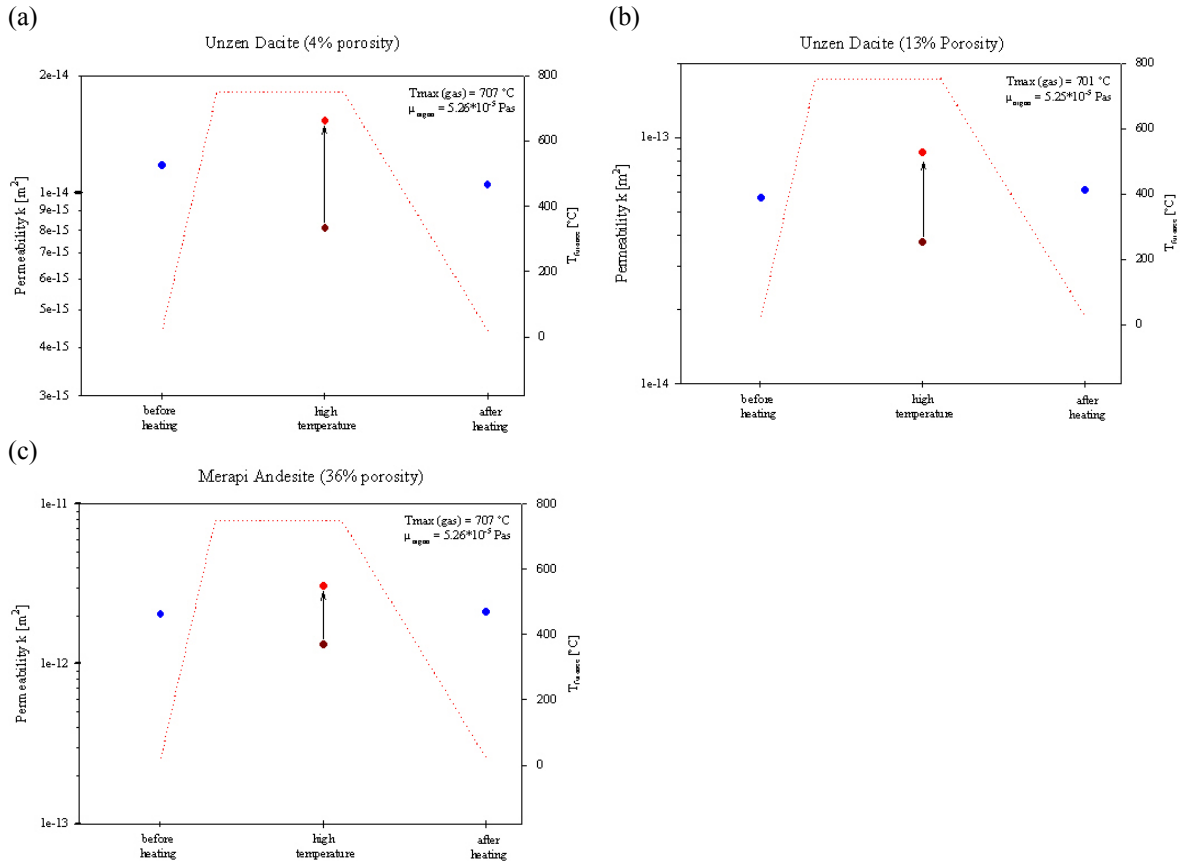


Figure 4.15: Permeability development during high-temperature experiments. The room-temperature experiments before and after the heating are similar within a 10 %-interval for all three cases. This indicates that no permanent changes in the samples structure took place. At high temperatures the permeability value, calculated without temperature correction, drops about 30 % (dark red dots). If, however, the changed gas properties are taken into account, permeability gets effectively higher (red dots). The red dotted line schematically indicates the temperature course of the experiment.

This effect can be illustrated regarding a comparative degassing experiment using a steel cylinder with seven capillary drillings as sample representative (Figure 4.16). Although the gas viscosity is higher at high temperatures and the flow rate should

theoretically decrease, the gas filtration rate is higher at 850 °C. This is most probably caused by an extension of the capillaries diameter by thermal expansion.

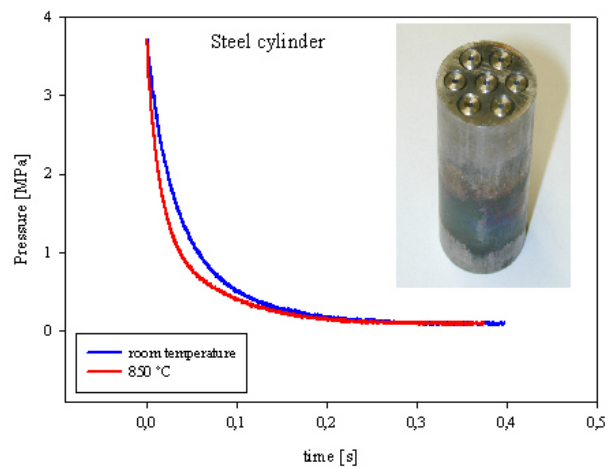


Figure 4.16: Pressure profiles of a degassing experiment at room temperature and 850 °C, performed on a steel cylinder with seven 0.2 mm drillings. Despite a higher gas viscosity, in this case the filtration rate of the high temperature experiment is higher.

It can be therefore concluded: (a) gas filtration through the samples is slower at high temperatures, though (b) the effective permeability of the samples is higher.

However, these conclusions must be seen under certain restrictions: it must be taken into account that the radial compressive forces induced by the salt upon the sample cylinder may counteract the extensional forces of the thermal expansion. This might lower both the calculated and the corrected permeability value. As the gas filtration properties of fracture-like geometries are more sensitive to volumetric changes than that of bubble interconnections, this compressive permeability reduction assumingly is more effective at dense samples with prominent fracture zones, rather than at high-porous samples. Since the amount of radial pressure and the actual effect of the compression on the sample can not fully be quantified and controlled in the present setup, uncertainties concerning the interpretation of the obtained permeability data remain.

To address the question whether permanent changes in a sample's textural properties can principally occur at the given experimental circumstances, a Campi Flegrei sample with trachytic, peralkaline composition was heated above the glass transition temperature of the material (~605-690 °C depending on water content; *Hess*, pers. comm.), and kept at 750 °C for five hours (Figure 4.17). Permeability measurements were performed subsequently during the heating phase without rapid

decompression, by supplying a defined ‘pulse’ of argon gas into the volume below the sample. Because the supplied gas was at room-temperature, no viscosity-correction for the permeability calculation was performed. As a slight temperature-increase of the gas during filtration can be assumed, the permeability values from the four high-temperature experiments in Figure 4.17 likely represent minimum values. But, as the conditions were equal for all four experiments, they allow a comparative examination: the results show no apparent changes in permeability throughout the entire experiment (Figure 4.17). It can therefore be concluded that deformation kinetics in these experiments are far too slow to cause any substantial structural modifications in the materials pores or fractures, even if the glass transition temperature is exceeded. Considering that in the present experiments no axial stresses are applied to the rock cylinder and deformation would have to occur purely gravitationally, these results correspond to the expected behaviour of highly viscous melts.

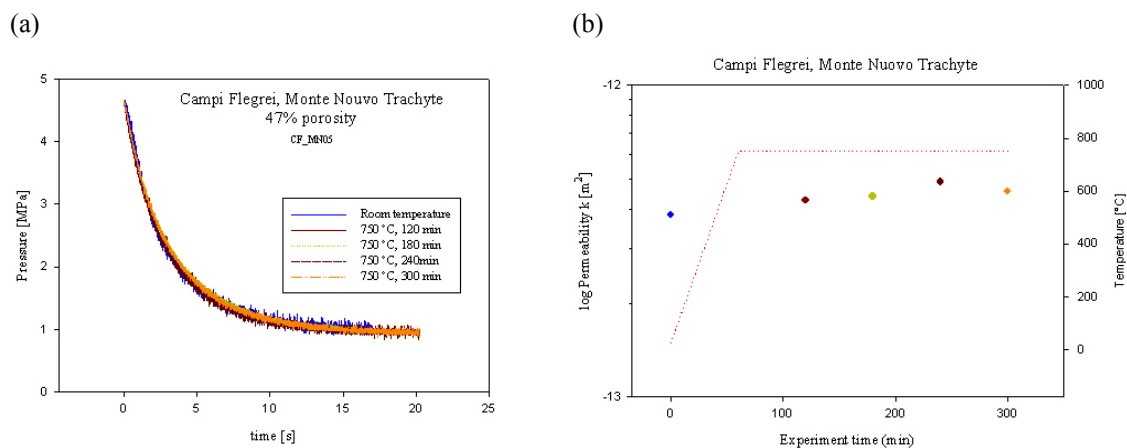


Figure 4.17: Long-term high temperature permeability measurement on a trachytic sample from Monte Nuovo, Campi Flegrei. (a) Pressure profiles from one room temperature and four experiments at 750 °C furnace temperature, measured in 1h-intervals. (b) Calculated permeability values (uncorrected). As no considerable changes in permeability throughout the entire experiment can be noted, permanent changes of the pore texture can be excluded under the given circumstances. The red dotted line schematically indicates the temperature course of the experiment.

5 Permeability control on volcanic fragmentation processes

5.1 Introduction

Fragmentation of porous magma bearing gas overpressure is considered to be a crucial process generating explosive volcanic eruptions. A decompressive event (e.g. rapid magma ascent, landslide, dome collapse, plug failure) disrupts the stress equilibrium between the gas phase and the surrounding melt. When the gas in the pores is exposed to a pressure gradient, it may either fragment the surrounding magma, or escape from the magma along an existing pathway of cracks and interconnected bubbles. Thus magma permeability can be a decisive parameter in determining whether an eruption experiences fragmentation; that is, whether it is explosive or effusive, or exhibits a temporal transition between the two eruptive styles. An experimental investigation of the interconnection between degassing efficiency and fragmentation behaviour of volcanic rocks is therefore of great importance for a refined understanding of eruption mechanisms.

5.2 Bubble overpressure and its reduction

Of the various phenomena that can drive magma fragmentation, internal bubble overpressure is considered to be amongst the most important (*Alidibirov & Dingwell 1996a, 2000; Cashman et al. 2000; Ichihara et al. 2002*). The propelling force of this phenomenon, exerted upon the pyroclastic products, should depend on magma porosity, gas overpressure, and the ability to preserve the overpressure condition for a certain time. The latter magma property is strongly dependent on its degassing efficiency or permeability. Magma porosity and permeability are normally linked by a complex positive relationship, as a higher proportion of pore space generally leads to a greater probability of pore interconnectedness (see chapter 3; *Eichelberger et al., 1986; Klug and Cashman, 1996; Blower, 2001a*).

As outlined in chapter 1, bubbles grow within rising magma due to overpressure fed by volatile diffusion and decompression. As the magmastatic pressure in the magma column decreases during ascent, i) volatile solubility decreases and, upon saturation and bubble nucleation, volatiles diffuse from the liquid into the bubbles; and ii) bubbles

expand to compensate for the resulting pressure disequilibrium. Magma viscosity and surface tension counteract and may effectively retard bubble growth, and the balance between these contributions determines the pressure at any moment within the individual bubbles (Sparks 1978; Sparks 1997; Thomas *et al.* 1994; Navon 1998; Lensky *et al.* 2001). If, however, during magma ascent, a connected network of void space (bubbles and/or cracks) is established, then gas flows down local pressure gradients and eventually escapes to the atmosphere or the country rock. Further, if the effective viscosity of the magma around the bubbles yields a magma relaxation time scale that is significantly longer than the time scale of magma ascent, then a closed pore network may cause high overpressures to be generated in isolated pores or network sections (Lensky *et al.* 2001, 2004). If magma decompression accelerates (due to either internal or external forces), two possible scenarios are conceivable (Figure 5.1): (1) a highly interconnected pore network is established and its permeability is sufficiently high to efficiently reduce vesicle overpressure by gas filtration (Figure 5.1b), or (2) the permeability of the network (or cluster of isolated pores) is low and gas overpressure cannot be reduced within the time scale required to prevent fragmentation (Figure 5.1c). In the latter case, the expansion of the pressurized gas may cause bubble wall failure and the fragmentation of magma into pyroclasts (Alidibirov & Dingwell, 1996, 2000; Zhang, 1999).

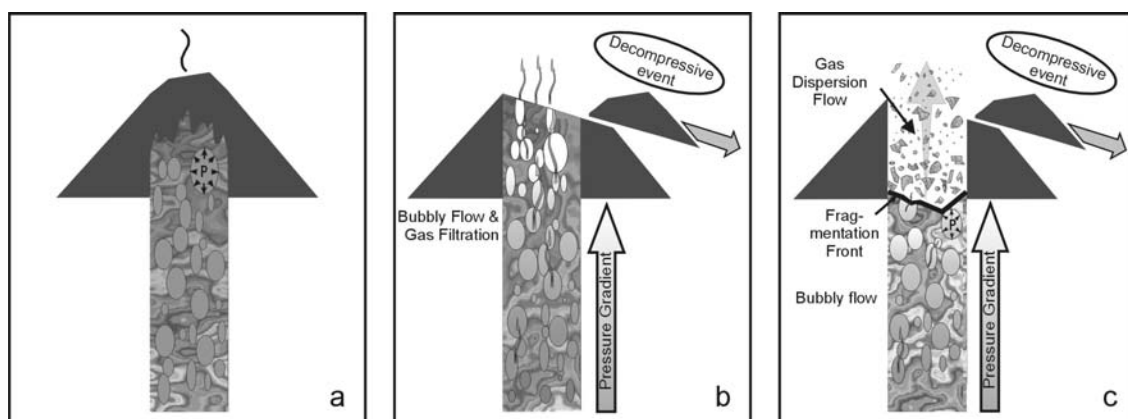


Figure 5.1: **a:** In a stable system the bubble overpressure is in structural equilibrium with the surrounding magma. **b:** A decompression event causes a pressure gradient within the magma column. If the permeability of the system is high enough, the gas will escape by filtration. **c:** At a low magma permeability, gas flow is hindered and vesicle overpressure may cause bubble wall failure. On the resultant newly exposed surface a steep pressure gradient between the gas phase in the bubbles and the atmosphere develops and induces magma fragmentation by a sudden expansion of the highly compressed gas phase. This is considered to occur in a layer-by-layer manner along a downward propagating fragmentation front (Alidibirov & Dingwell, 1996; Spieler *et al.*, 2004b Kennedy *et al.* 2004).

These two scenarios illustrate qualitatively the inexorable impact of permeability on the fragmentation of porous magma. In order to improve models of magma fragmentation and to permit more reliable hazard assessment, it is therefore of paramount importance to know the permeability of the investigated volcanic material (*Koyaguchi & Mitani 2005; Melnik et al. 2005*). Moreover, it now appears essential to quantify the dependence of the “fragmentation threshold” (the minimum gas overpressure required to initiate fragmentation; *Spieler et al. 2004b*) of porous material on its permeability coefficient.

5.3 Experimental procedure

To this end a combined investigation of permeability measurements and fragmentation experiments has been conducted on a selected variety of 32 dome rock and pumice samples. The permeability determinations and additional fragmentation threshold experiments were performed on the shock-tube-like fragmentation apparatus described in Chapter 4.

First, the permeability of a sample cylinder was measured according to the method described in Chapter 4.2, and subsequently the same sample was built into another autoclave designed for fragmentation threshold and speed analysis (*Spieler et al. 2004a, Scheu 2005*). The setup principles for the fragmentation experiments are schematically displayed in Figure 5.2. Above a specific ΔP_i , the overpressure in the pore space cannot be reduced sufficiently fast by gas filtration. In consequence, the matrix skeleton of the sample fails on the spots of stress accumulation, causing a layer-by-layer fragmentation of the rock cylinder (*Alidibirov & Dingwell 1996a, Spieler et al. 2004b*). This specific pressure difference is referred to as “fragmentation threshold” (ΔP_{fr}). ΔP_{fr} of a sample is determined by a series of experiments with constantly increasing ΔP_i , until ΔP_{fr} has been reached, and the entire sample has been fragmented. Normally, the initial pressure is increased in steps of 0.5 MPa. The time delay of the pressure drop due to rapid decompression recorded by two pressure transducers above and below the sample can be used to determine the speed of the downward propagation fragmentation front (*Spieler 2004a, Scheu 2005*).

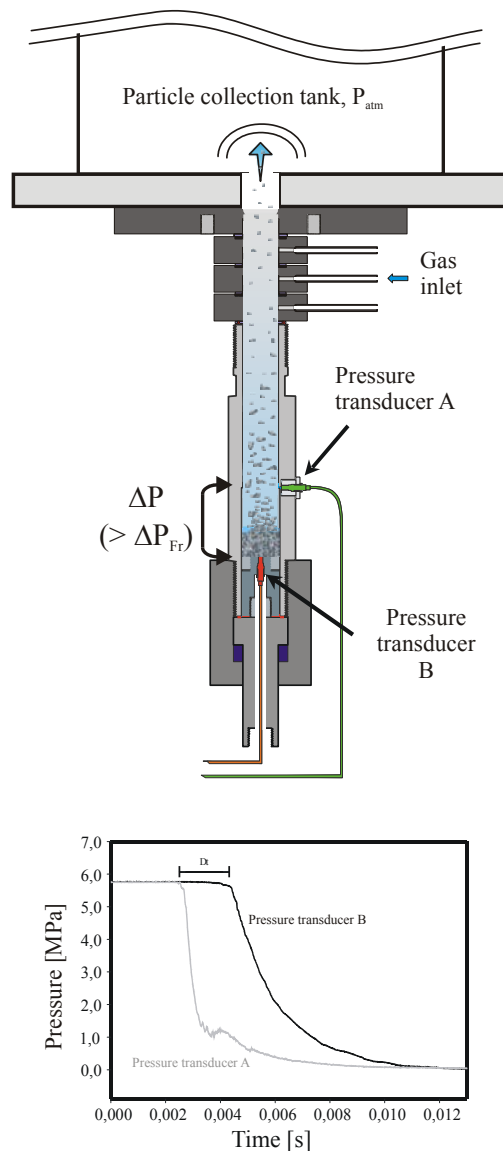


Figure 5.2: Detailed set-up of the autoclave section used for fragmentation threshold and -speed experiments. Above a specific ΔP_i , the overpressure in the pore space cannot be reduced sufficiently fast by gas filtration and the sample fragments. For the determination of ΔP_{fr} , the sample is set into an autoclave especially designed for fragmentation threshold and -speed analysis. Then, in a series of experiments, ΔP_i is constantly increased until the sample fragments. The minimum overpressure to fragment a specific sample is defined as ΔP_{fr} . The diagram below shows a typical recording of the pressure trends that display the time delay Δt between the impinging of the decompression fronts on the sample's surface and on its base after complete fragmentation.

5.4 The effect of permeability on the fragmentation threshold

Figure 5.3 includes the experimentally derived high- and room-temperature fragmentation threshold values of Spieler et al. (2004b), Scheu et al. (2006) and Kueppers et al. (2006), together with those of this study. As in the experiments isolated bubbles bear no overpressure and thus do not contribute to the fragmentation process, for the following considerations the values of the open porosity has been used. In general, the results of room-temperature experiments appear not to differ systematically from experiments performed at 850 °C. ΔP_{fr} and the sample's open porosity, ϕ , show a strongly non-linear dependency, which can be approximated as a first-order inverse correlation. Spieler et al. (2004b) deduced a fragmentation criterion of the form $\Delta P_{fr} = \sigma_m / \phi$, with σ_m being the effective tensile strength of a compound matrix. Clear deviations from this trend towards higher threshold values can however be noted, predominantly in the high-porosity region. These data may indicate an increasing influence of rock permeability on the fragmentation threshold.

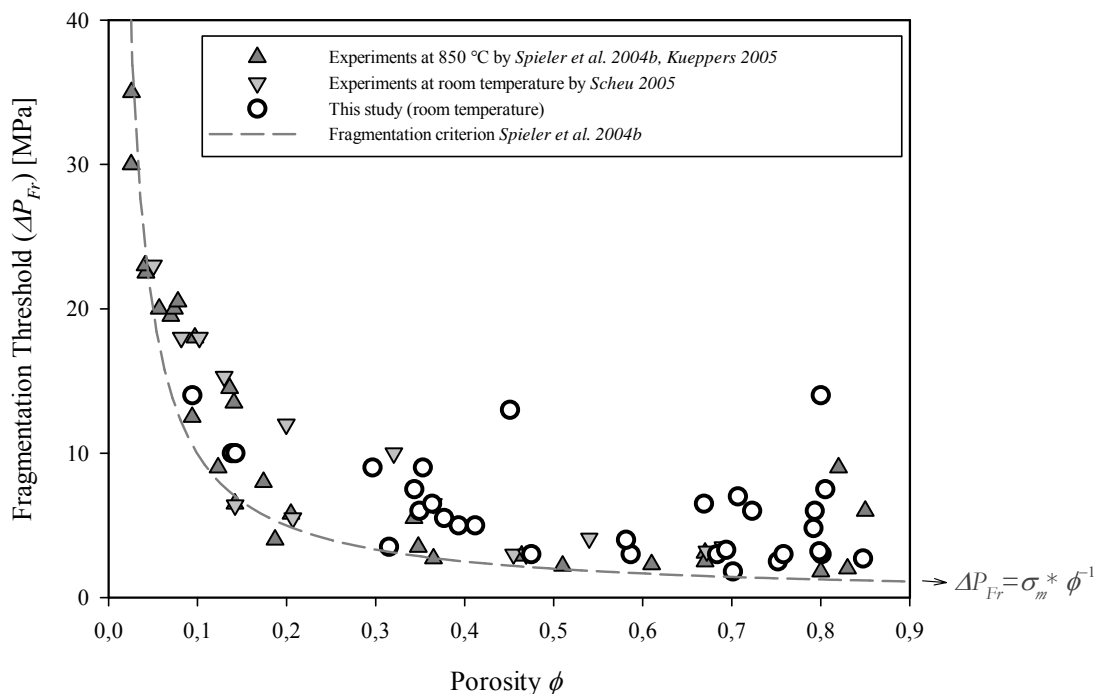


Figure 5.3: Experimentally determined high- and room-temperature fragmentation threshold values from Spieler et al., 2004, Scheu et al., 2006, Kueppers et al., 2006, and this study. Porosity values are given in void fraction between 0 and 1. Deviations from a first-order inverse correlation of ΔP_{fr} with the samples open porosity as proposed by Spieler et al., 2004, are evident especially in highly porous samples, indicating an increasing influence of a high permeability on the fragmentation behaviour.

In Figure 5.4 the linear permeability values of the samples used for the combined permeability-fragmentation study are highlighted. The comparison of Figure 5.3 and Figure 5.4 reveals conspicuous accordance in the porosity intervals 0.35-0.45 and 0.70-0.80. In both cases exceptionally high amplitudes of permeability values of almost four orders of magnitude coincides with exceptional deviations of the fragmentation threshold pressures from a first-order inverse trend. This analogy foreshadows the influence of the rock permeability on the fragmentation threshold. The experimental results of the porosity, permeability and fragmentation threshold determinations are compiled in Table 5.1.

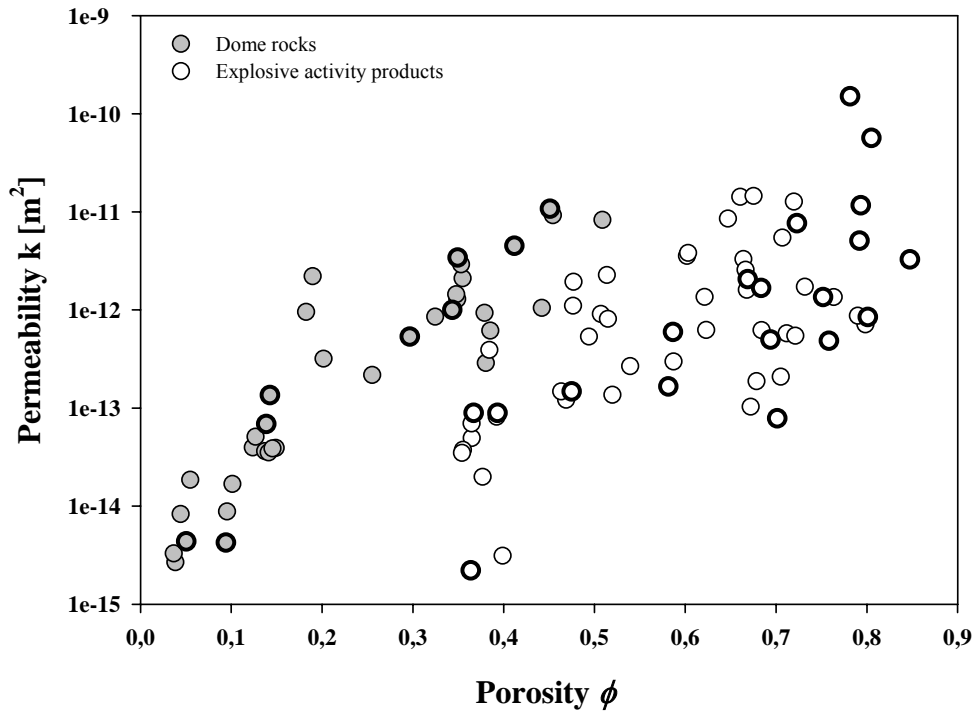


Figure 5.4: Permeability-porosity relations of the samples used for permeability-fragmentation experiments (highlighted with a black ring). Porosity values are given in void fraction between 0 and 1.

Table 5.1: Results of combined porosity, permeability, and fragmentation threshold determinations for 22 pumice/ breadcrust bomb samples and 10 dome rock samples

Sample	Open porosity ϕ	Permeability k [m^2]	Fragmentation threshold ΔP_{Fr} [MPa]	Energy Density at ΔP_{Fr} [$10^{-6}J/m^3$] (= $\Delta P_{Fr} * \phi$)
<u>Explosive activity products</u>				
Lipari B03	0.587	5.96e-13	3.0	1.7595
Lipari B04	0.581	1.66e-13	4.0	2.3252
Lipari C02	0.694	4.98e-13	3.3	2.2895
Lipari E01	0.393	8.90e-14	5.0	1.9660
Lipari E09	0.377	1.99e-14	5.5	2.0730
Lipari E20	0.364	2.20e-15	6.5	2.3633
Lipari F03	0.758	4.85e-13	3.0	2.2746
Unzen VUL02	0.475	1.47e-13	3.0	1.4247
Unzen BKB38	0.367	8.90e-14	4.1	1.5047
Campi Flegrei AMS 02	0.707	5.46e-12	7.0	4.9483
Campi Flegrei AMS 03	0.793	1.17e-11	6.0	4.7598
Campi Flegrei AMS 06	0.669	2.75e-12	6.5	4.3466
Campi Flegrei AMS 15	0.723	9.86e-12	6.0	4.3368
Campi Flegrei AMS 27	0.792	5.08e-12	4.8	3.8011
Montserrat 33	0.684	1.67e-12	3.0	2.0505
Krakatau RAK301	0.848	3.27e-12	2.7	2.2883
Krakatau tube pumice03	0.781	1.26e-10	14.0	11.2000
Santorini 01	0.752	1.35e-12	2.5	1.8793
Santorini 03	0.701	7.83e-14	1.8	1.2622
Santorini 05	0.798	7.13e-13	3.2	2.5549
Santorini 12	0.801	8.47e-13	3.0	2.4027
Stromboli biondo01	0.805	5.65e-11	7.5	6.0375
<u>Dome rocks</u>				
Unzen 01 A17	0.050	4.35e-15	23.0	1.1592
Unzen 01 F18	0.343	9.99e-13	7.5	2.5748
Unzen 00 G18	0.412	4.50e-12	5.0	2.0590
Unzen 00 G52	0.349	3.41e-12	6.0	2.0958
Merapi A02	0.139	6.88e-14	10.0	1.3850
Merapi A03	0.143	1.35e-13	10.0	1.4250
Merapi B04	0.297	4.64e-13	9.0	2.6694
Merapi B12	0.353	2.91e-12	9.0	3.1770
Merapi C01	0.451	1.26e-11	13.0	5.8630
Augustine B102	0.094	4.24e-15	14.0	1.3174

In Figure 5.5 the permeability is plotted against the respective fragmentation threshold of a sample. Regarding the distribution of the $(k, \Delta P_{fr})$ pairs of variants, the following points can be stated: (1) In analogy to the permeability-porosity trends (Chapter 4.4) a distinction between dome rocks and explosive activity products can be made. (2) The data points of both groups follow similarly shaped trends, but parallel translated along the ΔP_{fr} – axis, with dome rocks generally showing higher threshold pressures. A noticeable deviation from this parallelism can be observed for very low permeability values. (3) Both trends seem to follow a more or less pronounced parabolic curvature with a minimum ΔP_{fr} at permeability values between 10^{-12} and 10^{-11} m^2 . Again, this observation implicates an influence of high k values towards an increase of ΔP_{fr} . (4) However, the general view of the plot yields a high data scatter, because the very different porosities of the samples are not taken into account. Therefore this diagram helps to underpin the influence of the permeability on the fragmentation threshold but appears to be less suitable for an accurate quantitative statement.

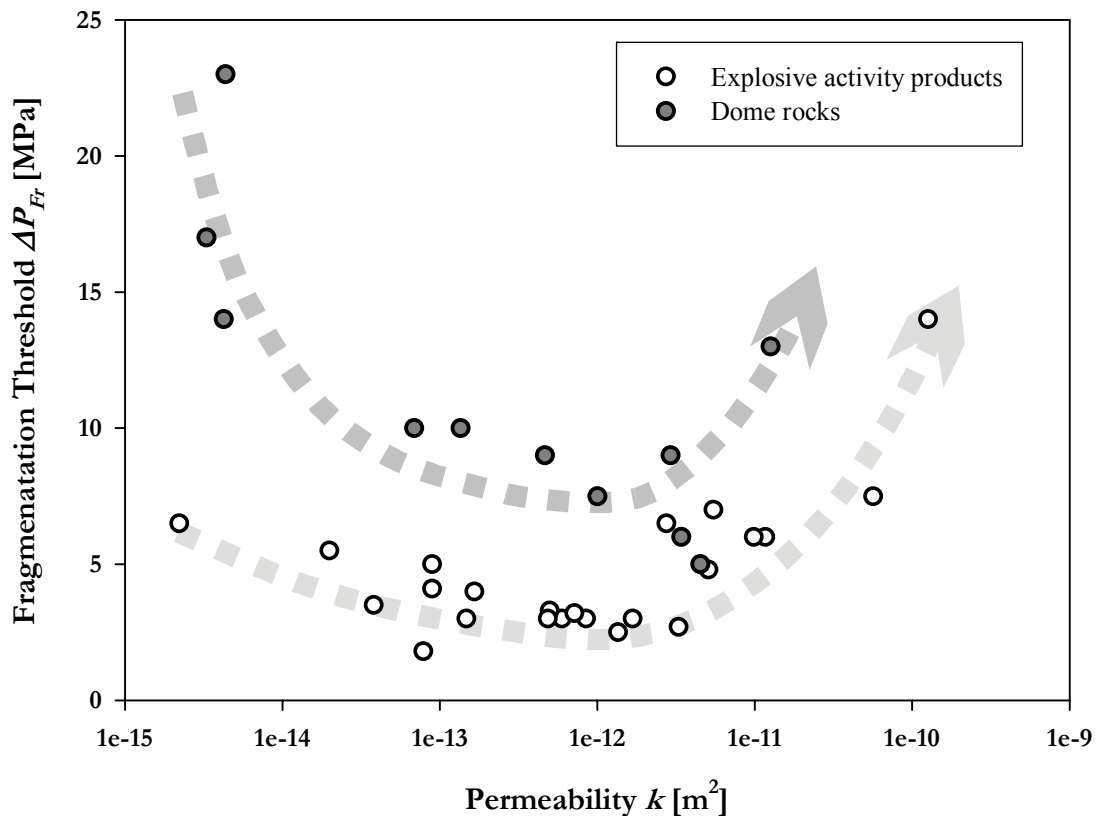


Figure 5.5: Permeability values plotted against the corresponding fragmentation threshold. Samples from dome rocks and from explosive activity both follow trends with a parabolic curvature, but are parallel translated. The sharp increase at high permeabilities indicates an increasing influence of effective degassing on the fragmentation process.

The most evident way to avoid data scatter due to different porosities is to choose a set of samples with a similar pore volume fraction but different permeabilities and study their fragmentation behaviour. This was done for a set of 7 samples with a porosity of approximately 0.8 and permeability coefficients ranging from $8.4 \cdot 10^{-13}$ to $1.6 \cdot 10^{-10} \text{ m}^2$ (Figure 5.6a). The plot of the determined ΔP_{fr} values of these samples versus the measured k reveals an explicit power-law increase of the fragmentation threshold with increasing permeability (Figure 5.6b). The trend can be best-fitted with the curve $\Delta P_{fr} = 3.48 + 3.43 \cdot 10^8 \cdot k^{0.76}$.

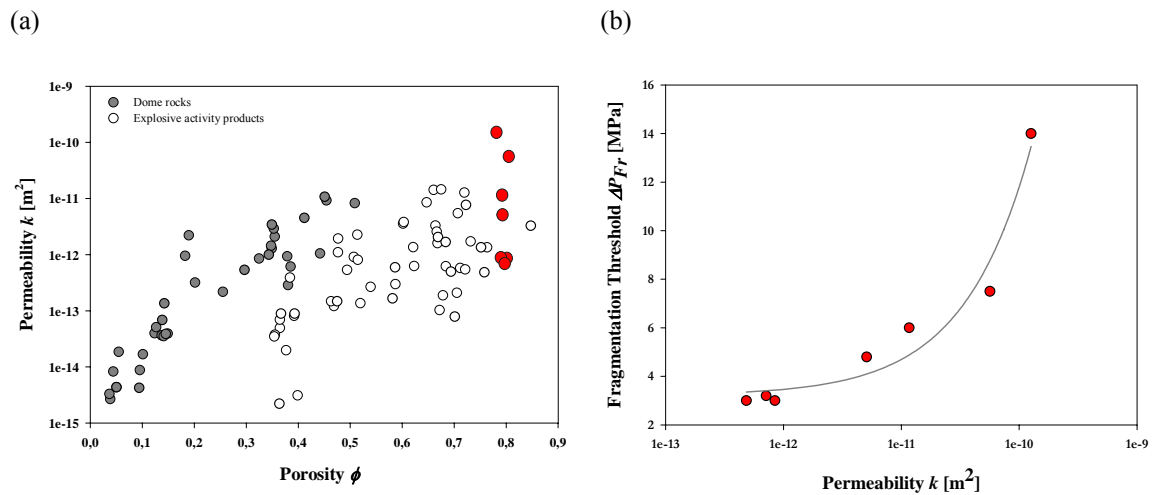


Figure 5.6: (a) porosity-adjusted influence of permeability on the fragmentation threshold is easiest achieved by taking samples with approximately the same porosity. In the present case, seven samples with ~80 vol% porosity were chosen (red dots), (b) k - ΔP_{fr} relation for seven samples with ~80 vol% porosity. An explicit increase following a power-law can be observed.

5.4.1 Fragmentation energy density

The concept of the energy responsible for the fragmentation process allows the incorporation of the pore volume to the fragmentation threshold examinations for the whole set of investigated samples (Scheu 2005): The energy, E , which is needed to initiate and sustain a fragmentation process, is provided by the expansion of the pressurized gas located in the pore space of the samples. If the experiments are assumed to be isothermal due to the high heat capacity of the sample matrix and a negligible temperature drop in the gas volume below the sample after decompression (see Chapter 4.2.2), E can be written as

$$E = \Delta P \cdot \phi \cdot V, \quad (5.1)$$

with ΔP being the differential between the pressure in the pore space and the ambient (in our case atmospheric) pressure, ϕ the volumetric fraction of open porosity, and V the sample volume. Standardizing the fragmentation energy to a unit volume the energy density, ρ_E , is defined as:

$$\rho_E = E/V = \Delta P \phi \quad (5.2)$$

The minimum ρ_E needed to initiate fragmentation can be considered to be the “fragmentation threshold energy density” or alternatively as the “threshold energy density” $\rho_{E_{fr}}$. In analogy to equation (5.2) this value is determined as:

$$\rho_{E_{fr}} = E(\Delta P_{fr})/V = \Delta P_{fr} \cdot \phi \quad (5.3)$$

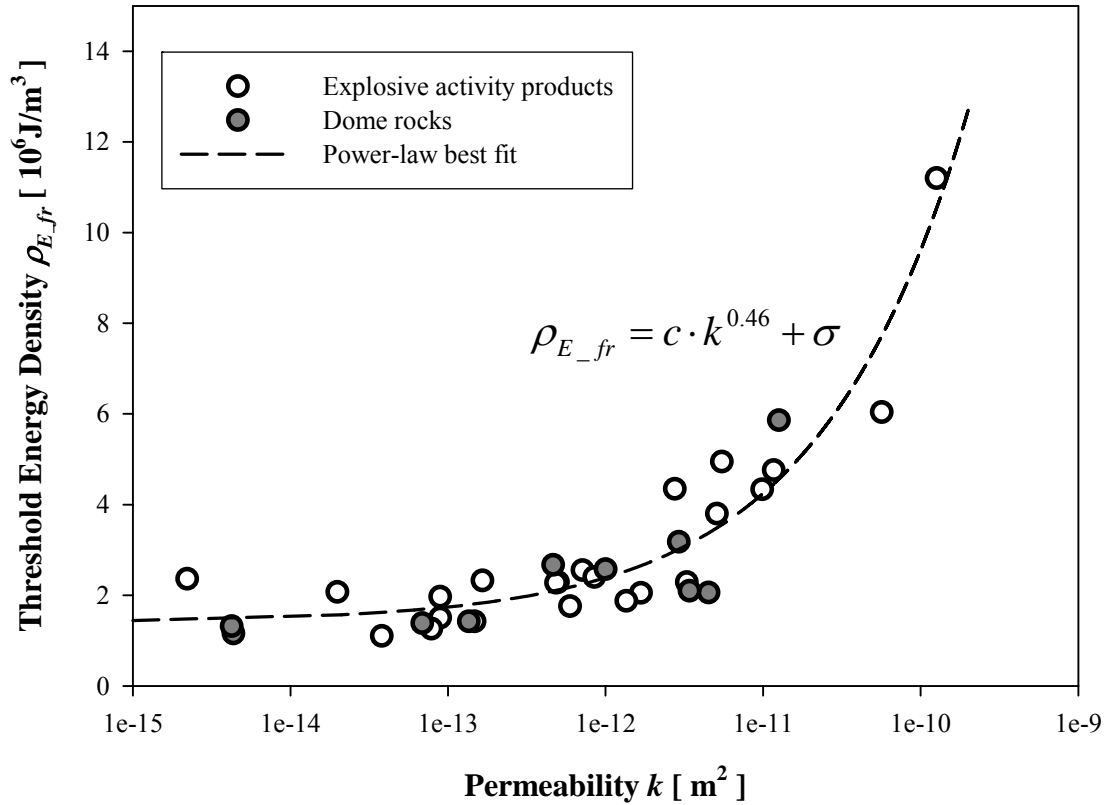


Figure 5.7: The fragmentation threshold energy density, $\rho_{E_{fr}}$, plotted against the corresponding permeability coefficients, k , on a logarithmic scale (both determined at room temperature). The increasing trend can be fitted by a power-law relation in the form $\rho_{E_{fr}} = c \cdot k^{0.46} + \sigma$ ($r^2=0.87$), with $c= 3.27 \cdot 10^5$ MPa/m², and $\sigma=1.4$ MPa. Interestingly, data points for dome rock and explosive activity products (pumices and breadcrust bombs) fully coincide, despite their very different pore textures responsible for gas filtration (cracks or highly deformed pores in long-term degassed dome rocks, and a network of interconnected, spherical bubbles in material produced by explosive activity, respectively), and their different permeability-porosity trends (Chapter 4). This concurrence supports the broad predictive value of the proposed model.

By relating the experimentally determined threshold energy density values of the samples with their measured permeability (Figure 5.7), the influence of a high rate of degassing on fragmentation becomes evident. Regression analysis reveals a data increase following the power-law distribution

$$\rho_{E_{fr}} = 3.27 \cdot 10^5 \cdot k^{0.46} + 1.4. \quad (5.4)$$

By combining equations (5.3) and (5.4) a correlation of the fragmentation threshold with the sample porosity and permeability is obtained:

$$\Delta P_{fr} = (c \cdot k^{0.46} + \sigma) \cdot 1/\phi \quad (5.5)$$

where c and σ are constants with the values $3.27 \cdot 10^5$ MPa/m² and 1.4 MPa, respectively.

5.4.2 Implications

Previous definitions of the criterion required for magma fragmentation have invoked either a range of porosity (*Sparks 1978; Sparks et al. 1994; Thomas et al. 1994; Gardner et al. 1996*) or a combination of porosity and overpressure (*Zhang 1999, Spieler et al. 2004b*). The equation (5.5) bears similarities to the empirically defined criterion given by *Spieler et al. (2004b)*. The comparison of the two equations strongly suggests that the constant σ , used in this study, can be regarded as an averaged value of the effective tensile strength of the samples matrix. The value of $\sigma=1.4$ MPa agrees well with the values reported by *Spieler et al. (2004b)*. In this way, equation (5.5) represents an enhanced fragmentation criterion that relates the fragmentation threshold pressure not only to the porosity, but also to the rock permeability.

The data distribution in Figure 5.7 indicates that at k -values around 10^{-12} m² there is a notable change in the influence of permeability. For $k < 10^{-12}$ m² the threshold energy density is more or less constant. Consequently, the effect of permeability on the fragmentation behaviour is minor and can be sufficiently explained by existing models. For $k > 10^{-12}$ m² the threshold energy density increases sharply, suggesting that the permeability is taking over control on the fragmentation process. Furthermore, it is remarkable that the data in Figure 5.7 display a well defined trend with a relatively low degree of scatter, despite the very different properties exhibited by the samples, such as bulk chemistry, crystallinity, porosity, and tortuosity. As a result, it can be concluded that the influence of these material properties on the fragmentation behaviour is minor compared to that of the permeability.

The fit accuracy of the criterion proposed here with respect to the experimental results is shown in Figure 5.8, and compared with results calculated with the fragmentation criterion by *Spieler et al. 2004b*. The data distribution demonstrates that the criterion incorporating the permeable gas flow is capable of predicting the

fragmentation threshold with an explicitly higher accuracy than the purely porosity-related criterion of *Spieler et al.* 2004b.

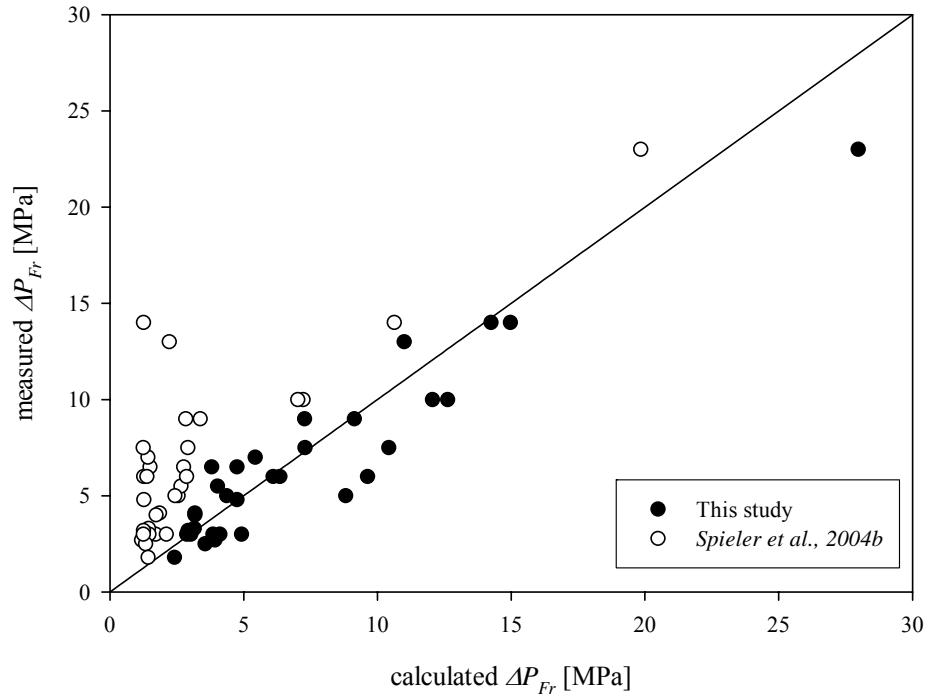


Figure 5.8: Comparison of the fit accuracy of the theoretically predicted ΔP_{fr} values according to the criterion of this work ($\Delta P_{fr} = (3.27 \cdot 10^5 \text{ kg/m}^3 \text{ s}^2 \cdot k^{0.46} + 1.4 \text{ MPa}) \cdot 1/\phi$; full circles) and the work of *Spieler et al.* 2004b ($\Delta P_{fr} = 0.995 \text{ MPa} \cdot 1/\phi$; open circles). The experimentally determined fragmentation threshold pressures of the 32 pyroclast samples of this work are therefore plotted against the values calculated with the two equations, respectively. The data distribution demonstrates that the criterion of *Spieler et al.* 2004b, neglecting the effect of permeable gas flow, overestimates the threshold of most of the samples, whereas the deviation between measured and calculated values remains small ($r^2=0.98$) throughout the entire sample set for the criterion proposed in this work.

6 Summary and conclusions

Porosity and permeability are both parameters which may have a considerable impact on the characteristics of a volcanic eruption. Various processes, from magmatic flow during ascent to the point of magmatic fragmentation during an explosive eruption are influenced, and sometimes even controlled by the amount of volatiles trapped in a magma's pore space and by the efficiency of their escape. Detailed investigations of the porosity of pyroclastic rocks and its relation to the gas permeability are therefore crucial for the understanding of such processes and may provide an important database for physical models. The combination of experimental work and field investigation represents in this context an effective approach to obtain a statistically relevant amount of data on the one hand, and, on the other hand, experimentally quantify the correlation between different parameters.

For this study, density data of pyroclastic deposits from eight circum-pacific volcanoes were recalculated to porosity values using the determined matrix density of the corresponding rocks. The pyroclasts density was determined directly in the field with a method based on the Archimedean principle; the matrix density was determined in the laboratory using a He-Pycnometer. The comparison of the resulting porosity distribution histograms allows (a) the investigation of local features related to depositional mechanisms, if the distribution of single measurement points is evaluated, and (b) statements about large scale coherencies regarding the eruptive style and the explosivity of a volcano, if the compiled datasets of the volcanoes are compared.

The shape and the variance of the distribution curves, as well as the positions of the porosity peak or mean porosity values are parameters that can be used for further interpretation. The differences in the porosity distribution patterns allowed the classification of the investigated volcanoes into three groups, corresponding to their eruptive characteristics: (1) dome-building volcanoes with predominantly block-and-ash-flow activity and occasional Vulcanian explosions (Merapi, Unzen, Colima), (2) cryptodome-forming volcanoes with a subsequent lateral-blast eruption (Bezymianny, Mount St. Helens), and (3) Subplinian to Plinian explosive eruptions (Krakatau, Kelut, Augustine).

Furthermore, possible coherencies between the mean porosity values of selected eruptions and their explosivity, expressed in two different explosivity indexes, were evaluated. The ‘Volcanic Explosivity Index’ (VEI), introduced by *Newhall & Self* (1982), is mainly based on the volume of the erupted tephra, and shows a rough positive correlation to the mean porosity of eruptive products. A qualitative enhancement of this correlation, especially considering low-porosity, low-explosive deposits, was achieved by using the measured porosity values to determine the index of the ‘Eruption Magnitude’, introduced by *Pyle* 1995. Volcanoes with not only pure explosive (Vulcanian and/or Plinian) activity were found to deviate systematically from this correlation. Besides their relevance for the understanding and modeling of eruption physics, the interpretation of porosity data may help to discriminate eruption characteristics and explosivities also at historic and pre-historic eruption deposits.

The main focus of this work was the experimental investigation of the gas permeability of volcanic rocks. In order to simulate degassing processes under strongly transient conditions, the experiments were performed on a shock-tube like apparatus. The permeability of a natural porous material depends on a complex mixture of physical and textural parameters. Evidently, the volume fraction of the materials pore space, i.e. its porosity, is one of the prominent factors controlling permeable gas flow. But, as a high scatter of measured permeability values for a given porosity indicates, it seems that parameters like vesicle sizes, vesicle size distribution, vesicle shape, the degree of interconnectivity et cetera may likewise influence filtration properties. Therefore it is almost impossible to predict the permeability development of natural material with theoretical cause-and-effect relations, and experimental work in this field is essential. By performing more than 360 gas filtration experiments on 112 different samples from 13 volcanoes, a comprehensive permeability and porosity database was created with this study, giving rise to profound empirical as well as quantitative investigations.

The dependency of porosity and permeability of volcanic rocks was found to follow two different, but overlapping trends, according to the geometries of the gas-flow providing pore-space: at low porosities (i.e. long-term degassed dome rocks), gas escape occurs predominantly through microcracks or elongated micropores and therefore could be described by simplified forms of capillary (Kozeny-Carman relations) and fracture flow models. At higher porosities, the influence of vesicles becomes progressively stronger as they form an increasingly connected network.

Therefore, a model based on the percolation theory of fully penetrable spheres was used, as a first approximation, to describe the permeability-porosity trend.

To investigate possible influences of high temperatures on the degassing properties of volcanic rocks, a measuring method that allowed permeability experiments at temperatures up to 750 °C was developed and tested. A sealing coat of compacted NaCl, which was, if required, further compressed during the high-T experiment, was found to be the most promising approach to avoid gas leaking due to different thermal expansivities of the materials involved. The results of three dome rock samples showed distinct lower gas filtration rates at high temperatures. As this may, for the largest part, be attributed to changed gas properties at high temperature, the obtained permeability values must be corrected for the enhanced gas viscosity. The corrected permeability values of the samples were higher than those obtained at room temperature, possibly caused by thermal expansion of the pores. Since, however, compressional forces of the salt coating upon the sample cylinder may lower the permeability particularly of highly fractured rocks to a not quantifiable degree, these results must be interpreted accordingly and seen under certain restrictions.

Comparison of the permeability values before and after the heating process revealed that no permanent structural changes in the pore network occurred. This was confirmed by a 5h-experiment on a trachytic sample, with permeability tests in an interval of 60 minutes.

The influence of permeability on magmatic fragmentation is of special interest for the modelling of eruptive processes. In particular the ‘fragmentation threshold’, i.e. the physical conditions, at which magma is no longer able to reduce gas overpressure by filtration and fragments, represents an important boundary condition for explosive eruption models. Former studies defined this threshold to depend on either the porosity of the magma, or a combination of porosity and overpressure. The experimental results of this work, however, reveal that, in addition to porosity and applied overpressure, the permeability strongly influences the fragmentation threshold. By quantifying this influence in a simple, analytical equation, these results will provide a valuable tool for physical models of eruption mechanics.

7 Bibliography

- Alidibirov M & Dingwell DB (1996a) Magma fragmentation by rapid decompression. *Nature* **380**: 146-148
- Alidibirov M & Dingwell DB (1996b) An experimental facility for the investigation of magma fragmentation by rapid decompression. *Bull. Volcanol* **58**: 411-416
- Alidibirov M, Dingwell DB (2000), Three fragmentation mechanisms for highly viscous magma under rapid decompression, *J Volcanol Geotherm Res* **100**: 413–421
- Andreastuti SD, Alloway BV, Smith IEM (2000) A detailed tephrostratigraphic framework at Merapi volcano, Central Java, Indonesia: implications for eruption predictions and hazard assessment. *J Volcanol Geotherm Res* **100**: 51-67
- Belikov BP, Zaleskii BV, Rozanov YA, Sanina EA, Timchenko IP (1964) Methods of studying the physicommechanical properties of rocks. In: Zaleskii BV (ed.) Physical and mechanical properties of rocks. Izdatel'stvo Nauka, Moskau, 1-58
- Belousov A (1996) Deposits of the 30 March 1956 directed blast at Bezymianny volcano, Kamchatka, Russia. *Bull Volcanol* **57**: 649-662
- Blower JD (2001a) Factors controlling permeability-porosity relationships in magma. *Bull Volcanol* **63**: 497-504
- Blower JD (2001b) A three-dimensional network model of permeability in vesicular material. *Comp Geosci* **7**: 115-119
- Bogoyavlenskaya GY, Braitseva OA, Melekestsev IV, Maksimov AP, Ivanov BV (1991) Bezymianny Volcano. In: Fedotov SA, Masurenkov YuP (eds) Active volcanoes of Kamchatka, v. 1. Nauka, Moscow, pp 166-197
- Brace WF, Walsh JB, Frangos WT (1968) Permeability of Granite under High Pressure. *J Geophys Res* **73**: 2225-2236
- Bourdier J-L, Pratomo I, Thouret J-C, Boudon G, Vincent PM (1997) Observations, stratigraphy and eruptive processes of the 1990 eruption of Kelut volcano, Indonesia. *J Volc Geotherm Res* **79**: 181-203
- Burgisser A, Gardner JE (2005) Experimental constraints on degassing and permeability in volcanic conduit flow. *Bull Volcanol* **67**: 42-56

- Carman PC (1956) Flow of Gases Through Porous Media. Academic Press, New York, pp 1-182
- Cashman KV, Sturtervant B, Papale P, Navon O (2000) Magmatic fragmentation. In: Sigurdsson H (ed) Encyclopedia of Volcanoes. Academic Press, London, pp 421-430
- Darcy HPG (1856) Les Fontaines Publique de la Ville de Dijon. Victor Dalmont, Paris, pp 1-647
- Dellino P, La Volpe L (1995) Fragmentation versus transportation mechanisms in the pyroclastic sequence of Monte Pilato - Rocche Rosse (Lipari, Italy). *J Volcanol Geotherm Res* **64**: 211-231
- De Vita S, et al (1999) The Agnano-Monte Spina eruption (4100 years BP) in the restless Campi Flegrei caldera (Italy). *J Volcanol Geotherm Res* **123**: 269-301
- Dingwell DB (1996) Volcanic dilemma: flow or blow? *Science* **273**: 1054-1055
- Dingwell DB (1998a) Magma degassing and fragmentation. Recent experimental advances. In: Freundt A, Rosi M (eds) From Magma to Tephra. Modelling physical processes of explosive volcanic eruptions. Elsevier, Amsterdam, pp 1-23
- Dingwell DB (1998b) Recent experimental progress in the physical description of silicic magma relevant to explosive volcanism. In: Gilbert JS, Sparks RSJ (eds) The physics of Explosive Volcanic Eruptions. Geological Society, London, Special Publications 145, 9-26.
- Doyen PM (1988) Permeability, conductivity, and pore geometry of sandstone. *J Geophys Res* **93**: 7729-7740
- Druitt TH, Mellors RA, Pyle DM, Sparks RSJ (1989) Explosive volcanism on Santorini, Greece. *Geol Mag* **126**: 95-126
- Druitt TH, Edwards L, Mellors RM, Pyle DM, Sparks RSJ, Lanphere M, Davies M, Barreirio B (1999) Santorini volcano. *Geol Soc London Mem* **19**: 1-165
- Druitt TH, et al. (2002) Episodes of cyclic vulcanian explosive activity with fountain collapse at Soufrière Hills Volcano, Montserrat. In: Druitt TH, Kokelaar BP (eds) The Eruption of Soufrière Hills Volcano, Montserrat, from 1995 to 1999. *Geol Soc Lond, Memoirs* **21**, pp 281-306
- Dullien FAL (1979) Porous Media — Fluid Transport and Pore Structure. Academic Press, San Diego, pp 1-396
- Eichelberger JC, Carrigan CR, Westrich HR, Price RH (1986) Non-explosive silicic volcanism. *Nature* **323**: 598-602
- Enck FD, Dommel JG (1965) Behaviour of the Thermal Expansion of NaCl at Elevated Temperatures. *J Appl Phys* **36**: 839-844

- Feng S, Halperin HI, Sen PN (1987) Transport properties of continuum systems near the percolation threshold. *Phys Rev B* **35**: 197-214
- Francalanci L, Tommasini S, Conticelli S (2004) The volcanic activity of Stromboli in the 1906-1998 AD period: mineralogical, geochemical and isotope data relevant to the understanding of the plumbing system. *J Volc Geotherm Res* **131**: 179-211
- Francis P, Oppenheimer C (2004) *Volcanoes*, 2nd edition. Oxford University Press, Oxford, pp 1-521
- Gardner JE, Thomas RME, Jaupart C, Tait S (1996) Fragmentation of magma during Plinian volcanic eruptions. *Bull Volcanol* **58**: 144-162
- Gertisser R, Keller J (2003) Temporal variations in magma composition at Merapi Volcano (Central Java, Indonesia): magmatic cycles during the past 2000 years of explosive activity. *J Volcanol Geotherm Res* **123**: 1-23
- Getahun A, Reed MH, Symonds R (1996) Mount St. Augustine volcano fumarole wall rock alteration: mineralogy, zoning, composition and numerical models of its formation process. *J Volcanol Geotherm Res* **71**: 73-107
- Gilbert JS, Sparks RSJ (1998) Future research directions on the physics of explosive volcanic eruptions. In: Gilbert JS, Sparks RSJ (eds) *The physics of Explosive Volcanic Eruptions*. Geological Society, London, Special Publications **145**, 9-26
- Gioncada A, Mazzuoli R, Bisson M, Pareschi MT (2003) Petrology of volcanic products younger than 42 ka on the Lipari-Volcano complex (Aeolian Islands, Italy): an example of volcanism controlled by tectonics. *J Volcanol Geotherm Res* **122**: 191-220
- Gonnermann HM, Manga M (2003) Explosive volcanism may not be an inevitable consequence of magma fragmentation. *Nature* **426**: 432-435
- Hammer JE, Cashman KV, Hoblitt RP, Newman S (1999) Degassing and microlite crystallization during pre-climactic events of the 1991 eruption of Mt. Pinatubo, Philippines. *Bull Volcanol* **60**: 355-380
- Harford CL, Sparks RSJ, Fallick AE (2003) Degassing at the Soufriere Hills Volcano, Montserrat, recorded in matrix glass compositions *J Petrology* **44**: 1503-1523
- Hoblitt RP, Harmon RS (1993) Bimodal Density Distribution of Cryptodome Dacite from the 1980 Eruption of Mount St. Helens, Washington. *Bull Volcanol* **55**: 421-437
- Hoblitt RP, Wolfe EW, Scott WE, Couchman MR, Pallister JS, Javier D (1996) The preclimactic eruptions of Mount Pinatubo, June 1991. In: Newhall CG, Punongbayan RS (eds) *Fire and Mud: Eruptions and Lahars of Mount*

- Pinatubo, Philippines. Quezon City, Philippines: Philippine Inst Volc Seism, and Seattle: Univ Wash Press, pp 457-511
- Horwell CJ, Brana LP, Sparks RSJ, Murphy MD, Hards VL (2001) A geochemical investigation of fragmentation and physical fractionation in pyroclastic flows from the Soufrière Hills Volcano, Montserrat. *J Volcanol Geotherm Res* **109**: 247–262
- Houghton BF & Wilson CJN (1989) A vesicularity index for pyroclastic deposits. *Bull Volcanol* **51**: 451-462
- Ichihara M, Rittel D, Sturtevant B (2002) Fragmentation of a porous viscoelastic material: implications to magma fragmentation. *J Geophys Res* **107**, doi:10.1029/2001JB000591
- Innocentini MDM, Pardo ARF, Pandolfelli VC (2000) Pressure–Decay Technique for Evaluating the Permeability of Highly Dense Refractories. *J Am Ceram Soc* **83**(1): 220 -222
- Jaupart C, Allegre CJ (1991) Eruption rate, gas content and instabilities of eruption regime in silicic volcanoes. *Earth Planet Sci Lett* **102**: 413-429
- Jaupart C (1998) Gas loss from magma through conduit walls during eruption. In: Gilbert JS, Sparks RSJ (eds) *The physics of Explosive Volcanic Eruptions*. Geological Society, London, Special Publications **145**, 73-90
- Johnson DA (1979) Onset of volcanism at Augustine Volcano, Lower Cook Inlet. *U.S. Geol Surv Circ* **804B**: 78-80
- Johnson DL, Koplik J, Schwartz LM (1986) New pore-size parameter characterizing: transport in porous media. *Phys Rev Lett* **20**, 2564-2567
- Kaminsky E, Jaupart C (1997) Expansion and quenching of vesicular magma fragments in Plinian eruptions. *J Geophys Res* **102**: 12203-12817
- Katz AJ, Thompson AH (1986) Quantitative prediction of permeability in porous rock. *Phys Rev B* **34**: 8179-8181
- Kennedy B, Spieler O, Scheu B, Kueppers U, Taddeucci J, Dingwell DB (2005) Conduit implosion during Vulcanian eruptions. *Geology* **33**: 581-584
- Klug C, Cashman KV (1996) Permeability development in vesiculating magmas — implications for fragmentation. *Bull Volcanol* **58**: 87-100
- Koyaguchi T, Mitani NK (2005) A theoretical model for fragmentation of viscous bubbly magmas in shock tubes. *J Geophys Res* **110**: doi:10.1029/2004JB003513
- Kozeny J (1927) Über kapillare Leitung des Wassers im Boden. *Sitzungsber. Akad. Wiss. Wien* **136**: 271-306

- Kueppers U (2005) Nature and efficiency of pyroclast generation from porous magma: Insights from field investigations and laboratory experiments. PhD thesis, Ludwig-Maximilians-Universität München, pp. 1-104
- Kueppers U, Scheu B, Spieler O, Dingwell DB (2005) Field-based density measurements as tool to identify pre-eruption dome structure: set-up and first results from Unzen volcano, Japan. *J Volcanol Geotherm Res* **141**: 65-75
- Kueppers U, Scheu B, Spieler O, Dingwell DB (2006) Fragmentation efficiency of explosive volcanic eruptions: A study of experimentally generated pyroclasts. *J Volcanol Geotherm Res* **153**: 125-135
- Lamb SH (1945) *Hydrodynamics*, 6th ed. Dover, New York, pp 1-738
- Landau LD, Lifshitz EM (1980) *Course of Theoretical Physics, Vol. 5, Statistical Physics*, 3rd edition. Pergamon, Oxford.
- Langlois WE (1964) *Slow Viscous Flow*. MacMillan, New York, pp 1-229
- Le Bas MJ, LeMaitre RW, Streckeisen A, Zanettin B (1986) A chemical classification of volcanic rocks based on the total alkali-silica diagram. *J Petrol* **27**: 745-750
- Lensky NG, Lyakhovsky V, Navon O (2001) Radial variations of melt viscosity around growing bubbles and gas overpressure in vesiculating magmas. *Earth Planet Sci Lett* **186**: 1-6
- Lensky NG, Navon O, Lyakhovsky V (2004) Bubble growth during decompression of magma: experimental and theoretical investigation. *J Volcanol Geotherm Res* **129**: 7-22
- Liang Y, Price JD, Wark DA, Watson EB (2001) Nonlinear pressure diffusion in a porous medium: Approximate solutions with applications to permeability measurements using transient pulse-decay method. *J Geophys Res.* **106**: 529-535
- Luhr JF (2002) Petrology and geochemistry of the 1991 and 1998-1999 lava flows from Volcán de Colima, Mexico: implications for the end of the current eruptive cycle. *J Volcanol Geotherm Res* **117**: 169-194
- Lyakhovsky V, Hurwitz S, Navon O (1996) Bubble growth in rhyolitic melts: experimental and numerical investigation. *Bull Volcanol* **58**: 19-32
- Mader HM, Manga M, Koyaguchi T (2004) The role of laboratory experiments in volcanology. *J Volcanol Geotherm Res* **129**: 1-5
- Mandeville CW, Carey S, Sigurdsson H (1996) Magma mixing, fractional crystallization and volatile degassing during the 1883 eruption of Krakatau volcano, Indonesia. *J Volcanol Geotherm Res* **74**: 243-274
- Mason BG, Pyle DM, Oppenheimer C (2004) The size and frequency of the largest explosive eruptions on Earth. *Bull Volcanol* **66**: 735-748

- Melnik O (2000) Dynamics of two-phase conduit flow of high-viscosity gas-saturated magma: large variations of sustained explosive eruption intensity. *Bull Volcanol* **62**: 153-170
- Melnik O, Sparks RSJ (2002) Dynamics of magma ascent and lava extrusion at Soufrière Hills Volcano, Montserrat. In: Druitt TH, Kokelaar BP (eds) The eruption of Soufrière Hills Volcano, Montserrat, from 1995 to 1999. *Geol Soc Lond, Memoirs* **21**, pp 153-171
- Melnik O, Sparks RSJ (2004) Controls on conduit magma flow dynamics during lava-dome building eruptions. *J Geophys Res* **110**, B022, doi:10.1029/2004JB003183: 1-21
- Melnik O, Barmin AA, Sparks RSJ (2005) Dynamics of magma flow inside volcanic conduits with bubble overpressure buildup and gas loss through permeable magma. *J Volcanol Geotherm Res* **143**: 53-68
- Mukhopadhyay S, Sahimi M (1994) Scaling behaviour of permeability and conductivity anisotropy near the percolation threshold. *J Statist Phys* **74** (5-6): 1301-1308
- Murphy MD, Sparks RSJ, Barclay J, Carroll MR, Brewer TS (2000) Remobilization of andesite magma by intrusion of mafic magma at the Soufrière Hills Volcano, Montserrat, West Indies. *J Petrol* **41**: 21-42
- Nakada S, Motomura Y (1999) Petrology of the 1990-1995 eruption at Unzen: effusion pulsation and groundmass crystallization. *J Volcanol Geotherm Res* **89**: 173-196
- Nakada S, Shimizu H, Ohta K (1999) Overview of the 1990-1995 eruption at Unzen volcano. *J Volcanol Geotherm Res* **89**: 1-22
- Navon O, Lyakhovsky V (1998) Vesiculation processes in vesiculating magmas. In: Gilbert JS, Sparks RSJ (eds) The physics of Explosive Volcanic Eruptions. Geological Society, London, Special Publications **145**: 27-50
- Navon O, Chekhmir A, Lyakhovsky V (1998) Bubble growth in highly viscous melts: theory, experiments, and autoexplosivity of dome lavas. *Earth Planet Sci Let* **160**: 763-776
- Newhall CG, Self S (1982) The volcanic explosivity index (VEI): an estimate of explosive magnitude for historical volcanism. *J Geophys Res* **87**: 1231-1238
- Orsi G, de Vita S, Di Vito M (1996) The restless, resurgent Campi Flegrei nested caldera Italy: constraints on its evolution and configuration. *J Volcanol Geotherm Res* **74**: 179-214
- Pallister JS, Hoblitt RP, Meeker GP, Knight RJ, Siems DF (1996) Magma mixing at Mount Pinatubo: petrographic and chemical evidence from the 1991 deposits. In: Newhall CG, Punongbayan RS (eds) Fire and Mud: Eruptions and Lahars

- of Mount Pinatubo, Philippines. Quezon City, Philippines: Philippine Inst Volc Seism, and Seattle: Univ Wash Press, pp 687-731
- Papale P (2001) Dynamics of magma flow in volcanic conduits with variable fragmentation efficiency and nonequilibrium pumice degassing. *J Geophys Res* **106** (B6): 11043-11065
- Pfeiffer T (2001) Vent development during the Minoan eruption (1640 BC) of Santorini, Greece, as suggested by ballistic blocks. *J Volcanol Geotherm Res* **106**: 229-242
- Polacci M, Pioli L, Rosi M (2003) The plinian phase of the campanian ignimbrite eruption (Phlegrean Fields, Italy): evidence from density measurements and textural characterization of pumice. *Bull Volcanol* **65**: 418-432
- Pyle DM (1995) Mass and energy budgets of explosive volcanic eruptions. *Geophys Res Lett* **5**: 563-566
- Pyle DM (2000) Sizes of Volcanic Eruptions. In: Sigurdsson H (ed) Encyclopedia of Volcanoes. Academic Press, London, pp 263-269
- Robertson R, et al. (1998) The explosive eruption of Soufrière Hills Volcano, Montserrat, West Indies, 17 september, 1996. *Geophys Res Lett* **25**: 3429-3432
- Robin C, Mossand P, Camus G, Camtagrel J-M, Gourgaud A, Vincent PM (1987) Eruptive history of the Colima volcanic complex (Mexico). *J Volcanol Geotherm Res* **31**: 99-113
- Roobol MJ, Smith AL (1998) Pyroclastic stratigraphy of the Soufrière Hills Volcano, Montserrat - implications for the present eruption. *Geophys Res Lett* **25**: 3393-3396
- Rose HE (1945a) An investigation into the laws of flow of fluids through beds of granular materials. *Proc Inst Mech Eng, War Emergency Issues* **1-12**: 141-147
- Rose HE (1945b) The isothermal flow of gases through beds of granular materials. *Proc Inst Mech Eng, War Emergency Issues* **1-12**: 148-153
- Rose HE (1945c) On the resistance coefficient-Reynolds number relationship for fluid flow through a bed of granular material. *Proc Inst Mech Eng, War Emergency Issues* **1-12**: 154-168
- Rosi M, Bertagnini A, Landi P (2000) Onset of the persistent activity at Stromboli volcano (Italy). *Bull Volcanol* **62**: 294-300.
- Saar MO (1998) The Relationship Between Permeability, Porosity, and Microstructure in Vesicular Basalts. MSc. Thesis, University of Oregon, pp 1-101
- Saar MO, Manga M (1999) Permeability-porosity relationship in vesicular basalts. *Geophys Res Lett* **26**(1): 111-114

- Sahimi M (1994) Applications of Percolation Theory. Taylor and Francis, London, pp 1-300
- Sahimi M (1995) Flow and Transport in Porous Media and Fractured Rocks. VHC Verlagsgesellschaft mbH, Weinheim, pp 1-496
- Scheu B (2005) Understanding silicic volcanism: Constraints from elasticity and failure of vesicular magma. PhD thesis, Ludwig-Maximilians-Universität München, pp. 1-139
- Scheu B, Spieler O, Dingwell DB (2006) Dynamics of explosive volcanism at Unzen volcano: an experimental contribution. *Bull Volcanol*, doi: 10.1007/s00445-006-0066-5
- Schopper J (1982) Porosity and permeability. In: Hellwege KH (ed) Landolt-Börnstein: Physikalische Eigenschaften der Gesteine, Vol. V/1a. Springer, Berlin, pp 184-303
- Schwarzkopf LM, Schmincke H-U, Cronin SJ (2005): A conceptual model for block-and-ash flow basal avalanche transport and deposition based on deposit architecture of 1998 and 1994 Merapi flows. *J Volcanol Geotherm Res* **139**, 117-134
- Shaw HR (1974) Diffusion of H₂O in granitic liquids, 1. Experimental data. In: Hoffman AW, Giletti BJ, Yoder HS, Yund RA (eds) Geochemical transport kinetics. Carnegie Inst Washington Publ **634**: 139-170.
- Siebert L, Simkin T (2002-) Volcanoes of the World: an Illustrated Catalog of Holocene Volcanoes and their Eruptions. Smithsonian Institution. *Global Volcanism Program Digital Information Series*, GVP-3, (<http://www.volcano.si.edu/world/>).
- Sigurdsson H (2000) Introduction In: Sigurdsson H (ed) Encyclopedia of Volcanoes. Academic Press, London, pp 1-13
- Sparks RSJ (1978) The dynamics of bubble formation and growth in magmas: a review and analysis. *J Volcanol Geotherm Res* **3**: 1-37
- Sparks RSJ (1997) Causes and consequences of pressurization in lava dome eruptions. *Earth Planet Sci Lett* **150**: 177-189
- Sparks RSJ, Barclay J, Jaupart C, Mader HM, Phillips JC (1994) Physical aspects of magma degassing. I. Experimental and theoretical constraints on vesiculation. In: Carrol MR, Holloway JR (eds) Volatiles in Magmas: Washington D.C., Mineralogical Society of America, Rev. Mineral. 30. pp. 414-445.
- Spieler O. (2001): Die Fragmentierung hochviskoser Magmen. Experimenteller Aufbau und Analysetechniken. PhD Thesis, Ludwig-Maximilians-Universität München, pp. 1-134

- Spieler O, Alidibirov M & Dingwell DB (2003) Grain-size characteristics of experimental pyroclasts of 1980 Mount St Helens cryptodome dacite: effects of pressure drop and temperature. *Bull Vulcanol* **63**, 90-104
- Spieler O, Dingwell DB & Alidibirov M (2004a) Magma Fragmentation Speed: an experimental determination. *J Vulcanol Geotherm Res* **129**, 109-123
- Spieler O, Kennedy B, Kueppers U, Dingwell DB, Scheu B & Taddeucci J (2004b) The fragmentation threshold of pyroclastic rocks. *Earth Planet Sci Let* **226**: 139-148
- Srouga P, Rubinstein N, Hinterwimmer G (2004) Porosity and permeability in volcanic rocks: a case study on the Serie Tobífera, South Patagonia, Argentina. *J Vulcanol Geotherm Res* **132**: 31-43
- Strohmeier D (2003) Gefügeabhängigkeit technischer Gesteinseigenschaften. PhD Thesis, Georg-August-Universität Göttingen.
- Swanson SE, Kienle J (1988) The 1986 eruption of Mount St. Augustine: field test of hazard evaluation. *J Geophys Res* **93**: 4500-4520
- Thomas N, Jaupart C, Vergnolle S (1994) On the vesicularity of pumice. *J Geophys Res* **99**: 15633-15644
- Toramaru A (1995) Numerical study of nucleation and growth of bubbles in viscous magmas. *J Geophys Res* **100**: 1913-1931
- Verein deutscher Ingenieure (Hrsg) (2002) VDI Wärmeatlas. Berechnungsblätter für den Wärmeübergang. 9th ed. Springer, Berlin.
- Voight B, Young KD, Hidayat D, Subandrio Purbawinata MA, Ratdomopurbo A, Suharna LaHusen R, Marso J, Iguchi M, Ishihara K (2000) Deformation and seismic precursors to dome-collapse and fountain-collapse nuées ardentes at Merapi, Volcano, Indonesia, 1994–1998. *J Vulcanol Geotherm Res* **100**: 261–287
- Waite RB, Begét JE (1996) Provisional Geologic Map of Augustine Volcano, Alaska. U.S. Geol Surv Open-File Report **96-516**
- Watanabe K, Hoshizumi H (1995) Geological Map of Unzen volcano. Geological map of volcanoes 8, Geological survey of Japan
- Wegst CW (1989) Stahlschlüssel. 15. Auflage. Verlag Stahlschlüssel Wegst GmbH, Marbach
- Westrich HR, Eichelberger JC (1994) Gas transport and bubble collapse in rhyolite magma: an experimental approach. *Bull Vulcanol* **56**: 447-458
- Woods AW, Koyaguchi T (1994) Transitions between explosive and effusive eruptions of silicic magma. *Nature* **370**: 641-644

- Zhang Y (1999) A criterion for the fragmentation of bubbly magma based on brittle failure theory. *Nature* **402**: 648-650
- Zobin VM, Luhr JF, Taran YA, Bretón M, Cortés A, De La Cruz-Reyna S, Dominguez T, Galindo I, Gavilanes JC, Muñiz JJ, Navarro C, Ramírez JJ, Reyes GA, Ursula M, Velasco J, Alatorre E, Santiago H (2002) Overview of the 1997-2000 activity of Volcán de Colima, México. *J Volcanol Geotherm Res* **117**: 1-19

Acknowledgements

At the outset, I want to thank Professor Donald B. Dingwell for supervising this work and giving me the opportunity to present my results at countless meetings all around the world.

Thanks to Oliver Spieler for all his support, especially with all kinds of technical questions, and for all the unconventional solutions in the lab. The three field campaigns ('McGyver-tours') in Mexico, Alaska, and Kamchatka were really amazing experiences which I don't want to miss.

Many thanks to Professor Ludwig Masch, for agreeing to act as a second reviewer.

I'm deeply indebted to Betty Scheu for all her help not only with physics and maths problems (even at times when she doubted her skills...), for her half-around-the-globe-assistance at paper and thesis writing, and at any other problem. I really enjoyed working with you, may it be continued somewhere, someday...

Thanks to Ulli Küppers for his virtually unbelievable helpfulness in all kinds of situations (no matter if it is to unscrew an intractable autoclave, repair a Twingo, sell a VW-Bus roof rack, etc.). I wish you a lot of fun on the Azores; enjoy the nightlife, and good luck with your Punk-Pub...

Many thanks to Yan Lavallée for good mood, good music, and the thorough reading of the manuscript. I'll miss the Bavarian coffees...

Thanks also to Benoît Cordonnier, who helped me a lot with image analysis questions, e.g. by giving me a Photoshop-crash course.

Thanks to Dominique Richard for selflessly providing density data and compilations, and for helping me to start my van early in the morning.

I'm grateful to Oleg Melnik, who solved a lot of mathematical and physical problems for me and wrote a specially designed numerical code for the permeability calculation.

Thanks to the employees from the workshop and the secretary for help with technical and administrative problems.

I would like to thank Jacopo Taddeucci (for proof readings, etcetera. See you next year in Toscana...), Alex Nichols (for countless proof-readings), Margarita Polacci (for hosting me in Pisa and introducing me to the mysteries of pumice thin sections), Daniele Giordano (for the Monte Nuovo sample), Clive Oppenheimer (for hosting me in Cambridge) and Andrea di Muro (for providing the Pinatubo samples).

Thanks to the 'Toscana crew', Susi Rummel, Stefan Gottschaller, Andi (aka Schöp) and Saskia Geiß, Christian Dekant and Hanni Schwarz for the very relaxing Toscana holidays and the many interesting culinary creations (e.g. Ananas-Streichwurst or Blumentopfbrotente). A warm welcome to our new member Julian Geiß, born on 21. October 2006.

Special thanks to Stefan Gottschaller for all the interdisciplinary discussions in his office, the mind-clearing coffee breaks (I owe you at least 10 kg of coffee powder...) and the many little hints for the use of weird programmes.

Many thanks to David, for always being there (e.g. just for a beer...).

Many thanks to my parents. Without your support this PhD wouldn't have been possible.

Very special thanks to my wife Hanni and my son Linus for your love, your constant emotional support (bridging even the 700 km between München and Bremen), and your patience with me, especially in the late stages of the PhD. Auf zu neuen Ufern...

The work was financially supported by the EU project MULTIMO and by the BMBF project SUNDAARC – DEVACOM (Publikationsnummer GEOTECH – 273).

Appendices

A. Permeability measurements and the use of the filtration codes – an operating manual

The methods for permeability measurements and data evaluation described in this work have been specially designed for particular investigations relevant to explosive volcanic activity and are therefore hardly comparable to standard measuring techniques. They comprise a complex procedure of sample preparation, installation, measurement, data recording and finally data evaluation. In order to enable a not only theoretical reproducibility of the method, a practical guideline for the steps relevant for measurement and subsequent data editing will be given in the following:

Experimental procedure

- (1) **Sample preparation:** A 25 mm core is drilled out of the respective sample boulder and the edges cut to the desired length (standard length for most of the investigations on the fragmentation apparatus is 60 mm. However, permeability measurements at lengths down to 20 mm and up to 100 mm are operable). The edges should be polished coplanar.
- (2) **Pycnometric density measurement/ BET surface analysis:** After drying and weighing the sample may pass through the non-destructive characterisation procedures of interest. Porosity/ density measurements on the AccuPyc™ are a standard precursor for further fragmentation/ permeability investigations.
- (3) **Sample installation:** The sample cylinder is glued into a steel tube using an adhesive (Crystalbond™) that softens and is processible at a temperatures of 71 °C, and consolidates and becomes gas tight when cooling down to room temperature (Figure A1). For high-temperature measurements the sample cylinder is placed in the autoclave, free-standing on the conical shaped inset on top of the sample (in measurement position). Then gradually the salt is filled in the space between sample and autoclave. About every 5 mm, the loose salt grains are compressed in a hydraulic or “Spindel” press, using a steel tube with 28 mm outer and ~25mm inner

diameter. The procedure is repeated, until the compressed salt coat covers the entire sample length.



Figure A1: The sample cylinder is glued into the steel tube using Crystalbond™.

(4) **Autoclave preparation:** The steel tube is screwed onto the lower sealing plug and firmly tightened against a copper or (better) Teflon sealing ring. With a conical shaped placeholder on top, the steel tube is then inserted into the autoclave (sample holder tube + placeholder should fill the lower autoclave volume as precisely as possible), and, by firmly tightening a screw nut, the plug is pressed against the lower edge of the autoclave (Figure A2).



Figure A2: The steel tube is attached to the lower sealing plug (a) and screwed down tightly (b). Subsequently the sample tube is inserted into the autoclave, and the system is sealed with screw nut (c).

(5) **Autoclave installation:** The autoclave is attached to the particle collection tank, with diaphragms of the desired strength placed in the diaphragm holders, and pressure transducers and gas supply are attached to the autoclave. Pressure transducer amplifiers are connected to the recording device (computer or oscillator; Figure A3).



Figure A3: Copper or aluminium diaphragms are placed in the diaphragm holders (a). The autoclave is then attached to the tank and screwed down tightly against the diaphragms (b). Finally the gas supply system and the pressure transducers are attached (c).

- (6) **Data recording:** Commonly a Labview™ applet is used to record and save the pressure signals of the two transducers. It is important for further data editing that the amount of recorded data points is between 5000 and 15000. The sampling interval and the record time should be adjusted accordingly.
- (7) **Filtration experiment:** For the measurement the autoclave is pressurized to the required overpressure. By a controlled exceeding of the uppermost diaphragms strength the upper autoclave volume is rapidly decompressed. The pressure signals are recorded until the pressures in the two volumes are completely equalized.
- (8) The recorded .dyn or .pt files are saved and converted into plain text files.

Data editing procedure

- (1) **Code installation:** Both codes, the steady and transient, consist of a *main.exe*, a *parameter.dat* and a *pressure.txt* file, which should be saved in the same folder for each of the codes. The additional files *grfront.dat* and *rgb.txt*, responsible for graphical presentation of the results, have to be saved in a newly created folder C:\pgplot.
- (2) **Pressure file separation:** For an initial data processing, the plain text file of the pressure recording should be imported to a suitable processing program, in the present case SigmaPlot® 8.0 has been used. All columns except the two pressure transducer signals should be deleted, as well as all forerun recording of the experiment (pressurization phase, constant pressure line etc.). The upper transducer column should be put in column 3 and should contain exactly one maximum pressure value (p_i) before the rapid pressure drop. Lower transducers signal should be placed in column 2.
- (3) **Time axis and conversions:** A time axis according to the chosen sampling interval should be created in column 1. For SigmaPlot, a transform file containing “col(1)=data(0;size(col(2))*x;x)”, where x is the sampling interval in seconds, will create a progressional time series. As the codes require *bar* as a unit of pressure, all *MPa* values should be converted. The three resulting columns “time [s] - p_{low}

[bar] – p_{up} [bar]” should be re-exported to a plain text file. (Note: the codes operate only with dot-separated decimals, so eventually commas have to be converted in this txt-file.)

- (4) **Pressure.txt-file editing of the steady code:** The entire pressure data set will then be copy-pasted into the appropriate section of the *pressure.txt* file of the quasi-steady code. Sample specifications must be entered above in the same file.
- (5) **Param.dat-file editing of the steady code:** The parameters in this file define the boundary conditions for the numerical calculation process of the code. “Min K” and “Max K” are the boundaries for the linear permeability, “Min C” and “Max C” for the non-linear term. For normal rocks k should lie between $1e-15$ and $1e-10$, and C between $1d-1$ and $1d4$ ($1d2 = 100$, $1d3 = 1000, \dots$). If one of the resulting parameters calculated by the code lies on the previously defined boundary value, the respective number should be adjusted. The setting “ik” defines the calculation range for the permeability determination: *0* – the code determines both C and k using the whole dataset, approximation is done with the non-linear Forchheimer law, *1* - determines only the linear permeability k using the tale of the dataset applying Darcy’s law. “tstart” and “dtend” define the time range for this calculation.
- (6) “*main.exe*” starts the code. After the calculations have been performed, a graphic file shows the measured versus the calculated pressure drop curve. k and C results and an mean deviation “delta” are displayed as well. A full compilation of the resulting parameters is found in the file “results.dat”.
- (7) For the use of the **transient code**, the 3 columns of the time/pressure recording must be pasted into the *pressure.txt*-file of the transient code. Calculation parameters, including the sample specifications, have to be entered in the respective *param.dat*-file. Again the *main.exe* file starts the calculations. Note: The correct value of C (transient) is obtained by multiplying the calculated C with the square root of k .

B. Tables of experimental results

Table B.1: Results of room-temperature permeability and laboratory porosity measurements of 112 samples, as well as fragmentation threshold and energy density values. For each of the samples, one to five permeability measurements at different initial pressure differences have been performed. The average values of these experiments are displayed in the table.

Sample	k(quasi-static)[m ²]	C(quasi-static)	k(transient)[m ²]	C (transient)	Φ _{open} [vol%]	Φ _{total} [vol%]	ΔP _{fr} [MPa]	ρ _{E,fr} [10 ⁻⁶ J/m ³]
LIP B02	2,37E-13	661,21	2,67E-13	97,54	53,92	60,05		
LIP B04	1,39E-13	326,06	1,66E-13	233,41	58,13	64,60	4	2,33
LIP B03	6,54E-13	90,50	5,96E-13	38,57	58,65	63,04	3	1,76
LIP C02	4,56E-13	528,48	4,98E-13	337,81	69,38	73,69	3,3	2,29
LIP E01	9,34E-14	572,50	8,90E-14	220,70	39,32	39,57	5	1,97
LIP E03	2,98E-13	249,28	3,90E-13	69,57	38,41	38,74		
LIP E04	7,54E-14	433,24	8,16E-14	294,31	39,22	39,32		
LIP E08	3,41E-14	1998,00	4,94E-14	1749,70	36,47	37,06		
LIP E09	2,03E-14	2475,20	1,99E-14	2847,39	37,69	37,84	5,5	2,07
LIP E11	6,20E-14	236,14	6,94E-14	171,48	36,46	36,95		
LIP E12	3,38E-14	395,12	3,73E-14	294,24	35,50	35,99		
LIP E13	3,03E-14	397,24	3,48E-14	110,04	35,39	36,18		
LIP E14	3,40E-14	117,37	3,80E-14	79,28	31,51	33,78		
LIP E17	3,32E-15	84149,00	3,12E-15	90242,50	39,87	40,46		
LIP E20	2,67E-15	56126,00	2,21E-15	50346,01	36,36	36,63	6,5	2,36
LIP F03	4,29E-13	6834,40	4,85E-13	5424,00	75,82	79,69	3	2,27
LIP F04	5,21E-13	1585,40	5,21E-13	1229,08	76,59	79,97	3,1	2,37
MUZ VUL01	1,06E-13	893,64	1,21E-13	651,02	46,88	53,95		
MUZ VUL02	1,71E-13	210,07	1,47E-13	71,50	47,49	54,25	3	1,42
MUZ VUL03	1,03E-13	1330,77	1,47E-13	375,20	46,34	54,48		
MUZ BKB35	8,99E-14	741,99	9,91E-14	588,52	36,88	42,93		
MUZ BKB 38	6,67E-14	793,82	8,91E-14	804,06	36,70	42,83	4,1	1,50
MUZ 2000 A18	2,56E-15	16775,00	2,67E-15	9001,65	3,83	4,22		
MUZ 2000 A19	7,34E-15	19836,00	8,93E-15	12137,27	4,41	4,41		
MUZ 2001 A22	2,11E-14	1065,24	1,85E-14	1239,93	5,47	5,47		
MUZ 2000 A22	1,51E-14	1764,90	1,68E-14	1064,28	10,12	10,12		
MUZ 2000 A25	3,98E-15	5418,00	3,29E-15	802,42	3,67	3,67	17	0,62
MUZ 2001 A17	4,15E-15	6198,00	4,35E-15	8354,00	5,04	5,04	23	1,16
MUZ 2001 B18	3,63E-14	1508,25	3,96E-14	1115,25	12,37	14,47		
MUZ 2001 C20	2,82E-13	154,15	3,18E-13	118,89	20,16	21,01		
MUZ 2000 D02	4,20E-14	1853,90	5,09E-14	1920,70	12,67	16,21		
MUZ 2000 D09	3,27E-14	2239,80	3,63E-14	1776,70	13,72	16,21		
MUZ 2000 E17	3,10E-14	1546,05	3,52E-14	1209,44	14,12	16,64		
MUZ 2000 E21	3,31E-14	1366,40	3,91E-14	1110,18	14,89	17,42		

MUZ 2000 E22	3,60E-14	1976,50	3,87E-14	1450,30	14,53	16,88		
MUZ 2000 G18	3,75E-12	2,49	4,50E-12	1,55	41,18	42,00	5	2,06
MUZ 2000 G32	7,88E-13	48,06	9,33E-13	28,61	37,89	38,93		
MUZ 2000 G38	5,43E-13	129,27	8,53E-13	149,37	32,46	34,55		
MUZ 2000 G52	2,89E-12	3,57	3,41E-12	2,25	34,93	36,04	6	2,10
MUZ 2001 F18	9,87E-13	52,57	9,99E-13	37,73	34,33	36,69	7,5	2,57
MUZ 2001 F23	1,14E-12	24,30	1,29E-12	17,38	34,88	37,43		
MUZ 2001 F24	1,11E-12	20,18	1,44E-12	10,97	34,77	37,02		
MP A02	7,81E-14	345,49	6,88E-14	62,87	13,85	13,85	10	1,39
MP A03	9,25E-14	1673,95	1,35E-13	1557,42	14,25	14,25	10	1,43
MP B04	4,93E-13	138,97	5,35E-13	142,90	29,66	30,37	9	2,67
MP B10	1,63E-12	17,17	2,14E-12	16,29	34,59	36,44		
MP B12	2,35E-12	5,41	2,91E-12	4,16	35,30	35,76	9	3,18
MP C01	9,66E-12	0,74	1,26E-11	0,12	45,10	45,50	13,5	6,09
CFS 02	4,65E-12	2,59	5,46E-12	1,87	70,69	73,70		
CFS 03	1,10E-11	1,42	1,17E-11	0,08	79,33	81,95		
CFS 06	2,00E-12	4,37	2,06E-12	1,02	66,87	69,80		
CFS15	6,64E-12	1,26	7,66E-12	0,41	72,28	75,20		
CFS16	2,84E-12	4,25	3,30E-12	2,05	66,39	69,17		
CFS18	1,94E-12	12,03	2,56E-12	7,20	66,63	72,31		
CFS27	4,53E-12	3,44	5,08E-12	1,54	79,19	82,08	4,8	3,80
SNT01	1,18E-12	29,21	1,35E-12	18,25	75,17	82,03	2,5	1,88
SNT03	6,95E-14	2216,40	7,83E-14	1610,20	70,12	78,34		
SNT05	5,90E-13	162,81	7,13E-13	124,04	79,84	84,42		
SNT06	8,91E-13	189,91	8,73E-13	59,35	79,00	84,38		
SNT12	7,27E-13	261,05	8,47E-13	180,86	80,09	84,61	3	2,40
STR_Br249	4,77E-13	98,36	5,35E-13	74,71	49,39	50,14		
Stbr02	1,18E-11	0,59	1,27E-11	0,19	71,95	72,87		
Stbr03	2,57E-13	112,11	2,97E-13	76,46	58,70	59,90		
Stbr04	5,77E-13	30,39	6,23E-13	21,21	62,30	63,18		
STR_Bi	5,44E-11	0,19	5,65E-11	0,05	80,50	81,24	7,5	6,04
Str_Bi03	1,38E-11	0,52	1,42E-11	0,33	66,05	68,95		
PIN A01	2,76E-12	7,78	3,56E-12	7,62	60,18	61,83		
PIN A02	2,99E-12	6,32	3,81E-12	6,04	60,31	62,40		
PIN B01	1,77E-12	22,39	2,27E-12	16,63	51,36	65,88		
PIN B07	1,23E-13	420,39	1,36E-13	269,43	51,97	63,65		
PIN B09	1,45E-12	20,41	1,10E-12	8,08	47,64	58,16		
PIN C04	8,44E-13	16,65	9,08E-13	7,81	50,70	55,77		
PIN C03	6,97E-13	26,06	8,09E-13	12,54	51,48	58,56		
PIN GFL1a	1,17E-12	8,79	1,35E-12	6,19	76,34	78,49		

PIN GFL1b	1,28E-12	9,76	1,72E-12	8,03	73,16	76,36		
PIN GFL1c	4,21E-13	29,74	5,78E-13	37,28	71,18	74,97		
PIN GFL2a	4,40E-13	29,69	5,44E-13	26,04	72,12	74,38		
PIN GFL3aa	1,08E-12	19,83	1,11E-12	7,70	72,99	75,20		
PIN GFL4a	5,68E-13	73,47	6,22E-13	58,01	68,39	73,89		
PIN GFL5	9,42E-14	381,27	1,03E-13	283,83	67,20	74,14		
PIN GFL6	1,58E-13	246,51	1,88E-13	195,01	67,84	73,52		
MTSR33	1,80E-12	25,32	1,67E-12	4,18	68,35	74,01	3	2,05
MTSR38	1,82E-12	98,59	1,60E-12	70,82	66,79	74,46		
MTSR86	1,29E-11	1,32	1,45E-11	0,70	67,52	73,62		
AuB1 02	4,70E-15	12362,00	4,24E-15	14291,82	9,41	9,41	14	1,32
AuC1 01	1,07E-12	13,92	1,17E-12	10,99	37,21	37,94		
AuC1 02	2,44E-12	3,49	2,68E-12	2,36	48,05	48,30		
AUG P4x	2,67E-13	320,25	2,09E-13	99,44	70,52	76,68		
AuP104	1,73E-12	9,05	1,93E-12	6,66	47,68	53,84		
CoC6 03	1,35E-13	787,68	1,51E-13	736,48	14,27	14,27		
CoD2 06	1,70E-12	20,11	2,21E-12	14,27	18,96	19,00		
CoD2 13	8,65E-13	97,23	9,56E-13	85,48	18,25	18,42		
CoD2 30	1,88E-12	7,38	2,38E-12	7,55	21,64	21,64		
CoE4 04	9,89E-13	18,81	1,05E-12	13,29	44,20	47,72		
CoP3 05	7,17E-12	1,24	8,54E-12	0,92	64,69	66,21		
CoP4 01	1,14E-12	43,18	1,36E-12	55,93	62,12	64,76		
KeC3 01	6,62E-13	132,05	7,22E-13	107,91	28,05	28,76		
KeD4 01	2,49E-12	6,45	2,87E-12	5,46	46,72	50,73		
KeD4 02	2,61E-12	7,00	2,88E-12	5,49	48,93	52,94		
KeD9 02	1,99E-12	12,14	2,41E-12	10,77	47,33	50,57		
KrA11 01	3,87E-14	4345,80	4,05E-14	3511,49	22,67	23,07		
KrD4 02	5,02E-14	590,15	6,57E-14	727,00	41,45	41,45		
KrE6 01	1,75E-13	178,29	2,51E-13	166,79	65,20	65,37		
KrTP	1,49E-10	0,02	1,51E-10	0,02	78,14	78,14		
KrR4 01	2,61E-12	16,18	3,27E-12	6,53	84,75	89,96	2,7	2,29
KrR4 02	9,76E-13	71,74	1,21E-12	56,15	82,37	88,59		
KrS2 01	1,19E-12	28,16	1,52E-12	27,39	73,36	81,39		
BeB1 01	1,72E-13	10,84	2,17E-13	10,42	25,52	28,32		
BeC3 01	3,08E-13	1896,05	2,88E-13	1176,75	38,04	41,49		
BeC3 02	4,28E-13	321,61	6,15E-13	364,92	38,52	41,99		
BeD2 06	8,26E-12	1,16	9,24E-12	0,91	45,42	45,47		
BeE1 01	7,04E-12	1,24	8,28E-12	0,98	50,87	51,12		

Appendices

Table B.2: Parameters and results of high-temperature permeability experiments. The measurements of the Camp Flegrei trachyte have been performed at 0, 120, 180, 240 and 300 min after experiment start.

Experiment	ΔP_i	T_{furnace} [°C]	T_{gas} [°C]	k(steady) [m ²]	C(steady)	k(transient) [m ²]	C(transient)	μ_{argon} [10 ⁻⁵ Pas]	k corr	C corr	k drop [%]	Φ_{open} [vol%]	Φ_{total} [vol%]
MUZ 2001 A20_b	1,65	25		9,23E-15	764,54	1,17E-14	1389,29					4,72	5,1
MUZ 2001 A20_h	1,63	707	707	5,76E-15	95782,00	8,10E-15	421736,86	5,26	1,89E-14	181202,53	30,9	4,72	5,1
MUZ 2001 A20_h	1,67	25		8,90E-15	1489,50	1,04E-14	2424,88					4,72	5,1
MUZ 2000 A17_b	2,59	25		1,92E-13	97,21	2,16E-13	96,31					9,23	9,69
MUZ 2000 A17_h	2,62	750	730	6,89E-14	96,61	7,54E-14	287,99	5,34	1,78E-13	121,88	65,1	9,23	9,69
MUZ 2000 A17_a	2,60	25		2,01E-13	63,67	2,16E-13	52,08					9,23	9,69
MUZ 2000 D b	1,57	25		6,10E-14	2978,80	5,68E-14	3767,35					14,1	16,2
MUZ 2000 D_h	1,56	750	701	4,33E-14	5572,30	3,73E-14	20182,53	5,25	8,67E-14	8688,10	34,4	14,1	16,2
MUZ 2000 D_a	1,56	25		7,84E-14	2905,40	6,11E-14	2803,83					14,1	16,2
MP B10_b	1,70	25		1,83E-12	8,90	2,03E-12	7,01					35,48	36,44
MP B10_h	1,70	750	701	1,15E-12	3,86	1,33E-12	10,52	5,25	3,08E-12	4,53	34,6	35,48	36,44
MP B10_a	1,71	25		3,86E-12	16,89	2,11E-12	4,47					35,48	36,44
cf_mn05_1	0,46	25		3,84E-13	37,77							46,71	
cf_mn05_1h	0,46	750		4,27E-13	83,21							46,71	
cf_mn05_2h	0,46	750		4,39E-13	104,64							46,71	
cf_mn05_3h	0,46	750		4,89E-13	79,44							46,71	
cf_mn05_3h	0,46	750		4,56E-13	96,11							46,71	

Curriculum vitae

Persönliche Daten

Sebastian Philipp Müller, geboren am 20. Mai 1975 in München
verheiratet, 1 Kind

Schulbildung

1981-1985	Besuch der Tagesheimschule an der Hochstraße, München
1985-1994	Besuch des Willi-Graf-Gymnasiums, München
Juli 1995	Erwerb der allgemeinen Hochschulreife

Studium

1995-1996	Studium der Geographie an der Technischen Universität München
1996-2002	Studium der Geologie/Paläontologie an der Ludwig-Maximilians-Universität München
September 2002	Erwerb des Diploms in Geologie/Paläontologie
Seit November 2002	Promotion an der Fakultät für Geowissenschaften, LMU München

Berufstätigkeit

Seit November 2002	Wissenschaftlicher Mitarbeiter am Department für Geo- und Umweltwissenschaften der LMU München
--------------------	--